

PCT

Express Mail Mailing Label No.  
EV 68884368  
WORLD INTELLECTUAL PROPERTY ORGANIZATION  
International Bureau

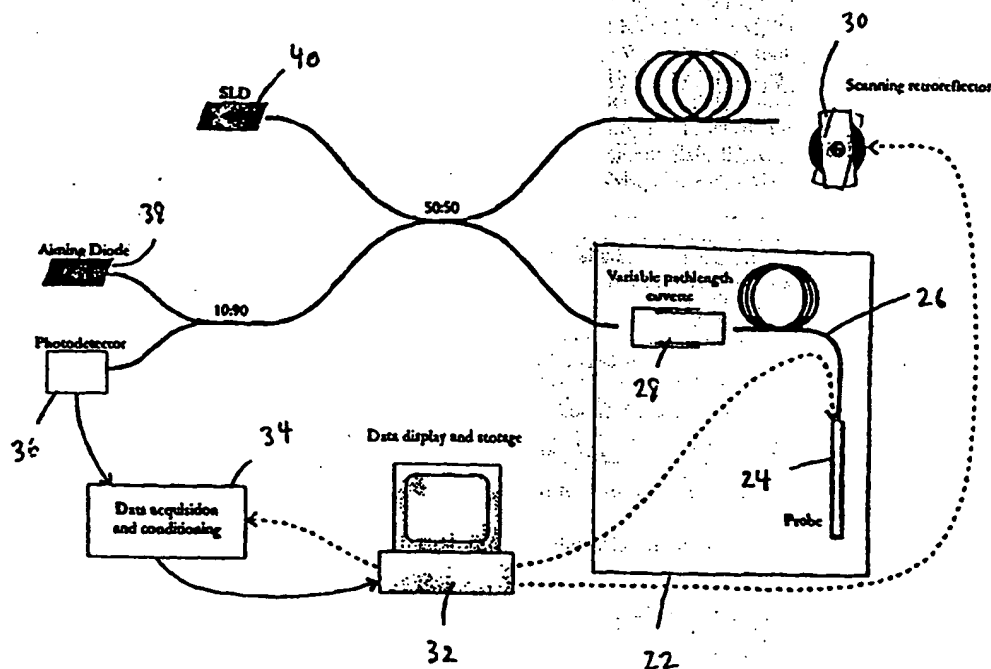
B-32

## INTERNATIONAL APPLICATION PUBLISHED UNDER THE PATENT COOPERATION TREATY (PCT)

(51) International Patent Classification 6 : G01B 9/02		A1	(11) International Publication Number: WO 99/57507
			(43) International Publication Date: 11 November 1999 (11.11.99)
(21) International Application Number: PCT/US99/09626		(81) Designated States: AE, AL, AM, AT, AU, AZ, BA, BB, BG, BR, BY, CA, CH, CN, CU, CZ, DE, DK, EE, ES, FI, GB, GD, GE, GH, GM, HR, HU, ID, IL, IN, IS, JP, KE, KG, KP, KR, KZ, LC, LK, LR, LS, LT, LU, LV, MD, MG, MK, MN, MW, MX, NO, NZ, PL, PT, RO, RU, SD, SE, SG, SI, SK, SL, TJ, TM, TR, TT, UA, UG, US, UZ, VN, YU, ZA, ZW, ARIPO patent (GH, GM, KE, LS, MW, SD, SL, SZ, UG, ZW), Eurasian patent (AM, AZ, BY, KG, KZ, MD, RU, TJ, TM), European patent (AT, BE, CH, CY, DE, DK, ES, FI, FR, GB, GR, IE, IT, LU, MC, NL, PT, SE), OAPI patent (BF, BJ, CF, CG, CI, CM, GA, GN, GW, ML, MR, NE, SN, TD, TG).	
(22) International Filing Date: 30 April 1999 (30.04.99)			
(30) Priority Data: 60/083,785 1 May 1998 (01.05.98) US			
(71) Applicant (for all designated States except US): BOARD OF REGENTS, THE UNIVERSITY OF TEXAS SYSTEM [US/US]; 210 W. 7th Street, Austin, TX 78701 (US).			
(72) Inventors; and			
(75) Inventors/Applicants (for US only): ZULUAGA, Andrés [CO/US]; Apartment I, 912 W. 22 1/2 Street, Austin, TX 78705 (US). UTZINGER, Urs [CH/US]; 3410 A South Oak, Austin, TX 78704 (US). RICHARDS-KORTUM, Rebecca [US/US]; 6410 Walebridge Lane, Austin, TX 78739 (US).			
(74) Agent: HIGHLANDER, Steven, L.; Arnold, White & Durkee, P.O. Box 4433, Houston, TX 77210 (US).			
		Published With international search report.	

BEST AVAILABLE COPY

(54) Title: METHOD AND APPARATUS FOR SUBSURFACE IMAGING



(57) Abstract

Methods and apparatus for subsurface imaging of a sample. An optical coherence topography system utilizes a scanning (30) probe (24) to scan radiation (40) relative to a sample to generate subsurface images (32).

**FOR THE PURPOSES OF INFORMATION ONLY**

Codes used to identify States party to the PCT on the front pages of pamphlets publishing international applications under the PCT.

AL	Albania	ES	Spain	LS	Lesotho	SI	Slovenia
AM	Armenia	FI	Finland	LT	Lithuania	SK	Slovakia
AT	Austria	FR	France	LU	Luxembourg	SN	Senegal
AU	Australia	GA	Gabon	LV	Latvia	SZ	Swaziland
AZ	Azerbaijan	GB	United Kingdom	MC	Monaco	TD	Chad
BA	Bosnia and Herzegovina	GE	Georgia	MD	Republic of Moldova	TG	Togo
BB	Barbados	GH	Ghana	MG	Madagascar	TJ	Tajikistan
BE	Belgium	GN	Guinea	MK	The former Yugoslav Republic of Macedonia	TM	Turkmenistan
BF	Burkina Faso	GR	Greece			TR	Turkey
BG	Bulgaria	HU	Hungary	ML	Mali	TT	Trinidad and Tobago
BJ	Benin	IE	Ireland	MN	Mongolia	UA	Ukraine
BR	Brazil	IL	Israel	MR	Mauritania	UG	Uganda
BY	Belarus	IS	Iceland	MW	Malawi	US	United States of America
CA	Canada	IT	Italy	MX	Mexico	UZ	Uzbekistan
CF	Central African Republic	JP	Japan	NE	Niger	VN	Viet Nam
CG	Congo	KE	Kenya	NL	Netherlands	YU	Yugoslavia
CH	Switzerland	KG	Kyrgyzstan	NO	Norway	ZW	Zimbabwe
CI	Côte d'Ivoire	KP	Democratic People's Republic of Korea	NZ	New Zealand		
CM	Cameroon			PL	Poland		
CN	China	KR	Republic of Korea	PT	Portugal		
CU	Cuba	KZ	Kazakhstan	RO	Romania		
CZ	Czech Republic	LC	Saint Lucia	RU	Russian Federation		
DE	Germany	LI	Liechtenstein	SD	Sudan		
DK	Denmark	LK	Sri Lanka	SE	Sweden		
EE	Estonia	LR	Liberia	SG	Singapore		

## DESCRIPTION

### METHOD AND APPARATUS FOR SUBSURFACE IMAGING

#### Background of the Invention

5        This application claims priority to provisional patent application Serial No. 60/083,785 filed May 1, 1998, entitled, "Fiber Optic Probe Device For Optical Coherence Tomography And Uses Therefor" by Rebecca Richards-Kortum, Andrés F. Zuluaga, and Urs Utzinger. The entire text of the above-referenced disclosure is specifically incorporated by reference herein without disclaimer.

#### 10    Field of the Invention

      The present invention relates generally to the fields of optical imaging. More particularly, it concerns apparatus and methods for generating two and three dimensional subsurface images of a sample, including both *in situ* and *ex situ* imaging of body tissues. In illustrative embodiments, devices are provided for  
15    minimally-invasive procedures such as colposcopic or oropharyngeal examinations, and miniturized devices are presented that may be used in endoscopic procedures.

#### Description of Related Art

      Cancer is one of the leading causes of death in the United States and in the world. In the United States alone, deaths from cancer are estimated to number  
20    560,000 in 1997 (*American Cancer Society Online. Cancer Facts and Figures*). Currently, diagnosis and treatment of cancer follow histopathologic evaluation of directed biopsies. However, the tissue removal necessitated by these techniques not only may alter the progression of the disease (Robbins and Kumar, 1984) but is also very costly. Improving the capability for *in situ* monitoring of disease progression  
25    could greatly enhance the ability to detect and treat cancer and precancer (Kelloff *et al.*, 1992).

#### Cervical Cancer

      In women, cervical cancer will account for an estimated 14,500 new cases and 4,800 deaths in 1997 (*American Cancer Society Online. Cancer Facts and Figures*).  
30    Its precursor, cervical intraepithelial neoplasia (CIN) refers to a tumor growth from the cervical epithelium (Robbins *et al.*, 1984; Harrison and Braunwald, 1987). Such

growth is believed to originate from a single mutant cell near the basal layer of the epithelium. Rather than follow the normal maturation process, the mutant cell continues to divide without control. This results in a growing, undifferentiated group of cells, which gradually spreads from the basal layer to the surface layer of the epithelium. The disease is considered pre-invasive when it is confined to the epithelium. If detected at this stage the disease is curable. Eventually the basal layer is compromised and the transformed cells invade the stroma. At this stage the disease is considered invasive.

The cervix has two distinct types of epithelia. A stratified squamous epithelium covers most of the cervix and a simple columnar epithelium covers the inside of the cervical canal. The interface between the two epithelia is called the squamo-columnar junction or the transformation zone (TZ), and is located at or near the os of the cervix (Burke *et al.*, 1991). The TZ is of particular importance because it is where virtually all precancerous and cancerous cervical lesions originate. The squamous epithelial layer is between 150 and 300  $\mu\text{m}$  deep, corresponding to tens of cell layers. It is separated from the stroma by a thin membrane called the basal lamina or membrane. Histologically the progression of the disease is characterized in terms of cell differentiation and organization from the basal layer to the surface of the epithelium (Burke *et al.*, 1991). Of greatest importance in the diagnosis of the disease are the changes of the epithelial cell nuclei. As the disease progresses, cells show an increase in the relative size of the nuclei with respect to the cytoplasm, and abnormal nuclear configurations during cell division. Since these cells are mitotically very active the cellular density is also increased.

Early detection of CIN has been crucial to the reduction of the mortality caused by disease over the last decades (Anderson *et al.*, 1988). Currently, cytologic techniques are of widespread use in the monitoring of gynecologic abnormalities. Unfortunately the accuracy of such techniques is not optimal. In a study of the accuracy of the Pap test, Fahey found that sensitivity ranged from 11 to 99% and specificity from 14 to 97% (Fahey *et al.*, 1995). This is attributed to variability in sample collection and reader error. If an abnormal Pap smear is detected, further examination is performed using a low power microscope called a colposcope.

Colposcopy is used to identify the extent and grade of the lesion, and to direct any biopsies to be taken. While highly sensitive, colposcopy is not very specific (Mitchell, 1994). This means that a large number of normal sites are classified as diseased. Colposcopy is only performed by trained experts, making the cost of more  
5 widespread screening with this method prohibitive. There is a need for more accurate, automated screening and diagnostic tools to identify cervical precancers.

#### Optical Diagnosis of Cervical Cancer

Recently, work done in the area of optical spectroscopy has been aimed at aiding in the diagnosis of cancer and precancer not only in gynecologic tissue  
10 (Ramanujam *et al.*, 1994) but also in other kinds of tissue (Alfano *et al.*, 1987; Hung *et al.*, 1991; Roy *et al.*, 1995; Schomacker *et al.*, 1992; Cothren *et al.*, 1990). Recent reviews in the field are found in (Nishioka, 1994; Richards-Kortum and Sevick-Muraca, 1996; Bohorfoush, 1996; Bigio and Mourant, 1997). These techniques attempt to classify the tissue being probed by effectively assessing its biochemical  
15 composition as evidenced by the light reflected, absorbed or emitted as Raman or fluorescence signals. They attempt to provide additional information that will result in better *in situ* diagnosis tools available, allowing for better diagnostic performance from less specialized personnel.

Another approach to improving diagnostic ability is to provide morphological  
20 information of the tissue, in the manner of x-ray, MRI or ultrasound imaging. These techniques, however, are not well suited for this particular task, as they do not provide immediate results in the first two cases and the last does not have the necessary resolution to detect the sub-millimeter lesions that characterize pre-invasive disease. Optical techniques that overcome the problems of multiple scattering in imaging have  
25 been developed and are being made available for use in medical screening and diagnostic. Notables in this category are confocal microscopy and optical coherence tomography.

Confocal microscopy is an imaging technique well suited for the evaluation of specimens in thick, turbid samples. This is due to its ability to reject light from  
30 outside the focal volume. The technique is well established and has been used extensively *in vitro* (Pawley, 1995) and applications for *in vivo* and endoscopic use

have been developed (Webb *et al.*, 1987; Smithpeter, 1997). Confocal microscopy has a resolution on the order of 1 to 2 microns, allowing it to resolve single cells and their nuclei. This makes it potentially an excellent tool for aiding diagnosis since it may provide near-histologic resolution images *in vivo*. However, confocal imaging is only possible at depths of several hundred microns, as image quality is degraded by the wavefront aberrations induced by the tissue and contrast is reduced by detected photons from outside the confocal volume.

### Optical Coherence Tomography

A number of time-, frequency-, and coherence-domain techniques have been investigated for biomedical imaging. Most investigations have concentrated on thick tissue specimens, where multiple scattering limits image resolution. A few studies have investigated time-resolved imaging of unscattered transmitted light or singly-backscattered light for imaging in relatively thin (<1-2 mm) tissues. However, the femtosecond temporal resolution required for imaging microstructure in this manner constrains the practicality of these techniques for medical applications. An alternative, more economical approach has recently gained prominence. This approach takes advantage of the coherence length of a broadband light source as a range gate, rather than the pulse duration of an ultrashort laser pulse. Techniques based on coherence-gating include the one dimensional ranging technique of optical coherence-domain reflectometry (OCDR), two-dimensional combined scanning/ranging techniques such as optical coherence (OCT) and optical coherence microscopy (OCM), and inherently two-dimensional techniques based on low-coherence holography. Of these, OCT has proven most promising in clinical applications due to its relative simplicity and low cost.

Optical coherence tomography (OCT) is an optical imaging technique that allows high-resolution cross-sectional imaging of tissue microstructure (Huang *et al.*, 1991). OCT is analogous to ultrasound imaging except that infrared light waves rather than acoustic waves are used. An optical beam is focused into the tissue, and the echo time delay of light reflected from internal microstructure at different depths is measured by interferometry. Image information is obtained by performing repeated axial measurements at different transverse positions as the optical beam is scanned

across the tissue. The resulting data constitute a two-dimensional map of the backscattering or reflectance from internal architectural morphology and cellular structures in the tissue.

OCT imaging is based on a classical optical measurement technique known as low coherence (or white light) interferometry, which has been used in optics to perform high precision measurements in optical fibers and optical components (Youngquist *et al.*, 1987; Takada *et al.*, 1987; Gilgen *et al.*, 1989). One of the first applications of low coherence interferometry to biological systems was pioneered by Fercher *et al.* for high precision measurements of axial eye length and corneal thickness (Fercher *et al.*, 1988; Hitzenberger *et al.*, 1992). Low coherence interferometry is analogous to ultrasound A mode or axial mode measurement. OCT is a powerful extension of the optical ranging concept, which permits the measurement of two-dimensional, cross-sectional images with micrometre resolution (Huang *et al.*, 1991; Swanson *et al.*, 1993).

Initially, OCT was applied to imaging the transparent tissue of the eye (Fercher *et al.*, 1993; Swanson *et al.*, 1993). Clinical studies have shown that OCT provides high-resolution cross-sectional images of a wide range of retinal macular diseases (Hee *et al.*, 1995a; Hee *et al.*, 1995b; Hee *et al.*, 1995c; Puliafito *et al.*, 1995). Recently, imaging to depths of 2 to 3 mm in nontransparent tissue was achieved by use of longer wave-lengths in the near infrared (Huang *et al.*, 1991; Fujimoto *et al.*, 1995; Schmitt *et al.*, 1994; Brezinski *et al.*, 1996; Schmitt *et al.*, 1995). The identification of *in vitro* pathology has been verified in tissue from the cardiovascular system and gastrointestinal tract (Brezinski *et al.*, 1996).

OCT technology is based on fiber optics, which are used in optical communications technology. Thus, OCT technology is robust, portable, low cost, and can be readily interfaced with optical fiber techniques to catheters and endoscopes. OCT has been investigated and reduced to clinical practice in ophthalmology. Preliminary clinical studies demonstrate that OCT can noninvasively image structures of the anterior eye and retina with unprecedented resolution (Huang *et al.*, 1991; Swanson *et al.*, 1993; Izatt *et al.*, 1994; Hee *et al.*, 1995a; Hee *et al.*, 1995b; Hee *et al.*, 1995c). OCT has been especially promising for the diagnosis and monitoring of

macular diseases (Puliafito *et al.*, 1995). Since quantitative information also can be obtained from OCT images, it also may provide the first objective clinical assessment of diseases such as glaucoma (Takada *et al.*, 1987).

OCT can overcome the problems of multiple scattering, allowing it to image sub-surface structure in tissue. OCT detects very faint reflections of laser light directed into the tissue and determines at what depth these reflections occurred. This results in an image of the relative reflectivity of the tissue below the surface. This is related to the properties of individual cells as well as the overall structure of the tissue, both of which change in the presence of disease.

With OCT, tomographic images of sub-surface biological microstructure are obtained with  $\sim 10\ \mu\text{m}$  spatial resolution (Clivaz *et al.*, 1992; Huang *et al.*, 1991; Izatt *et al.*, 1993; Swanson *et al.*, 1993; Youngquist *et al.*, 1987; Izatt *et al.*, 1993). The heterodyne optical detection scheme inherent to OCT provides sensitivity to backscattered signals as small as one part in  $10^{11}$  of the incident optical power, thus extremely faint reflections can be visualized. In OCT, the specimen to be interrogated is placed in the sample arm of an interferometer illuminated with a low-coherence light source (FIG. 2). Interference between light returning from the reference arm and light scattered from internal sample reflections occurs only when the optical path lengths in both arms of the interferometer are matched to within the source coherence length. Thus, scanning the reference arm while monitoring the envelope of the interferometric signal generates a map of tissue reflectivity versus optical depth or "A-scan," with axial resolution given by the coherence length. Cross-sectional images of tissue backscatter are built from sequential A-scans obtained while scanning the probe beam across the tissue surface. Resulting two-dimensional data sets are plotted as gray-scale images.

Rooted in work done for integrated optics testing (Youngquist *et al.*, 1987; Danielson and Whittenberg, 1987), OCT was brought into the fore of biomedical community by Huang *et al.* (1991). In this article they describe a fiber optic-based OCT system and compare sample images obtained *in vitro* with histologic preparations of the same samples. The tissues investigated were a human retina and a human coronary artery, both being structures of clinical importance.



The primary applications of OCT developed to date have been for high-resolution imaging of ocular structure (Swanson *et al.*, 1993; Schuman *et al.*, 1995; Puliafito *et al.*, 1995; Izatt *et al.*, 1995; Fercher *et al.*, 1988). Initial studies of OCT imaging in non-transparent media have also been reported (Izatt *et al.*, 1994; Izatt *et al.*, 1996; Pan *et al.*, 1995; Reitze *et al.*, 1997; Schmitt *et al.*, 1994; Tearney *et al.*, 1997). The axial point-spread function of the low-coherence interferometer is given by the autocorrelation function of the source optical field. For superluminescent diodes typically used in this application, coherence lengths can be as short as 15  $\mu\text{m}$ , and the autocorrelation function is very close to Gaussian as a function of depth. Thus, reflections more than a few coherence lengths away from the peak of the point-spread-function are very strongly rejected, much more strongly than out-of-focus reflections in a confocal microscope (Izatt *et al.*, 1994). The strong rejection of unwanted light allows for coherence-domain imaging up to 1.5 millimeters deep even in highly scattering tissues. OCT is attractive for clinical imaging for at least three reasons: (i) the typical OCT image has an axial resolution of 10  $\mu\text{m}$ , up to 10 times higher than any clinically available diagnostic imaging modality; (ii) because OCT systems can be constructed with fiber optical components used in telecommunications, they are relatively inexpensive and portable; and (iii) fiber optic systems can be incorporated into catheters or endoscopes, allowing high-resolution images of internal organ microstructure.

OCT is analogous to ultrasound B-mode imaging: reflections of light from biological tissue layers are detected instead of acoustic reflections. Imaging is performed by directing a focused beam of light into the biological tissue and measuring the delay time (echo delay) for the backscattered light to return to the instrument. Backscatter or reflections are returned from each microstructural feature within the tissue during a single axial (depth) scan. A cross-sectional image of the tissue is constructed by laterally scanning the light beam through the tissue and assembling adjacent axial scans (Huang *et al.*, 1991; Boppart *et al.*, 1997).

The ability to resolve fine structure deep in turbid media only one reason OCT is well suited for medical applications. Additionally, it is possible to implement the system in such a way that measurements can be made remotely by delivering the beam

through an optical fiber. This makes it amenable to medical use, where access is often restricted to the working channels of endoscopes. While the ability to measure OCT signals through optical fiber suggests relative ease in the adaptation of the method for probe-based delivery, only two such references are found in the literature to date. A radial-scanning, side-firing catheter-endoscope is described by Tearney *et al.* (Tearney *et al.*, 1996). The device consists of a rotating core within a sheath. The total diameter of the probe is 1.1 mm. The rotating core contains a fiber optic cable with a GRIN lens and a prism attached at the end. The prism redirects the beam so that the catheter "sees" in a direction perpendicular to its axis. First results of *in vitro* human saphenous vein were shown.

Sergeev *et al.* (1997) recently presented *in vivo* images obtained from a forward-firing endoscope. The endoscope uses "galvanometric principle" scanning to provide transverse coverage of close to 2 mm and piezoelectric fiber stretching to obtain up to 3 mm scan depths. The probe is about 3 mm in outer diameter and is designed to be used through the biopsy channel of a standard endoscope. Images have been shown of a number of human mucosal tissues in the respiratory gastrointestinal, urinary and genital tracts.

### Summary of the Invention

In one respect, the invention is an apparatus for subsurface imaging of a sample, including a radiation source, an interferometer, a scanning probe, and a detector. The interferometer is in optical communication with the source. The scanning probe is in optical communication with the interferometer and the sample, and it includes an optical fiber and a piezoelectric scanner. The optical fiber is configured to receive radiation from the radiation source and to direct the radiation toward the sample. The piezoelectric scanner is coupled to the probe and is configured to scan the radiation relative to the sample. The detector is in optical communication with the scanning probe.

In other aspects, the scanning probe may be a scanning side-looking probe including an optical element in optical communication with the fiber. The optical element may be configured to direct radiation from the fiber toward the sample in a

direction that is substantially non-parallel with the fiber. The piezoelectric scanner may include a piezoelectric bender. The scanning probe may also include a GRIN lens coupled to the optical fiber. The scanning probe may also include a sterilizable cover configured to cover at least a portion of the scanning probe. The scanning probe  
5 may also include an optical window coupled to the scanning probe adjacent the optical fiber. The scanning probe may also include an inner and outer tube enclosing at least a portion of the scanning probe.

In another respect, the invention is an apparatus for subsurface imaging of a sample, including a radiation source, an interferometer, a scanning probe, and a  
10 detector. The interferometer is in optical communication with the source. The scanning probe is in optical communication with the interferometer and sample, and it includes an optical fiber and a mirror scanner. The optical fiber is configured to receive radiation from the radiation source and to direct the radiation toward the sample. The mirror scanner is coupled to the probe and is configured to scan the  
15 radiation relative to the sample. The detector is in optical communication with the scanning probe.

In other aspects, the mirror scanner may include a mirror coupled to an electromagnetically powered micromotor.

In another respect, the invention is an apparatus for subsurface imaging of a  
20 sample, including a radiation source, an interferometer, a scanning probe, and a detector. The interferometer is in optical communication with the source. The scanning probe is in optical communication with the interferometer and sample, and it includes an optical fiber and a galvanometric scanner. The optical fiber is configured to receive radiation from the radiation source and to direct the radiation toward the  
25 sample. The galvanometric scanner is coupled to the probe and is configured to scan the radiation relative to the sample. The detector is in optical communication with the scanning probe.

In other aspects, the galvanometric scanner may include one or more permanent magnets in operative relation with the optical fiber.

30 In another respect, the invention is an apparatus for subsurface imaging of a sample, including a radiation source, an interferometer, a probe, and a detector. The

interferometer is in optical communication with the radiation source. The probe is in optical communication with the interferometer and the sample, and it includes an optical fiber and a spectroscopy module. The optical fiber is configured to receive radiation from the radiation source and to direct the radiation toward the sample. The spectroscopy module is in optical communication with the sample and is configured to measure optical spectroscopy of the sample simultaneously with optical coherence imaging of the sample. The detector is in optical communication with the probe.

In other aspects, the probe may be a scanning probe including a piezoelectric scanner configured to scan the radiation from the radiation source relative to the sample. The probe may be a scanning probe including a mirror scanner configured to scan the radiation from the radiation source relative to the sample. The probe may be a scanning probe including a galvanometric scanner configured to scan the radiation from the radiation source relative to the sample. The spectroscopy module may also include a dichroic mirror configured to direct the radiation from the radiation source into the optical fiber. The spectroscopy module may also include an optical fiber configured to direct radiation toward the sample. The spectroscopy module may be a multi-wavelength spectroscopy module that includes a spectrograph in optical communication with the probe. The optical spectroscopy may include fluorescence, reflectance, or Raman spectroscopy.

In another respect, the invention is an apparatus for subsurface imaging of a sample, including a radiation source, an interferometer, a probe, and a detector. The interferometer is in optical communication with the first radiation source. The probe is in optical communication with the interferometer and the sample, and it includes an optical fiber and a surface imaging module. The optical fiber is configured to receive radiation from the radiation source and to direct the radiation toward the sample. The surface imaging module is in optical communication with the sample and is configured to optically image the sample simultaneously with optical coherence imaging of the sample. The detector is in optical communication with the probe.

In other aspects, the probe may be a scanning probe including a piezoelectric scanner configured to scan the radiation from the radiation source relative to the sample. The probe may be a scanning probe comprising a mirror scanner configured

to scan the radiation from the radiation source relative to the sample. The probe may be a scanning probe comprising a galvanometric scanner configured to scan the radiation from the radiation source relative to the sample.

5 In another respect, the invention is an apparatus for subsurface imaging of a sample, including a radiation source, an interferometer, a probe, and a detector. The interferometer is in optical communication with the radiation source. The probe is in optical communication with the interferometer and the sample, and it includes an optical fiber and a therapeutic module. The optical fiber is configured to receive radiation from the first radiation source and to direct the radiation toward the sample.  
10 The therapeutic module is in optical communication with the sample and is configured to apply therapeutic radiation to the sample simultaneously with optical coherence imaging of the sample. The detector is in optical communication with the probe.

15 In other aspects, the probe may be a scanning probe including a piezoelectric scanner configured to scan the radiation from the radiation source relative to the sample. The probe may be a scanning probe including a mirror scanner configured to scan the radiation from the radiation source relative to the sample. The probe may be a scanning probe including a galvanometric scanner configured to scan the radiation from the radiation source relative to the sample.

20 In another respect, the invention is an apparatus for multi-dimensional subsurface imaging of a sample without scanning, the apparatus including a radiation source, an interferometer, a detector, and an imaging spectrograph. The radiation source is in optical communication with the sample. The interferometer is in optical communication with the radiation source. The detector is in optical communication  
25 with the interferometer and the sample. The imaging spectrograph is intermediate the interferometer and the detector.

In other aspects, the apparatus may also include an optically addressed spatial light modulator in optical communication with the imaging spectrograph, a coherent source in optical communication with the optically addressed spatial light modulator,  
30 and a cylindrical lens in optical communication with the optically addressed spatial light modulator. The apparatus may also include an optical fiber bundle in optical

communication with the interferometer and the sample. The optical fiber bundle may be configured to receive radiation from the radiation source and to direct the radiation through individual fibers of the optical fiber bundle toward the sample. The optical fiber bundle may include a one dimensional array of optical fibers. The optical fiber bundle may include a two dimensional array of optical fibers. The apparatus may also include a probe in optical communication with the radiation source and the sample, the probe housing at least a portion of the optical fiber bundle. The probe may be a side-looking probe including an optical element in optical communication with the fiber bundle, the optical element configured to direct radiation from the fiber bundle toward the sample in a direction that is substantially non-parallel with the fiber bundle. The probe may be a radially-looking probe including one or more angle polished fibers. The apparatus may also include a spectroscopy module in optical communication with the sample and configured to analyze the sample simultaneously with optical coherence imaging of the sample. The apparatus may also include a surface imaging module in optical communication with the sample and configured to optically image the sample simultaneously with optical coherence imaging of the sample. The apparatus may also include a therapeutic module in optical communication with the sample and configured to apply therapeutic radiation to the sample simultaneously with optical coherence imaging of the sample.

In another respect, the invention is an apparatus for multidimensional subsurface imaging of a sample without scanning, the apparatus including a confocal microscopy system and an optical fiber bundle. The confocal microscopy system includes a radiation source, an imaging spectrograph, and a detector. The imaging spectrograph is in optical communication with the sample. The detector is in optical communication with the sample. The optical fiber bundle is configured to receive radiation from the radiation source and to direct the radiation through individual fibers of the fiber bundle toward the sample.

In other aspects, the apparatus may also include an optically addressed spatial light modulator in optical communication with the imaging spectrograph, a coherent source in optical communication with the optically addressed spatial light modulator, and a cylindrical lens in optical communication with the optically addressed spatial

light modulator. The optical fiber bundle may include a one dimensional array of optical fibers. The optical fiber bundle may include a two dimensional array of optical fibers. The apparatus may also include a probe in optical communication with the radiation source and the sample, the probe housing at least a portion of the optical fiber bundle. The probe may be a side-looking probe including an optical element in optical communication with the fiber bundle, the optical element configured to direct radiation from the fiber bundle toward the sample in a direction that is substantially non-parallel with the fiber bundle. The probe may be a radially-looking probe including one or more angle polished fibers. The apparatus may also include a spectroscopy module in optical communication with the sample and configured to analyze the sample simultaneously with confocal imaging of the sample. The apparatus may also include a surface imaging module in optical communication with the sample and configured to optically image the sample simultaneously with confocal imaging of the sample. The apparatus may also include a therapeutic module in optical communication with the sample and configured to apply therapeutic radiation to the sample simultaneously with confocal imaging of the sample.

In another respect, the invention is a method for subsurface imaging of a sample, including the following steps. A radiation source, an interferometer in optical communication with the radiation source, a detector in optical communication with the interferometer, and an imaging spectrograph intermediate the interferometer and the detector are provided. Radiation from the radiation source is directed to the sample. Radiation from the sample is directed to the interferometer, to the imaging spectrograph, and to the detector. A multi-dimensional optical coherence tomography image of the sample is generated.

In other aspects, the method may also include providing an optically addressed spatial light modulator in optical communication with the imaging spectrograph, a coherent source in optical communication with the optically addressed spatial light modulator, and a cylindrical lens in optical communication with the optically addressed spatial light modulator. Output intensity of the imaging spectrography may be converted from incoherent to coherent with the optically addressed spatial light modulator, and a Fourier transformation may be performed with the cylindrical lens.

The method may also include providing an optical fiber bundle in optical communication with the interferometer and the sample, the optical fiber bundle configured to receive radiation from the radiation source and to direct the radiation through individual fibers of the fiber bundle toward the sample. The method may also include providing a spectroscopy module in optical communication with the sample and measuring optical spectroscopy of the sample simultaneously with optical coherence imaging of the sample. The method may also include providing a surface imaging module in optical communication with the sample and optically imaging the sample simultaneously with optical coherence imaging of the sample. The method may also include providing a therapeutic module in optical communication with the sample and applying therapeutic radiation to the sample simultaneously with optical coherence imaging of the sample.

In another respect, the invention is a method for subsurface imaging of a sample, including the following steps. A confocal microscopy system including a radiation source, an imaging spectrograph in optical communication with the sample, and a detector in optical communication with the sample are provided. Radiation from the radiation source is directed to the sample. Radiation from the sample is directed to the imaging spectrograph and to the detector. A multi-dimensional confocal microscopy image of the sample is generated.

In other aspects, the method may also include providing an optically addressed spatial light modulator in optical communication with the imaging spectrograph, a coherent source in optical communication with the optically addressed spatial light modulator, and a cylindrical lens in optical communication with the optically addressed spatial light modulator. Output intensity of the imaging spectrography may be converted from incoherent to coherent with the optically addressed spatial light modulator, and a Fourier transformation may be performed with the cylindrical lens. The method may also include providing an optical fiber bundle in optical communication with the sample and configured to receive radiation from the radiation source and to direct the radiation through individual fibers of the fiber bundle toward the sample. The method may also include providing a spectroscopy module in optical communication with the sample and measuring optical spectroscopy of the sample



simultaneously with confocal imaging of the sample. The method may also include providing a surface imaging module in optical communication with the sample and optically imaging the sample simultaneously with confocal imaging of the sample. The method may also include providing a therapeutic module in optical communication with the sample and applying therapeutic radiation to the sample simultaneously with confocal imaging of the sample.

The apparatus and methods described herein advantageously provide for, for instance, a portable system for the acquisition of OCT images. In one embodiment, such images may be acquired in the cervix at the time of colposcopy. The apparatus are transportable so that they can be rolled into and out of the patient examination rooms. The apparatus are small in size so that they fit in examination rooms. Further, the apparatus has a size allowing for insertion through dilated vagina while still allowing the physician some view. Finally, image acquisition times, which may be about 5 sec or less, in advantageously to minimize motion artifacts. Applications for the methods and apparatus described herein are vast and include, but are not limited to, analysis and detection of disease including cancers and pre-cancers (such as cervical, head and neck, colon, lung, esophageal, ovarian) and atherosclerosis. Applications also include industry, including, but not limited to, the semiconductor industry.

#### Brief Description of the Drawings

The following drawings form part of the present specification and are included to further demonstrate certain aspects of the present invention. The invention may be better understood by reference to one or more of these drawings in combination with the detailed description of specific embodiments presented herein.

**FIG. 1.** Schematic of a prior art Michelson interferometer. Shown are a source 10, a beamsplitter 14, a reference mirror 18, a detector 12, and a mirror 16.

**FIG. 2.** Schematic of a prior optical coherence tomography (OCT) setup. Shown are a source 10, a beamsplitter 14, a reference mirror 18, a signal 13, a detector 12, and a sample 20.

**FIG. 3.** Schematic of a fiber-optic based, OCT setup according to the present disclosure. The boxed area 22 corresponds to a cervical probe attachment functional element.

**FIG. 4 and FIG. 5.** Photo of a practical implementation of a portable, fiber-optic based, optical coherence tomography setup according to the present disclosure. The embodiment of **FIG. 4** includes a cervical probe attachment 31, a lock-in amplifier 32, a Galvanometer power supply 33, an SLD power supply 34, a Piezoelectric controller 35, and an Optics drawer 36. The embodiment of **FIG. 5** shows a detail of one optics setup and includes an SLD enclosure 37, a Photodetector 38, a Cervical probe handpiece 39, a Scanning retroreflector 40, a Variable pathlength cuvette 41, and a Fiber-optic coupler (50:50) 42.

**FIG. 6.** Photo showing an implementation of a fiber optic probe in accordance with the present disclosure. In this embodiment, the piezoelectric multimorph scans the focal spot of the GRIN lens 1 mm in the transverse direction. The outer diameter of the sterilizable cover is 18 mm. The sterilizable cover may minimize the time in between patients.

**FIG. 7.** Measured line scan of a smooth sample with  $-29.6$  dB reflectivity. The measured FWHM depth resolution is  $22.6\text{ }\mu\text{m}$  and the measured sensitivity is  $-94.4$  dB, indicating shot-noise limited performance.

**FIG. 8 and FIG. 9.** Measured period of a 500 lp/in ( $51\text{ }\mu\text{m}$  period) Ronchi grating. Each data point is the average of four measurements. The error bars correspond to  $\pm$  one standard deviation.

**FIG. 10.** Comparison of measured transverse resolution for a Ronchi grating under mounted and hand-held conditions. Good agreement is seen, confirming the lack of motion artifacts during acquisition time.

**FIG. 11 and FIG. 12.** Comparison of an OCT image (**FIG. 11**) and a phase contrast microscope image (**FIG. 12**) of fresh onion skin. The intensity scale in (**FIG. 11**) is in dB, and the scale bar in (**FIG. 12**) measures  $100\text{ }\mu\text{m}$ . Individual cells and cell layers are distinguishable in the OCT image. The sizes of the cells in the OCT image correspond well to the sizes observed in the phase contrast image.

**FIG. 13.** Sample image from scattering media *in-vivo*, showing the bottom lip of an adult male. 50 corresponds to the Probe shield, 52 to the Epithelium; 54 to the Lamina propria; 56 to the Submucosa; and 58 to the Muscle. 60 is the Shield-epithelium interface, 62 is a Blood vessel (longitudinal cut); 63 is a Blood vessel (transverse cut). The color scale is in dB.

**FIG. 14.** Transverse section through the contiguous cutaneous and red areas of lip of newborn infant (Copenhaver *et al.*, 1978). The field is 1mm by 1mm.

**FIG. 15.** Schematic of one embodiment of the distal end of the probe, showing Part A and Part B, including dimensions, material and assembly information. In one embodiment a removable cover, 25 cm long and 2 cm in diameter, slides over this portion providing protection from the environment and ease of sterilizability. In one embodiment, the probe, which may be of circular cross-section, may be about 240 mm long and about 20 mm in diameter. A multimorph piezoelectric translator, or another type of scanner as disclosed herein or known in the art, may scan the fiber and lens, in one embodiment, about 900  $\mu$ m perpendicular to the plane of the schematic.

**FIG. 16.** Schematic of one embodiment of Part A, the bottom part of the piezoelectric multimorph bender holder according to one embodiment. Dimensions for this embodiment are included. Polycarbonate (LEXAN) may be used as material for this part. Pieces may be held together by #1-72 screws at the indicated positions.

**FIG. 17.** Schematic of one embodiment of Part B, the piezoelectric multimorph bender protector. This piece may prevent damage to the piezo element during protective sleeve insertion and removal. Dimensions for this embodiment are included. Polycarbonate (LEXAN) may be used as material for this part. In this embodiment, this piece is to be glued to the bottom of Part A.

**FIG. 18.** Detail of one embodiment of the proxial (top) piece of the probe, including assembly information, showing Part C and Part D. The protective sleeve (outer tube) may be threaded so that it may be inserted and fixed by the locking nut. The threads also may allow for adjustment of the distance from the end of the optics at the distal end to an optical window such as a quartz window, on the protective sleeve. This results in adjustment of the depth of the focal spot on the

sample. In this embodiment, the threading should be the finest that can be made on all pieces (outer tube, inner tube, Part C, and Part D)

**FIG. 19.** Schematic of one embodiment of Part C, the top piece of the probe. Aluminum may be used as a material for this part.

5 **FIG. 20.** Schematic of one embodiment of Part D, the locking nut for the protective sleeve. Aluminum may be used as a material for this part.

**FIG. 21.** Schematic of one embodiment of the OCT probe, including materials, dimensions and assembly information.

10 **FIG. 22.** Schematic of one embodiment of an outer tube (protective sleeve), which may be made of stainless steel type 304.

**FIG. 23.** Schematic of one embodiment of an inner tube, which may be made of aluminum.

15 **FIG. 24.** Effect of increasing organelle content on scattering phase function. Typical amelanotic cell with 3% volume fraction of mitochondria (line 21), cell with 8% fraction of mitochondria (line 19), cell with 8% volume fraction of melanin (line 17).

**FIG. 25.** Block diagram of a system to measure fluorescence and reflectance spectra, according to the present disclosure.

20 **FIG. 26.** *left* - white light photograph of center of ovarian cyst, *right* - TRICT fluorescence photograph of center of ovarian cyst.

**FIG. 27.** Phase contrast image of epithelial cell before (left) and after (right) addition of acetic acid.

25 **FIG. 28.** Measured phase functions of OVCA420 cells before (bottom line) and after (top line) addition of 3% acetic acid.

**FIG. 29.** Predicted phase function for ovarian epithelial cell at 514.5 nm (line 27), 780 nm (line 25) and 2  $\mu$ m (line 23) wavelengths.

30 **FIG. 30.** Schematic of a no-moving-parts OCT system for acquiring 2 or 3-dimensional subsurface images in real time according to the present disclosure. In this embodiment, the spectrograph is an imaging spectrograph. Image processing may be performed after images are acquired electronically or in real-time by optical means

before the image reaches the CCD camera CCD1. The reference path and reference mirror Mref are shown unfolded and may be implemented in the sample light path by the use of a partially reflecting mirror before the sample. The system is well suited to accommodate modular functional attachments. The shaded region shows one such modular functional attachment, in this case a multi-wavelength fluorescent attachment. Other modules may include, for example, i) fluorescence imaging; ii) reflectance imaging; or iii) therapeutic light delivery. It is to be understood that such modules may be implemented with a "standard" system, *i.e.* a system having moving parts.

FIGS. 31- 34. Schematic representations of OCT system modules according to the present disclosure. FIG. 31 shows one embodiment of a full field surface fluorescence module. FIG. 32 shows one embodiment of a full field surface imaging module. FIG. 33 shows one embodiment of a therapeutic laser module. FIG. 34 shows one embodiment of a multiwavelength fluorescence module.

FIG 35. Schematic of a fiber-optic probe based, no-moving-parts OCT system for acquiring 2 or 3-dimensional images in real time according to the present disclosure. Shown are a polarizing beamsplitter (PBS), a quarter waveplate (QW), a dichroic mirror, a fiber bundle, various optics, a partial mirror, a sample, a module, an imaging spectrograph, an OASLM (optically addressed spatial light modulator), a beamsplitter, a readout laser, and a CCD camera. In this embodiment, the fiber coherent array is used for delivery and collection. The imaging spectrograph is used to resolve transverse information spatially as well as depth information spectrally. Although illustrated as an OASLM, it will be understood that any device suitable for converting the spectrograph output intensity from incoherent to coherent and then performing the required Fourier transformations may be substituted therewith.

FIG. 36. Schematic of a system for 3-dimensional imaging with no moving parts, by separating the different lines in the imaging bundle optically or mechanically, and re-directing each line to a different imaging spectrograph-camera combination.

**FIGS. 37.** Schematic of fiber bundle of FIG. 36. In this embodiment, each line,  $L_1$  through  $L_n$  is directed to its corresponding Spectrographs, Spectrographs 1 through n.

**FIG. 38.** Schematic of a fiber bundle for three dimensional imaging  
5 utilizing a single spectrograph.

**FIG. 39.** Schematic of one embodiment of side firing probes according to the present disclosure.

**FIG. 40A.** Schematic of one embodiment of radially-looking fiber bundle according to the present disclosure. The radial pattern may be achieved through the  
10 use of angle-polished individual fibers to re-direct the radiation, as shown. Other embodiments may make use of rotating mirrors to achieve a radial pattern. The mirrors may be coupled to a micromotor suitable for generating rotation.

**FIG. 40B.** Schematic of another embodiment of radially-looking fiber bundle according to the present disclosure. The radial pattern may be achieved  
15 through the use of mirrors, which may be multi-faceted, positioned one per fiber in this embodiment. A collar or other suitable device may be used to align the fibers and mirrors.

**FIG. 41.** Image of ovarian tissue obtained *in vitro*. A cyst was located approximately 250  $\mu\text{m}$  below the tissue surface.

**FIG. 42.** Schematic representation of bending of a bi/multimorph piezoelectric element according to the present disclosure. The location of the fiber  
20 and lens according to this embodiment are shown.

**FIG. 43.** Schematic of an embodiment utilizing a scanning probe including a mirror scanner configured to scan radiation from an optical fiber relative  
25 to a sample. Although not shown, the scanning mirror may be coupled to a micromotor suitable for generating rotation. Dimensions for this embodiment are also given.

**FIGS. 44 - 46.** Schematic of one embodiment of a piezoelectric stack-actuated, lever arm probe. Sample components and dimensions are illustrated.

**FIG. 47.** Schematic of a piezoelectric Bi/multimorph scanning probe,  
30 allowing for side imaging by the addition of an optical element (here, a prism but

which may include another component such as a mirror). Fiber 82 is coupled to GRIN lens 84 and piezoelectric bender 80. Optical element 86 directs radiation in a side-looking pattern substantially non-parallel to the probe body.

FIG. 48. Schematic of a variation on a current technology (Tearney patent) for a radial-firing catheter tip. This embodiment makes use of a micromotor 90 near the tip of a rotating mirror 92, allowing for the complete catheter to be flexible, except for a few millimeters at the tip. Rotation may also be more reliable without the torsion on the shaft in their design. Also shown is a fiber 82 coupled to a GRIN lens 84.

FIGS. 49 and FIG. 50. Schematics of a variation in the optics of an OCT probe to allow for surface imaging while acquiring OCT images. The addition of an imaging bundle 102 to the tip of the probe may add visual feedback, helping with probe placement. The system may be implemented with common optics (as shown, the GRIN lens 84 is shared by the OCT and imaging fibers 102) or with separate optics.

FIG. 51 and FIG 52. Schematics of a galvanometer based one dimensional scanning mechanism for OCT (and other probes -- the probe shown has a probe head 108 and a fiber 82). Electromagnets 112 exert variable force on a spring/bar 106 causing it to move (see arrows in FIG. 51) over controllable distances. The tip may be moved in a raster pattern or another pattern by adjusting the positions of the magnets appropriately. The magnets may be permanent magnets or electromagnets.

FIGS. 53 and 54. Schematic of galvanometer-based two dimensional scanning probes. The tip may be moved in a raster pattern or another pattern by adjusting the positions of the magnets appropriately. The magnets may be permanent magnets or electromagnets.

FIG. 55. Schematic representation of a spatially-resolved spectral interferometer. Depth in the sample (z) is encoded as wavelength-dependent spatial frequency in the spectrogram; transverse information (x) is imaged directly on the spectrogram. The inset shows a fiber optic delivery system, suitable for 2 or 3-dimensional image acquisition.

FIG. 56. Schematic of a test sample used in Example 8.

FIG. 57. Single-frame image of the test sample used in Example 8.

FIG. 58. Schematic representation of a Fourier domain OCT setup in accordance with the present disclosure. A broadband source illuminates a Michelson interferometer as in time domain methods but the output is spectrally, rather than  
5 time, resolved by means of a spectrograph and an array detector (a camera in the diagram).

FIG. 59. Schematic representation of a Fourier-domain OCT system with no moving parts in accordance with the present disclosure. The system illustrates the potential to add multifunctional modules so that other measurements may be  
10 acquired simultaneously.

FIG. 60. Schematic of an all-optical, Fourier domain OCT system in accordance with the present disclosure.

#### Description of Illustrative Embodiments

15 OCT is an optical ranging technique that uses a broadband source in an interferometer to resolve depth information. A Michelson interferometer is most commonly used to implement the technique, although equivalent setups using a Mach-Zehnder interferometer and spectral techniques have also been reported (Fercher *et al.*, 1994; Bail *et al.*, 1996).

20 FIG. 1 shows a diagram of a Michelson interferometer. Light from source 10 is collimated and passes through a beamsplitter 14. A portion of it goes through, is reflected by mirror 16 and returns to the beam splitter 14. The rest of the light is initially reflected by the beamsplitter 14, then reflected by moveable mirror 18 and returns to the beamsplitter 14. At the beamsplitter 14 the two beams recombine and  
25 are focused into the detector 12. The intensity at detector 12 is determined by the interference of the light from each arm of the interferometer. Thus, as mirror 18 moves the measured intensity cycles as the system goes from constructive to destructive interference. The frequency  $f$  of this oscillation is calculated as:

30

$$f = \frac{2v}{\lambda}$$

[Equation 1]



where  $v$  is the speed at which mirror 18 is moving,  $\lambda$  is the wavelength of the light, and the factor of two is due to the fact that light travels twice along each arm.

If the source 10 has a finite bandwidth, each monochromatic element will contribute a perfectly periodic pattern with the frequency determined by the wavelength. When  $h$  see (FIG. 1) is zero, all of the components add in phase and a large peak is observed. As mirror 18 is displaced, the independent contributions start dephasing with respect to each other resulting in partially destructive interference. This reduces the amplitude of the oscillating pattern until eventually the phases are completely randomized and a constant value is reached. The width of the envelope of the oscillating pattern is therefore a function inversely related to the bandwidth of the source. This width is referred to as the coherence length of the source and it characterizes the path difference after which interference will not occur. It is also a function of the source power spectral density (Goodman, 1985). In the case of a gaussian power spectral density, the envelope is also gaussian in shape and its width is given by

$$l_c = \frac{2 \cdot \ln(2)}{\pi} \cdot \frac{\lambda^2}{\Delta\lambda} \quad [\text{Equation 2}]$$

where  $l_c$  is the coherence length of the source,  $\lambda$  is the central wavelength of the source and  $\Delta\lambda$  is its FWHM (full width at half maximum) bandwidth. For a superluminescent diode (SLD) typically used in OCT,  $\lambda = 850$  nm and  $\Delta\lambda = 25$  nm yielding a coherence length of 12.75  $\mu\text{m}$ .

Obtaining ranging information from this scheme is illustrated in FIG. 2. The set up of FIG. 2 includes Broadband source 10; Beamsplitter 14, Reference mirror 18; Sample 20; Detector 12 and Detected signal 13. Interference fringes are seen only when reflections from the sample match the optical pathlength of the reference mirror. Let  $M_s$  in FIG. 1 be replaced by a sample 20 made up of two layers with different indices of refraction ( $n_1$  and  $n_2$ ). If mirror 18 is then scanned with a constant velocity  $v$ , the detector is going to see fringes of frequency  $f$  given by Equation 1, with a gaussian envelope of width given by Equation 2, when the optical path length to

mirror 18 and a reflection site in the sample are matched within a coherence length. This is shown in FIG. 2:

The envelope of this signal is obtained by mixing it with a reference sinusoid at frequency  $f$  and low-pass filtering. The optimum bandwidth of the low pass filter is given by  $2\Delta f$ , (Swanson *et al.*, 1992) where:

$$\Delta f = f \cdot \frac{\Delta \lambda}{\lambda} \quad [\text{Equation 3}]$$

The amplitude of the envelope is proportional to the square root of the reflectivity of the interface (Schmitt *et al.*, 1993). The overall result is analogous to an ultrasound A-scan, a reflectivity profile with depth resolution in the order of  $l_c$ . An image may be assembled by a collection of line scans obtained while scanning the beam in a transverse direction.

The sensitivity limit of the instrument is characterized by a signal to noise figure. Assuming shot-noise-limited detection this is given by (Swanson *et al.*, 1992):

$$SNR = \frac{1}{2} \cdot \frac{\eta P_s}{h\nu} \cdot \frac{R_s}{NEB} \quad [\text{Equation 4}]$$

where  $\eta$  is the quantum efficiency of the detector,  $P_s$  is the power delivered to the sample,  $h$  is Planck's constant,  $\nu$  is the optical frequency,  $R_s$  is the sample reflectivity and  $NEB$  is the noise equivalent bandwidth of the low-pass filter. The heterodyne detection scheme implemented in OCT results in sensitivities in the order of 100 dB (Youngquist *et al.*, 1987; Izatt *et al.*, 1995; Fercher, 1997; Hee *et al.*, 1994; Fujimoto *et al.*, 1995), allowing for imaging deep in turbid media. Note that Equation 4 indicates that there is a penalty to be paid for high-speed imaging, as this will increase the NEB. The same effect results from an increase in the source bandwidth, indicating a tradeoff between depth resolution and sensitivity at constant power.

A gross estimate of the greatest depth possible to image is easily calculated, considering that 100 dB corresponds to an attenuation of 5 orders of magnitude or 11.5 mean free paths (mfp). More detailed models including numerical aperture

(confocal) and multiple scattering effects can be found in (Izatt *et al.*, 1994; Pan *et al.*, 1995; Knuettel *et al.*, 1996; Schmitt *et al.*, 1994) and confirm the validity of the estimate. The actual depth that can be measured depends on the type of tissue. Estimates rely on optical property characterizations such as  $\mu_s$  and  $\mu_a$  which vary significantly. A study using OCT (Schmitt *et al.*, 1993) estimated  $\mu_s$  values for *in-vivo* human epidermis in the range of 50 to 150  $\text{cm}^{-1}$  at 800 nm. An extensive survey in (Welch and van Gemert, 1995) shows a number of values for different tissue types under different conditions. Table 1 shows some values for *in-vitro* tissue around 633 nm, the longest wavelength for which properties were consistently reported. In the near-infrared region of the spectrum, scattering significantly dominates absorption (Cheong *et al.*, 1990) so  $\mu_s$  is equal to  $\mu_t$  for practical purposes.

TABLE 1

OPTICAL PROPERTIES OF SELECTED TISSUES *IN VITRO*

ALL TISSUES ARE HUMAN UNLESS NOTED OTHERWISE

Tissue Type	$\lambda$ (nm)	$\mu_t$ ( $\text{cm}^{-1}$ )	$\mu_s$ ( $\text{cm}^{-1}$ )
Aortic intima	633	175	
Aortic media	633	312	
Aortic adventiva	633	201	
Uterus	635	394	
Prostate tumor (rat)	633	271	
Dermis	633	190	
Epidermis (pig)	633		492 +/- 17
Dermis (pig)	633		289 +/- 7
Whole blood	630	3670	

This illustrates that even in the absence of a strong absorber such as blood, the total imaging depth can vary by a factor of  $e^{10}$  (the difference between  $\mu_t=50$  and  $\mu_t=500$ ) or about 22000.

In one embodiment, the system may be used in the non-invasive characterization of precancerous lesions in the cervix. These lesions are histologically classified by the depth of dysplastic epithelial cells, with the epithelium roughly divided in thirds. The instrument should therefore be able to sufficiently resolve each  
5 third of the epithelium. For cervical epithelial depths of 150 to 300  $\mu\text{m}$ ., this requires depth resolution of at least  $(150/3)/2.2 = 22.7 \mu\text{m}$  with coverage of 300  $\mu\text{m}$ . Given the variability of reported optical properties of tissue, it is convenient to determine penetration depth ranges for a given instrument sensitivity and feature reflectivity. The source of signal is assumed to be index of refraction mismatch (Dunn *et al.*,  
10 1996), at normal incidence. For an index mismatch of 0.05, the resulting reflectivity is  $1.313 \times 10^{-3}$ . An OCT system with sensitivity of -100 dB can detect a reflectivity of  $10^{-10}$ . Assuming Beer's law with  $\mu_t$  between 50 and 500  $\text{cm}^{-1}$  the instrument would have an imaging depth between 164  $\mu\text{m}$  and 1.64 mm. At -94.6 dB this range changes to 151  $\mu\text{m}$  to 1.51 mm, while at -110 dB sensitivity the range is 187  $\mu\text{m}$  to 1.87 mm.  
15 It should be noted that these are maximum estimates, since they only account for the signal attenuation due to scattering and absorption. The source's short coherence length further reduces the imaging depth estimates since a photon which was multiply scattered will have traveled too long a path to interfere with the corresponding reference photon, even if it makes it back to the detector.

20 A system was designed and built according to these specifications and is illustrated in FIG. 3. It consists of 2 functional elements: a core OCT system and a cervical probe accessory. The complete system may be enclosed in a rolling, 19-inch rack mount 30 inches high and 23 inches deep shown in FIGS. 4 and 5. The control computer and monitor bring the total height to 54 inches. The probe attachment  
25 extends, in one embodiment, extends 9 feet, enclosed in a flexible protective covering. The core OCT system in the embodiment of FIG. 3 is made up of a broadband source, a Michelson interferometer and detection and control electronics. The cervical probe consists of relay and focusing optics, and a translation mechanism.

#### Core OCT System

30 The source used for the OCT system of FIG. 3 is a superluminescent diode 40 (SLD) model C86063E-15 from EGandG Optoelectronics Canada (Quebec, Canada).

It outputs 417  $\mu$ W of optical power from a single mode fiber (5/125 core/cladding). The SLD 40 has a FWHM bandwidth of 22.8 nm centered at 856.2 nm, yielding a theoretical FWHM resolution of 14.2  $\mu$ m. The SLD 40 is powered by a 06DLD201 diode laser driver from Melles-Griot (Irvine, CA) and is thermoelectrically cooled by a TC6 temperature controller (EG and G Jusdon; Montgomeryville, PA).

The Michelson interferometer of FIG. 3 was completely implemented with fiber optics. A 50:50, 2  $\times$  2 coupler (Gould Fiber Optics; Millersville, MD) is used to split the wavefronts and mix them again. This is a very convenient implementation that minimizes alignment in the system since the fibers are terminated with standard FC single mode connectors. The fiber outputs that are to be collimated in air are angle polished in order to minimize back-reflections. To implement the scanning reference mirror, the output of the reference arm of the interferometer is collimated to about 10 mm by an achromat (Melles-Griot 01LA0024) and is directed onto a 7 mm corner cube retroreflector 30 (Edmund Scientific; Barrington, NJ). The retroreflector 30 is mounted on a custom-made swinging arm that is actuated by a G3 series galvanometer from General Scanning (Watertown, MA). The galvanometer can drive the total inertial load at up to 15 Hz while translating the retroreflector 1.82 mm. Initial prototypes translated the reference arm mirror using a motorized linear stage. Using a galvanometer for depth scanning in the reference arm results in much smoother motion, which in turn results in a much cleaner signal frequency spectrum. Filtering out the noise can thus be more efficient. When used without the cervical probe accessory, the sample arm output is collimated by an achromat (Melles-Griot 06LAL027) and then focused on to the sample with appropriate optics. Since polarization balance between the two arms of the interferometer is important, a polarization controller (General Photonics; Chino, CA) was inserted into the reference arm.

A New Focus model 2001 silicon photodiode 36 (New Focus; Sunnyvale, CA) detects the optical signal. The detector 36 has adjustable gain settings and low- and high-pass filtering settings which are used to pre-filter the signal. Envelope detection of the signal is done with a 7260 DSP lock-in amplifier (EG and G Instruments; Workingham, United Kingdom). The output of the lock-in amplifier is digitized to 16

bits by a National Instruments AT-MIO16X multi function card (National Instruments; Austin, TX) and displayed on the host computer screen. The AT-MIO16X also controls the galvanometer motion and provides a synchronization signal for accessories. The lock-in amplifier is controlled *via* a GPIB card (National Instruments). The entire system is controlled through LabVIEW (National Instruments) through a graphical user interface.

The system also has a provision for a visible aiming beam on the sample. This is implemented by placing a 90:10,  $2 \times 1$  fiber coupler in between the output of the interferometer and the detector. The 90% arm is directed to the photodetector 36 while a visible diode laser 38 (Wave Optics; Mountain View, CA) is coupled into the 10% arm. The result is a visible spot in the same place illuminated by the invisible SLD. Data acquisition and conditioning may be accomplished with computer 32 and acquisition agent 34, which may be integral with computer 32.

#### Cervical Probe

The cervical probe 24 includes, in one embodiment, a rigid endpiece, 25 cm in length and 18 mm in diameter, at the end of a 250 cm. flexible protecting tube. Light from the core OCT system is coupled into a  $5/125 \mu\text{m}$ . (core/cladding) single mode fiber 26 (Flexcor 780 by Corning; Corning, NY) and delivered to the end of the probe. The fiber is the same kind of fiber that is used in the 50:50  $2 \times 2$  coupler. The endpiece consists of an outer, removable shield capped by a 2 mm optical window, such as a quartz window. The shield is sterilizable and the availability of several shields considerably reduces the time needed in between measurements on different patients. The core of the endpiece is a support for the delivery optics and the transverse scanning actuator. Delivery optics include a 0.29 pitch GRIN lens that focuses the fiber output to a spot size of about  $15 \mu\text{m}$  at a distance of approximately 6 mm from the lens face. The confocal parameter (depth of field) is  $207 \mu\text{m}$ . In one embodiment, the lens and fiber assembly may be mounted on the surface of a piezoelectric device, such as a piezoelectric multimorph bender (Dr. Lutz Picklemann Piezomechanik, GmbH; Munich, Germany) which provides  $900 \mu\text{m}$  of motion at the tip. The multimorph is controlled by a BMT 60 multimorph controller (Piezomechanik). A custom-built board synchronized with the data acquisition

process modulates the output of the BMT 60. The board is designed to provide a sawtooth output which will translate the piezo bender by a user-selectable 10 or 20  $\mu\text{m}$  per depth scan of the reference mirror in the core OCT system. Full control and synchronization of this board is achieved through LabVIEW via the AT-MIO16X card.

The attachment of the cervical probe 24 necessitates some modifications in the core OCT system. First, the optical path lengths on both arms of the interferometer must be matched. Since the optical distance in the sample arm is increased by the addition of the fiber probe, a similar length of fiber must be inserted in the reference arm. The length of this compensation fiber must be within 1 mm. of the total optical length of the probe attachment. This is easily implemented since the fibers are terminated by connectors. Dispersion in both arms of the interferometer must also be matched (Clivaz *et al.*, 1992) in order for the resolution of the system to be optimal. While the fiber lengths can readily be matched to within a few millimeters, the GRIN lens in the cervical probe introduces some unknown dispersion. In order to compensate for this, a variable length, cylindrical cuvette 28 was introduced in the sample arm. The cuvette 28 was then filled with different fluids and the resultant resolution observed. Deionized, ultra filtered water gave the best results of the fluids tried and is thus currently used.

## 20 Resolution, Coverage and Sensitivity

The three most important parameters that characterize an imaging system are its resolution, field of view and sensitivity. In OCT, the limit of depth resolution is a function of the source wavelength and bandwidth (Equation 2). The source used in one embodiment has a center wavelength of 856.2 nm and a FWHM bandwidth of 22.8 nm. This results in a theoretical limit of 14.2  $\mu\text{m}$  depth resolution. FIG. 7 shows a measurement of a smooth sample with reflectivity of -30 dB. This was achieved by measuring the reflection from the interface between the quartz probe shield window and air. The measured depth resolution is 22.6  $\mu\text{m}$ . The discrepancy is due to differences in the dispersion characteristics of the sample and reference arms of the interferometer. The GRIN lens is especially problematic in this respect since its dispersion varies as a function of position within the element. The higher dispersion

introduced by the GRIN lens in the sample arm was compensated by introducing variable pathlength cuvette 28. This allowed for both pathlength and dispersion control with a single element. The cuvette was filled with deionized water. Water's lower dispersion partially compensated for the higher dispersion of the GRIN element.

5 It's ready availability made it also very attractive choice.

Equation 4 allows calculation of the minimum detectable reflectivity. With  $\text{SNR} = 1$ , the detector quantum efficiency  $\eta = 0.9$  at 855 nm, the power delivered to the sample  $P_s = 75 \mu\text{W}$  and  $\text{NEB} = 50 \text{ kHz}$ , the smallest resolvable reflectivity is -94.6 dB. A measurement one standard deviation above the noise mean is considered  
10 the limit of detectability (Izatt, 1997). The sensitivity thus measured from FIG. 7 is -94.4 dB, indicating that the measurement is shot-noise limited. It should be noted that the laser exposure is well below the ANSI standard for minimum permissible exposure on skin, which is 132  $\mu\text{W}$  for the current configuration.

FIGS. 8 and FIG. 9 shows a calibration measurement for the system's  
15 transverse coverage and resolution. The measurement was performed by placing the probe shield in contact with a Ronchi grating of 500 line pairs per inch. This corresponds to a spatial period of 51  $\mu\text{m}$ . The lines of the grating were oriented perpendicularly to the transverse scanning direction of the probe, and water was added in between the surfaces as an index matching medium. The image obtained is shown  
20 in FIG. 8. Twenty lines, viewed as bright bars, are appreciable indicating coverage of 1 mm. Note that the signal from a sample in contact with the probe shield window plane does not appear at a constant depth. This is because the piezo multimorph moves the lens in an arc and the window surface is flat. This is a feature observed in all measurements performed with the protective shield on the probe.

25 Resolution in the transverse direction was determined by measuring the period of the Ronchi grating. This was done by holding the probe in an inverted position and placing the grating on the shield with a drop of water as index matching fluid. FIG. 9 shows the results obtained by averaging 4 different measurements. The measured period is in good agreement with the 51  $\mu\text{m}$  expected value indicating that the  
30 transverse resolution of the system is 10  $\mu\text{m}$ . A slight dependence of this resolution with the location on the measured field is seen. The lower relative transverse



positions in FIG. 9, corresponding to the left side of the images, have a slightly longer measured period. This nonlinearity of the transverse field is also a result of the circular path imparted by the transverse motion actuator.

Empirical results and suggestions from surgeons involved in previous studies suggested that image acquisition times of 5 sec or less would minimize motion artifacts. In the image collection scheme, each depth scan is acquired at 30 Hz and is deemed free of motion artifacts. The collection of 100 depth scans takes 3.5 sec (including some display overhead) and is much more susceptible to this kind of degradation. In order to quantify possible motion artifacts, the same Ronchi grating used for lateral resolution and coverage was measured under conditions simulating measurement during colposcopy. This was done by holding the probe from the proximal end of the endpiece and measuring the grating, which was being held in between an individual's hand and the probe. Water was also used as index matching fluid. The measured period of the grating in this configuration was compared to the previously measured period. The results are shown in FIG. 10, showing excellent agreement and confirming the lack of significant motion artifacts during the 3.5 sec acquisition time.

#### Imaging of Biological Media

Once system specifications were confirmed, biological samples were measured. First, a sample of fresh onion skin was measured. Onion skin was chosen for its large, clearly defined structures, ease of handling and availability. FIGS. 11 and 12 show a comparison of an OCT image and a phase contrast image of onion skin. It should be noted that this measurement was performed without the probe shield. The intensity scale of the OCT image is in dB. The scale bar on the top right of FIG 12 measures 100  $\mu\text{m}$ , making the field about 600 by 400  $\mu\text{m}$ . The field of the OCT image is 1000 by 500  $\mu\text{m}$ . Good agreement is seen between the observed features in both images. The sample is seen to have a top layer of cells with round shapes, 75 to 100  $\mu\text{m}$  in diameter. Above this first layer of cells are thin membrane layers that are seen to be highly scattering in the OCT image. Beneath the top layer of cells the cells become larger and acquire a more polygonal shape. The OCT image shows good contrast between the cell walls and the cellular contents up to 500  $\mu\text{m}$ .

The second biological sample measured was the inside of the bottom lip of an adult male. The measurement, shown in FIG. 13 was performed *in-vivo* in 3.5 sec. This measurement was performed with the probe shield in contact with the sample. The two surfaces were index matched with a drop of water. The image spans a field  
5 800 by 1000  $\mu\text{m}$  and shows clearly distinguishable features. Region *S* corresponds to the probe shield window and is characterized by the absence of signal. *E* corresponds to the epithelial layer, which in the oral cavity is of the stratified squamous type as in the cervix. The epithelium is supported by a layer of densely packed connective tissue called the lamina propria (*LP*), which is seen to be highly scattering in the OCT  
10 image. The lamina propria is connected to the underlying muscle layer by a layer of loose submucosal tissue (*SM*) showing slightly less scattering. Bundles of skeletal muscle (*M*) make up the bulk of the lip, corresponding to the bottom of the image. The epithelial surface is seen flattened by contact with the probe shield. A high index mismatch at the boundary, even in the presence of water as an index matching  
15 medium, results in a strong back reflection (61). The epithelium is seen to have a fairly constant thickness of 150  $\mu\text{m}$ . The interface of the epithelium and the lamina propria is clearly distinguishable. The layer of dense connective tissue is seen to vary in thickness between 50 and 100  $\mu\text{m}$ . The border between the two layers of connective tissue is not as well defined as that of the epithelium and the lamina  
20 propria, and is best appreciated toward the right of the image. The submucosal connective tissue is seen to vary in thickness similarly to the lamina propria. It is interesting to note that structures are visible within the submucosal layer. Examples of blood vessels, characterized by their strong absorption, are shown by arrows 62 and 63 in longitudinal and transverse cuts respectively. While the line of demarcation  
25 between the submucosal layer and the muscle layer is well defined, little detail is observed in the weakly scattering muscle layer. FIG. 14 shows a histologic preparation of the lip of a newborn child. The image is seen to have good feature correspondence to the measured OCT image.

The performance of an OCT system in accordance with the present disclosure  
30 assembled was found to perform up to specification in all categories. Resolution was measured to be 22.6  $\mu\text{m}$  in depth and 10  $\mu\text{m}$  transversely, with coverage of at least 1

mm in either direction. The instrument was measured to have a sensitivity of -94.4 dB in reflectivity, indicating that detection is shot-noise limited. The image acquisition time was measured to be 3.5 sec for an image field measuring 1mm by 1mm.

- 5 Images from biological media were successfully acquired. OCT imaging of plant cells in fresh onion skin showed excellent correspondence with images observed through a phase contrast microscope. Imaging of human epithelial tissue *in-vivo* was also successful. Several layers of tissue were clearly distinguishable, notably the epithelial layer. This suggests that OCT imaging may be used successfully to  
10 determine the grade and extent of precancerous and cancerous lesions. It is also significant that blood vessels may be detected, as these often accompany carcinogenesis.

#### Examples

- The following examples are included to demonstrate preferred embodiments  
15 of the invention. It should be appreciated by those of skill in the art that the techniques disclosed in the examples which follow represent techniques discovered by the inventors to function well in the practice of the invention, and thus can be considered to constitute embodiments for its practice. However, those of skill in the art should, in light of the present disclosure, appreciate that many changes may be  
20 made in the specific embodiments that are disclosed and still obtain a like or similar result without departing from the spirit and scope of the invention.

#### Example 1 -- Construction of the OCT Probe

##### Assembly of the OCT Probe Device

- A system according to the present disclosure is a fiber optic-based Michelson  
25 interferometer with a galvanometer arm scanning a retroreflector in the reference arm. Delivery to the sample is through a fiber optic probe terminated by a GRIN lens. This provides a focal distance of 5 mm with a 5.6  $\mu$ m spot diameter. The end-firing probe has a rigid endpiece with removable, sterilizable covers 25 cm in length and 2 cm in diameter. The endpiece is terminated by a quartz window designed to come in contact  
30 with the sample. The system operates a wavelength of 855 nm and has a coherence length in air of 14  $\mu$ m. Transverse scanning at the sample is achieved by a

multimorph piezoelectric bender, which gives a motion range of 900  $\mu\text{m}$ . A 10  $\mu\text{m}$  sweep in the transverse direction per depth scan was chosen. Signal to noise was measured at 78 dB, with image acquisition times of 5 sec.

#### Example 2 – Instrument Performance

5       The greatest promise of optical coherence tomography is the ability to achieve high-resolution images over a field of view comparable to that observed under a light microscope. The specifications set for the instrument reflect this. These were expressed in terms of depth and transverse resolution, as well as area of coverage. Acquisition time, though not a set design parameter, was minimized. This  
10       characterization allows for a more objective evaluation of the potential of the OCT system with the cervical probe attachment for aiding in the non-invasive morphological characterization of tissue. All of the results presented here were acquired at a line rate of 30 Hz, corresponding to a 1 mm by 1 mm image acquisition time of 3.5 sec. This time is sufficiently short to allow for point measurements  
15       without significant motion artifacts in the cervix.

      The system described herein has been designed to image a variety of biological specimens, including human tissues. In an illustrative embodiment, it has been used in the diagnosis of precancerous lesions in the human cervix. The instrument includes a core OCT system that is capable of acquiring images from a cervical probe  
20       attachment. This probe attachment is capable of acquiring images 1 mm by 1 mm in size, comparable to that of a standard biopsy punch used in the cervix. The system has 22.6 mm depth and 10 mm transverse resolution and is capable of acquiring an image in 3.5 s.

      Results show excellent correspondence between the morphological features  
25       observed in the OCT image and a phase contrast microscope image. An *in vivo* image obtained from the oral cavity mucosa in a human, morphologically similar to the cervical mucosa, showed the system's ability to differentiate the epithelium from the underlying layers. This result is of significance in that cancers in the cervix, as well as in other tissues in the body, are believed to start as an anomaly in the basement  
30       membrane of the epithelium. The possibility to monitor the extent of the epithelial

layer non-invasively may significantly impact a physician's ability to treat the disease at an early stage, not only in the cervix but in other tissues as well.

Resolution in depth is a function of the source used. Currently SLDs are the brightest broadband sources available around 850 nm and thus are the best suited for single mode fiber coupling. Other fiber sources are available at different wavelengths, notably telecommunications-relevant wavelengths of 1.3, 1.5 and 1.8  $\mu\text{m}$  (Bouma *et al.*, 1998). These have also been used in OCT imaging systems that in general trade off resolution for penetration depth (Lankenau *et al.*, 1998). High-speed imaging has also been demonstrated recently using pulse-shaping techniques (Rollins and Izatt, 1998).

### Example 3 -- Subsurface Imaging

Subsurface morphology of tissue is of great importance in the clinical assessment of malignancy. Optical coherence tomography (OCT) methods provide a means for imaging subsurface structure non-invasively with range and resolution believed to be sufficient for successful diagnosis. OCT methods can be divided into two categories by the measuring principle used in generating depth-resolved reflectivity profiles: the first is based on time-domain measurements, and the second on Fourier domain measurements.

In the time-domain method a broad bandwidth source is used to illuminate the sample, which is in one of the arms of a Michelson interferometer. The pathlength of the other arm (the reference arm) is scanned and interference fringes are observed when the optical pathlength of the reference arm is within one coherence length of a reflective site on the sample. Note that the detector in this case is measuring the autocorrelation of the signal from the reference and the sample arms. Many variations of this principle have been studied recently.

In Fourier domain methods an interferometer illuminated with a broad bandwidth source is also used, although the reference and sample arms are stationary. The spectrum of the interferometer output, the interferogram, is analyzed instead. It is the Fourier transform of this interferogram which contains the depth information. The principle is based on spectral interferometry. The signal returning from the sample can be thought of as a superposition of monochromatic waves which interfere with the

similar components reflected from the sample arm. It can be shown (Fercher *et al.*, 1991; Hausler *et al.*, 1998) that the spectrally resolved output of the interferometer carries depth information in the manner analogous to the time domain methods described above. This results from the fact that the power spectral density of a light beam is equal to the Fourier transform of the autocorrelation of the electric field. In a variation of this technique a tunable light source and a single detector can also be used (Haberland *et al.*, 1997; Chinn *et al.*, 1997).

Fourier domain methods provide a means to obtain OCT images in systems without moving parts. Systems which provide single line scans have been reported in the literature (Fercher *et al.*, 1991; Hausler *et al.*, 1998). These however still necessitate some form of transverse scanning of the probe beam in order to assemble a complete image. Another limitation of these systems is the fact that the technique is computationally intensive, since Fourier transforms of each of the acquired spectra must be taken in order to retrieve the depth-resolved reflectance information.

Presented here is a system that may overcome both of these limitations, effectively displaying real-time, two-dimensional OCT images in a system with no moving parts. The system may also have the capability to obtain images endoscopically.

The system is an elaboration of the single line system presented by Hausler and Lindner, and is illustrated in FIG. 30. The single line limitation is overcome by using an imaging system on the sample arm and an imaging spectrograph as a detector. In this way a spectrogram corresponding to a full 2-D OCT image may be collected at once. Note that the transverse (along the surface) resolution in this case is determined by the imaging quality spectrograph while the dispersive quality of the spectrograph and the bandwidth of the source determine the depth resolution. The computational requirements of the Fourier domain methods may be overcome by performing the required Fourier transformations optically.

Apart from being able to obtain 2-D OCT images without moving parts, the proposed system allows for the addition of functional elements, or modules, that may perform other optical measurements *simultaneously*. An example is illustrated in FIG. 30, where a multi-wavelength fluorescence module has been incorporated. The

module may use the same delivery and collection optics as the OCT device but may separate its signal band by the use of a dichroic mirror DM1. This particular setup may allow for the simultaneous measurement of an OCT image together with the spectrally and spatially resolved fluorescence at each point along the surface of the OCT image. In a similar fashion other modules can be incorporated to allow for the visual monitoring of the surface being measured; for the measurement of full field surface fluorescence; and for the delivery of therapeutic optical radiation. All of these can be implemented while monitoring the sub-surface structure with Fourier domain OCT. With the benefit of the present disclosure, those of skill in the art will recognize that numerous other modules may be used in conjunction with the system of FIG. 30, such as, but not limited to, analysis modules and monitoring modules.

#### Example 4 — Laparoscopic Imaging

Recently, office laparoscopic procedures have been developed to visualize the ovaries in a simple outpatient procedure, providing a unique opportunity to design a tool to better evaluate early ovarian disease. Although visual assessment through the laparoscope may identify late ovarian disease, it is not sufficiently sensitive to identify early disease. As described in detail below, the histologic features of the ovary are different than many epithelial organs in which pre-cancers develop. The inventors believe that the combination of spectroscopy and OCT is particularly suited for identifying the molecular and architectural features associated with early ovarian cancers.

During active reproductive life, the ovaries measure approximately 4 cm in length, 2.5-3 cm in width and 1 to 1.5 cm in thickness (Robbins *et al.*, 1984). The ovary consists of an outer cortex and an inner medulla. The cortex is covered by a single layer of surface epithelial cells (~15  $\mu\text{m}$  diameter) atop a thin layer of relatively acellular collagenous connective tissue. By puberty, follicles (~60  $\mu\text{m}$  diameter) and ova (~20  $\mu\text{m}$  diameter) are found in the outer cortex (Robbins, *et al.*, 1995). At puberty, the granulosa cell responds to follicle stimulating hormone and ovulation occurs (Speroff *et al.*, 1994). The follicle ruptures through the surface and the ovarian surface epithelium is left with a large defect.

Ovarian surface epithelial cells proliferate to repair the ovulation defect (Scully, 1995). Epithelial cell proliferation increases the chance that a genetic mistake will occur by increasing DNA replication and the opportunity to induce or express mutations in oncogenes or tumor suppressor genes. Some hypotheses suggest that ovarian inclusion cysts form as the ovarian surface epithelium repairs itself; these involutions are covered with ovarian surface epithelium which can become metaplastic (Scully, 1995). Metaplasia is found much more commonly in the contralateral ovary in patients with ovarian cancer than in patients without cancer, suggesting that this is a precursor lesion to ovarian cancer (Scully, 1995; Mittal *et al.*, 1993; Resta *et al.*, 1993). In all grade 1, most grade 2 and grade 3 epithelial ovarian cancers, cells adjacent to areas of cancer show atypia (Deligdisch *et al.*, 1995; Plaxe *et al.*, 1990). This area has been called ovarian epithelial neoplasia, related to the dysplastic changes in the uterine cervix which are considered to be precursors to cervical cancer. Several ovarian cancer tumor markers, most notably CA125, are found significantly more often in inclusion cysts than in surface epithelial cells (Kabawat *et al.*, 1983). CA125 is a commonly used serum test and is expressed by 80% of advanced malignant ovarian epithelial cancers. Dysplastic papillary excrescences express CA125 as do borderline and invasive cancers. Consequently, areas that express CA125 may exhibit aberrant pathology and other markers of transformation, including expression of Her-2 (30%) and EGFR (77%) (Berchuk, 1995). Thus, in evaluating early ovarian cancer, it is important to assess both architectural features such as inclusion cysts as well as molecular and morphologic features of the ovarian surface epithelium.

Processes which interrupt ovulation (pregnancy, lactation, oral contraceptive pills (OCP)) all decrease the risk of ovarian cancer. The use of OCP for five years reduces the risk of ovarian cancer by 50%, with only a 15% reduction in total number of ovulatory cycles, suggesting that other mechanisms also contribute. One hypothesis is that the decrease in risk is due to both a reduction in ovulation and an increase in apoptosis, or programmed cell death (Wyllie, 1997).

The introduction of comprehensive cervical cancer screening programs based on the Pap smear has dramatically reduced the incidence of cervical cancer in the



United States. Unlike the cervix, which is easily accessible to diagnostic tools such as the colposcope, the ovary is remote and, up to now, has been poorly accessible to noninvasive optical diagnostic techniques. However, based on an increasing body of scientific and medical evidence the inventors reasoned that there are identifiable and easily diagnosable preinvasive areas in women destined to develop ovarian cancer. These areas should have differences in gross architecture (cyst formation), cellular morphology (dysplasia with increased nuclear size and altered chromatin texture), apoptosis (blebbing, chromatin degeneration, apoptotic bodies), cell surface markers (CA125 and others) compared to normal ovary. The combination of OCT and spectroscopy provides unique advantages to aid in the early detection of these features. The molecular specificity of spectroscopy provides a tool to detect functional changes such as increased metabolic rate and, with the addition of fluorophore linked antibodies for cell surface antigens expressed in early cancer, the molecular specificity is further increased. The subsurface resolution of OCT provides a tool to evaluate morphologic and architectural changes such as the increased backscattering associated with apoptosis and dysplasia, as well as the presence of subsurface inclusion cysts. Ovarian cancer is an important disease with a potentially recognizable precursor.

The heterodyne optical detection scheme inherent to OCT provides sensitivity to backscattered signals as small as one part in  $10^{11}$  of the incident optical power, thus extremely faint reflections can be visualized. In OCT, the specimen to be interrogated is placed in the sample arm of an interferometer illuminated with a low-coherence light source. Interference between light returning from the reference arm and light scattered from internal sample reflections occurs only when the interferometer arm optical path lengths are matched to within the source coherence length. Thus, scanning the reference arm while monitoring the envelope of the interferometric signal generates a map of tissue reflectivity versus optical depth or "A-scan," with axial resolution given by the coherence length. Cross-sectional images of tissue backscatter are built from sequential A-scans obtained while scanning the probe beam across the tissue surface. Resulting two-dimensional datasets are plotted as gray-scale images. The imaging point-spread function of OCT in the axial direction is given by

the envelope of the temporal autocorrelation function of the source electric field, whose width is the source coherence length. Superluminescent diodes and semiconductor optical amplifiers which are typically used as sources for OCT feature autocorrelation functions which are very close to a Gaussian as a function of depth, and coherence lengths as short as 10  $\mu\text{m}$ . Thus, reflections more than a few tens of microns away from the peak of the point-spread-function are very strongly rejected, much more strongly than out-of-focus reflections in a confocal microscope. This strong rejection of unwanted light allows for coherence-domain imaging up to several millimeters deep even in highly scattering tissues. OCT imaging depth in scattering tissues is ultimately limited by multiple scattering artifacts which gradually reduce image resolution and contrast, particularly at high NA.

The initial clinical application of OCT was for high-resolution imaging of intraocular structure. A growing number of studies of OCT imaging in non-transparent media have also been reported. *In vitro* and *in vivo* studies have reported OCT imaging in the skin, teeth, and brain, as well as in vascular, respiratory, and gastrointestinal tissues. Recent technical advances in image acquisition time and probe miniaturization have produced the first studies on catheter and endoscopic OCT imaging in living animals and humans. Using a catheter approximately 1 mm in diameter, Sergeev and colleagues recently reported *in vivo* images of human esophagus, larynx, stomach, urinary bladder, and uterine cervix (Sergeev *et al.*, 1997). Epithelial invasion of the basement membrane was visible, implying that the technique is extremely promising for early diagnosis of tumors.

Although OCT provides images with near histological resolution, little is understood about the cellular and extracellular features which give rise to contrast. Signal in OCT images is produced by single backscattering which arises from spatial inhomogeneities in the tissue index of refraction. Analytical methods such as Mie Theory (Van de Hulst, 1957) have been used to describe the scattering of simple structures such as spheres of uniform refractive index. Mie theory and its approximations have been used to provide some insight into the dimension of scatterers likely to contribute to optical images. Mourant has argued that single backscattering is produced primarily by cellular structures small compared to the

illuminating wavelength (Mourant *et al.*, 1996); Feld postulates that the single scattering from cell nuclei modulate epithelial tissue reflectance (Perelman *et al.*, 1998). However, the refractive index profile of cells, which contain water, proteins, nucleic acids and lipids in complex spatial arrangements, are much more complicated than that of a homogeneous sphere. Similarly, the refractive index profile of the structural protein fibers have a complicated spatial pattern. To adequately describe the scattering of cells and extracellular constituents requires a model which can realistically incorporate these structures.

To address these limitations, the inventors have developed a forward scattering model which directly predicts the scattered electromagnetic fields from complex, three dimensional biological objects. In this model, Maxwell's equations are used to describe the propagation of an incident electromagnetic wave through a single cell of arbitrary shape, containing an arbitrary number of irregular inclusions with spatially varying dielectric properties using the finite difference time domain (FDTD) algorithm (Dunn and Richards-Kortum, 1996). A parallel form of Yee's FDTD technique (Weedon *et al.*, 1994) was implemented in 3 dimensions, using the boundary condition of Mur (1981) to calculate the scattered electromagnetic fields for a variety of irradiation conditions, including arbitrary polarizations of plane waves incident directly on the cell or focused on the cell *via* high NA optics. Using this tool, the scattering cross sections and phase functions of cells of varying composition were computed to determine which components contribute most to the backscattering (Dunn and Richards-Kortum, 1996). FIG. 24 shows the scattering phase function for three cells with varying organelle content; cellular scattering increases with the volume of cytoplasmic organelles from 40 to 180° with respect to the incident beam. Similar simulations show that scatter increases with increasing nuclear diameter, although over a smaller range of angles, from 120-180°.

Based on this work, the inventors reasoned that changes associated with neoplasia, in particular increased nuclear size will produce an increase in the backscattering detected by OCT. Thus, morphologic information directly related to the development of neoplasia should be detectable.

### Example 5 – Spectroscopic Diagnosis of Disease

While coherence-domain techniques developed to date rely upon variations in tissue backscattering for image contrast, optical spectroscopic techniques are sensitive to extremely small differences in chemical composition (Richards-Kortum and Sevick-Muraca, 1996). Optical spectroscopy has a rich history of use in the identification and monitoring of physical, chemical, and biological processes. Reflectance (Perelman *et al.*, 1998; Mourant *et al.*, 1995; Bigio *et al.*, 1994; Bigio *et al.*, 1995), fluorescence (Alfano *et al.*, 1987; Cothren *et al.*, 1990; Cothren *et al.*, 1995; Lam *et al.*, 1993; Svanberg *et al.*, 1995; Vo-Dinh, 1995) and Raman (Alfano *et al.*, 1991; Baraga *et al.*, 1992; McCreery *et al.*, 1995) spectroscopy have recently been explored as diagnostic tools in medicine for remote *in situ* identification of disease. In the UV and visible regions of the spectrum, tissue reflectance spectra provide information about the wavelength dependent scattering of tissue as well as electronic absorption bands, primarily those of oxy- and deoxy hemoglobin. Similarly, fluorescence spectra provide information about electronic transitions. The most common naturally occurring biological fluorophores include the aromatic amino acids, the co-factors NAD(P)H and FAD, which describe the tissue metabolic rate, crosslinks associated with collagen and elastin, and porphyrins. The excitation light and fluorescent light undergo scattering and absorption in turbid tissues; thus, fluorescence spectra are also sensitive to changes in scattering and the presence of hemoglobin.

Reflectance and fluorescence spectra of complex, inhomogeneous tissues can be recorded in near real time non-invasively using fiber optic probes designed to be inserted through standard endoscopic equipment. FIG. 25 shows a block diagram of a system that may be used to acquire reflectance and fluorescence spectra of tissue. The system includes of a broad band arc lamp and monochromator to provide a tunable source of monochromatic excitation. A fiber probe directs excitation light to the tissue and delivers the resulting reflected and fluorescent light to a spectrograph and multichannel detector which records the signal intensity as a function of wavelength. Typically, reflectance and fluorescence spectra must be collected sequentially since the dynamic range of the detector is not sufficient to acquire both simultaneously.

During acquisition of fluorescence, long pass filters may be used to block light reflected at the excitation wavelength. Tissue reflectance and fluorescence spectra may be interpreted to give information about the chemical and physical structure of tissues and the likelihood of the presence of disease. A continuing difficulty in clinical application of these techniques for tissue characterization is the difficulty of deconvolving the spectral contributions of scatterers, absorbers and fluorophores; this is particularly challenging in inhomogeneous tissues, where the subsurface structure and chromophore distribution is not known a priori (Durkin *et al.*, 1994; Wu *et al.*, 1993). The combination of OCT and spectroscopy provides a unique approach to this problem.

Members of inventors' laboratory have developed optical techniques to identify pre-malignant and early malignant changes in the female genital tract, including optical techniques to address limitations of the Pap smear and colposcopy, performed when a Pap smear is abnormal. Initially, fluorescence was measured *in vitro* to determine optimal wavelengths for diagnosis (Mahadevan *et al.*, 1993). *In vivo* studies were carried out at 337, 380 and 460 nm excitation (Ramanujam *et al.*, 1996a). A statistical method of algorithm development was designed to extract diagnostically relevant information (Ramanujam *et al.*, 1996b; Tumer *et al.*, 1998). The performance of this algorithm exceeds that of the Pap smear and is comparable to that of colposcopy in expert hands. Because fluorescence spectra may be recorded in real time without tissue removal and data analysis can be automated, optical diagnosis affords many advantages. These include the potential to reduce the need for clinical expertise, reduce the number of unnecessary biopsies and to significantly reduce health care costs (Cantor *et al.*, 1998).

Based on the success of this work, the use of reflectance and fluorescence spectroscopy for the detection of early ovarian cancer has been explored. In a clinical study of patients undergoing laparotomy, fluorescence emission spectra were measured at 18 excitation wavelengths spanning the UV and visible and reflectance spectra were measured from 350 nm to 800 nm; following spectroscopic measurements all sites were biopsied, stained sections were evaluated by a pathologist and photographed. Reflectance spectra indicate differences in the scattering

coefficient and the ratio of oxy-hemoglobin to deoxy-hemoglobin. Fluorescence spectra show contributions consistent with emission of the structural protein crosslinks as well as NAD(P)H and FAD. An analysis correlating spectroscopic measurements with histopathology indicates that spectra are influenced strongly both  
5 by biochemical changes (oxygen saturation and metabolic rate) as well as structural changes (presence of cysts). Members of inventors' laboratory have found the influence of cysts to be so significant that in order to facilitate data interpretation, are being quantitating structural information available from histologic photographs. The advantage of combined OCT and spectroscopy is that this information would be  
10 available non-invasively from OCT images and could be used to aid in the analysis of spectroscopic signals.

The spectral signatures of intrinsic tissue chromophores provide another type of contrast which can be utilized diagnostically to complement the structural information available in OCT images. However, the presence of markers expressed  
15 preferentially in neoplastic ovary provides the opportunity to enhance this contrast with appropriately labeled extrinsic chromophores. Antibodies to CA125 are readily available and can easily be linked to fluorophores. As an example, members of inventors' laboratory have successfully linked OC125 (the antibody to CA125) to the TRICT fluorophore. Ovaries were painted with a solution containing the fluorophore  
20 labeled OC125 and washed after 30 min. Using a 35 mm camera and a long pass filter, the inventors photographed the resulting fluorescence (FIG. 26). Markers indicative of apoptosis can also be similarly targeted. Phosphatidyl serine is translocated from the inner plasma membrane to the outer plasma membrane early in apoptosis. Annexin-V has a high binding affinity for phosphatidyl serine and is easily  
25 linked to a fluorophore (Boersma *et al.*, 1996; Vermes *et al.*, 1995). This may prove to be an accurate method of assessing apoptosis and therefore be a marker for intrinsic activity on the ovarian surface.

#### **Example 6 -- Model Biological Systems for Imaging Studies**

The ideal model system to validate novel advances in high-resolution  
30 combined optical imaging and spectroscopy would mimic both the physical and chemical structure of ovary at the cellular scale in a way that can be manipulated

through the stages of cancer development. Conventional cell cultures provide homogeneous samples which can be used to study changes in normal and transformed epithelial cells. However, these cultures do not reflect the complex physical organization of the epithelium and underlying stroma present in real tissues. While  
5 intact tissues obviously exhibit the desired morphologic characteristics, they can be difficult to access and manipulate precisely through various stages of the cancer sequence.

Growing cells as an adherent monolayer in plastic dishes or in suspension culture is technically straightforward. Therefore, it is the major method that cell  
10 biologists use to study animal and human normal and malignant cells *in vitro* (Fogh, 1975), and is the first biological model the inventors use to validate the experimental techniques disclosed herein. However, the maintenance of various tissue components in their normal anatomical relationship is important for regulation of growth and differentiation (Miller *et al.*, 1989; Hoffman, 1991). Tumor cells, stromal fibroblasts,  
15 and endothelial cells may express a set of genes *in situ* that only partially overlaps the set expressed by each cell type in isolation from the other in primary cultures. In addition, the mesenchymal cells may secrete factors that the tumor cells can use as mitogens. Organotypic cultures have been developed initially for skin and then adapted for a variety of epithelial cancers as an approach to provide the three  
20 dimensional growth including epithelial cell-cell interactions that are major features of solid carcinomas, but are partially lost in monolayer cultures. The method is based on the growth of epithelial cells at the air-liquid interface on top of a collagen gel containing fibroblasts (hence the name RAFT cultures for floating on the liquid phase). This organ culture provides conditions that preserve tissue architecture,  
25 growth, and function. It can be prepared with different cell layers and can be analyzed as a tissue without restrictions involved in obtaining actual surgical specimens from patients or volunteers. RAFT cultures are also more reproducible than tissues obtained from different individuals. Members of inventors' laboratory believe that preclinical research would greatly benefit from analysis of novel diagnostic  
30 approaches directly in organotypic cultures because the results are likely to be more informative and could be extrapolated to the *in vivo* situation with greater confidence

than work with cell lines in monolayer cultures. Utilization of these complex cultures will represent a test of the disclosed methods and apparatus.

An understanding of the native sources of signal and contrast in OCT images permits the rational design of physical methods to enhance this contrast. Members of  
5 inventors' laboratory may consider two methods of contrast enhancement: (A) addition of contrast agents which affect the backscattering of normal and neoplastic cells differently, and (B) selection of wavelengths where the backscattering and/or absorption of normal and neoplastic cells differ most.

Intrinsic differences in the index of refraction profile give rise to contrast in  
10 OCT images of normal and neoplastic ovarian cells. Several methods to differentially alter the index profiles of normal and neoplastic ovarian cells in order to enhance this contrast may be explored. A contrast agent routinely used in the colposcopic detection of cervical pre-cancer-acetic acid may be examined. During colposcopy, 3% acetic acid is applied to the cervix; areas which turn white are most likely to harbor  
15 pre-cancerous cells. While a number of hypotheses to explain acetowhitening have been advanced, it appears that a selective enhancement of nuclear scattering in pre-cancerous cells and an increased permeability of neoplastic epithelium to acetic acid play a role. Members of inventors' laboratory examined phase contrast images of neoplastic epithelial cells before and after exposure to acetic acid (FIG. 27) and  
20 observed an increase in the spatial fluctuations in the nuclear index of refraction. FIG. 28 shows the measured scattering phase function of neoplastic ovarian cells before and after addition of acetic acid. Clearly, acetic acid increases the backscattering. The ability of acetic acid to selectively induce increased backscattering in neoplastic ovarian cells as detected with OCT in cell cultures, organ  
25 cultures and *in vivo* may be examined.

Contrast agents linked to markers associated with ovarian cancer which increase the local index of refraction may also be examined. Liposomes are membrane bound spherical structures which can be linked to antibodies to cell surface antigens (Goins, 1997). Liposome based systems to selectively increase the  
30 backscattering of neoplastic ovarian cells and test the ability of such systems to produce contrast in OCT images may be designed. Given the density of cell surface



antigens, the expected binding efficiency, and the size and index of fluid within the liposome, the inventors' forward model can be used to predict the expected increase in backscattering. It is expected that liposomes which are small compared to the illumination wavelength and which contain a high index fluid will produce the greatest increase in backscattering. To demonstrate the potential of this technique, members of inventors' laboratory attached 250 nm diameter liposomes filled with water to 18  $\mu$ m diameter polystyrene microspheres. Scattering phase functions were measured before and after attachment of liposomes; liposomes produced an increase in backscattering. More significant increases should be possible by increasing the index of the fluid within the liposomes (by adding bovine serum albumin (BSA) this index can be increased up to 1.43 for example). Simulations and studies may be conducted to determine the ideal size, index and marker for liposomes enhanced contrast in OCT, beginning with polystyrene spheres, moving to cells suspensions, then RAFT cultures and finally *in vitro* ovarian tissue. Markers that will be targeted include CA125 ( $10^6$ /cancer cell,  $10^0$ /normal cell), EGFR ( $10^{4-5}$ /cancer cell,  $10^4$ /normal cell) and Her-2 ( $10^{4-6}$ /cancer cell,  $10^4$ /normal cell).

It is believed that increased backscattering may also potentially be achieved by adding strongly absorbing extrinsic dyes which accumulate selectively in neoplastic ovarian cells. The absorption coefficient ( $\alpha$ ) is directly related to the imaginary part of the refractive index ( $k$ ) :  $\alpha = (4\pi k)/\lambda$  where  $\lambda$  is the wavelength (Foster, 1992). Thus, an increase in local absorption coefficient also leads to an increase in refractive index and potentially backscattering. This approach to increased backscattering is designed to mimic the backscattering of melanin. The intrinsic absorber melanin is present in melanosomes which are small compared to the incident wavelength. Melanin granules produce very strong backscattering which can clearly be observed in OCT and confocal images of skin (Rajadhyaksha *et al.*, 1995; Sergeev *et al.*, 1996). Although melanin is strongly absorbing, because it is present in such small packages, the total absorption cross section is low, and images can be obtained deep within melanotic tissues by taking advantage of this backscattering. The Kramers Kronig integral provides a direct relationship between the wavelength dependent real and imaginary parts of the refractive index and can be used to predict how much of an

increase in local absorption is required to produce a significant change in the refractive index (Hodgson, 1970). Calculations show that for a 10 nm wide absorption band, a local absorption coefficient of  $10^4 \text{ cm}^{-1}$  is required to produce an increase of 0.05 in refractive index. Although most biological absorbers do not produce such high absorption in tissue (melanin is an exception), there are many extrinsic dyes (such as phycoerythrin) with extinction coefficients exceeding  $10^6 \text{ cm}^{-1} \text{ M}^{-1}$  so that the needed absorption could be achieved at local dye concentrations of several hundred  $\mu\text{M}$  (Murphy and Lagarias, 1997). Absorbing dyes which localize in membranes so that structures small compared to the wavelength such as mitochondria will accumulate the absorber and produce backscattering may be pursued. This approach in cell cultures, RAFT cultures and finally *in vitro* ovarian tissue may be tested. The increase in local absorption may be measured using an absorption microspectrophotometer. The Kramers Kronig integral may be used to compute the increase in the refractive index and use the inventors' model to predict the cell phase function. Phase function measurements may be compared to predictions. The increase in OCT image contrast may be assessed in each tissue model.

The technique of wavelength-ratiometric OCT (WROCT) can be used to image physiological analyte concentrations as well as extrinsic chromophore concentrations based on the differential absorption of OCT probe light at two or more separate illumination wavelengths. The intensity of the signal of wavelength  $\lambda$  backscattered from a depth  $x$  in a homogenous medium can be expressed as:

$$S(\lambda, x) = B(x)I(\lambda, 0)e^{-2x(\mu_a(\lambda) + \mu_s(\lambda))},$$

where  $B(x)$  is the backscatter profile of the sample,  $I(\lambda, 0)$  is the incident intensity, and  $\mu_a(\lambda)$  and  $\mu_s(\lambda)$  are the absorption and scattering coefficients. These two wavelengths are ideally chosen such that the scattering coefficients are equal, while the analyte absorption coefficients are as different as possible. Under these assumptions, using incident beams of equal intensity, the natural log of the ratio of the signals at two wavelengths is:

$$\ln\left(\frac{S(\lambda_1, x)}{S(\lambda_2, x)}\right) = 2xC(\sigma_a(\lambda_2) - \sigma_a(\lambda_1))$$

where  $C$  is the absorber concentration and  $\sigma_a(\lambda)$  is the absorption cross section. Light from both sources may be coupled into the OCT interferometer simultaneously by using a standard wavelength-division multiplexer. Then, the wavelength-resolved images are separated by demodulating the detected interferometric signal from the scanning reference mirror at the different Doppler shift frequencies corresponding to the different wavelengths. This technique for simultaneous dual-wavelength OCT has been demonstrated previously (Gelikonov *et al.*, 1997).

The use of WROCT to produce high contrast images of ovarian cancer using the absorption of extrinsic chromophores may be explored. The absorption differences produced by extrinsic chromophores linked to antibodies for markers associated with ovarian cancer may be used. Here, only relatively small changes in the absorption coefficient - less than  $1 \text{ cm}^{-1}$  need to be produced. Dyes developed for photodynamic therapy with NIR illumination present an ideal choice for this approach, since they absorb in the NIR and accumulate preferentially in neoplastic tissues. The inventors will examine a variety of these dyes, beginning with indocyanine green (FDA Approved) (Sevick-Muraca *et al.*, 1997) and lutetium texaphyrin (Young *et al.*, 1996), first in cell cultures to determine the expected differential absorption, then in RAFT cultures and finally in *in vitro* ovary. With both dyes, preferential accumulation leading to a tenfold increase in drug concentration has been reported in tumors, resulting in increased absorption at 740 (texaphyrin) and 760 nm (ICG) (Sevick-Muraca *et al.*, 1997; Young *et al.*, 1996).

In mapping absorption using WROCT, two illumination wavelengths may be selected where the scattering cross section is similar. If, instead, two wavelengths are chosen where the scattering of a particular structure is different, but the absorption is similar, WROCT images may enhance the contrast associated with that structure. Thus, the wavelength dependence of backscattering may be exploited to enhance contrast in OCT images. The forward model may be used to describe cell scattering as a function of wavelength. FIG. 29 shows an example of the scattering phase function for an ovarian epithelial cell at different illumination wavelengths. As the wavelength is increased, the backscattering increases, because the number of structures in the cell small compared to the incident wavelength increases. The

forward model may be used to predict whether the wavelength dependence of backscattering differs significantly for normal and neoplastic ovarian cells and if so, to predict which wavelengths are optimal to recognize ovarian cancer cells. The technological development of WROCT may then be taken advantage of to add  
5 differential wavelength contrast to images of anatomic microstructure. This method may be tested in cell cultures, RAFT cultures, *in vitro* ovary and *in vivo*.

Integration of spectroscopic information provides another dimension to increase contrast. Building on recent advances using Fourier-domain reconstruction of OCT ranging data ("spectral radar") (Hausler and Lindner, 1998), a simple fiber  
10 optic probe may be developed which has no moving parts to simultaneously record the spectrum of fluorescent light emitted from the surface of a tissue site and to record the subsurface structure with high spatial resolution using OCT. In Fourier domain methods, an interferometer illuminated with a broad bandwidth source may be used, although the reference and sample arms are stationary. The spectrum of the  
15 interferometer output, the interferogram, may be analyzed instead. It is the Fourier transform of this interferogram that contains the depth information. The signal returning from the sample may be thought of as a superposition of monochromatic waves which interfere with the similar components reflected from the sample arm. It can be shown (Hausler and Lindner, 1998; Fercher *et al.*, 1991) that the spectrally  
20 resolved output of the interferometer carries depth information in the manner analogous to the time domain methods. This results from the fact that according to the Weiner-Khinchine theorem, the power spectral density of a light beam is equal to the Fourier transform of the autocorrelation of the electric field. In a variation of this technique a tunable light source and a single detector can also be used (Chinn *et al.*,  
25 1997; Haberland, 1997).

Fourier domain methods provide a means to obtain OCT images in systems without moving parts. Systems which provide single line scans have been reported (Hausler and Lindner, 1998; Fercher *et al.*, 1988). These however still necessitate some form of transverse scanning of the probe beam in order to assemble a complete  
30 image. Another limitation of these systems is the fact that the technique is computationally intensive, since Fourier transforms of each of the acquired spectra

must be taken in order to retrieve the depth-resolved reflectance information. A system in accordance with the present disclosure that overcomes both of these limitations, effectively displaying real-time, two or three-dimensional OCT images (by using a one or two dimensional fiber optic bundle, respectively) in a system with  
5 no moving parts is illustrated in FIG. 30. The system has the capability to obtain images endoscopically. The system is an elaboration of the single line system presented by Hausler and Lindner. The single line limitation is overcome by using a coherent single mode fiber bundle and an imaging system on the sample arm and an imaging spectrograph as a detector. In this way a spectrogram corresponding to a full  
10 2 or 3-D OCT image may be collected at once. Note that the transverse (along the surface) resolution in this case is determined by the fiber size and bundle spacing and the imaging quality spectrograph while the dispersive quality of the spectrograph and the source bandwidth determine the depth resolution.

The computational requirements of the Fourier domain methods may be  
15 overcome, in one embodiment, by performing the required Fourier transformations optically. In this novel scheme, a cylindrical lens placed a focal length away from the output slit of the imaging spectrograph will calculate an exact Fourier transform of the dispersed optical frequency spectrum, thus reproducing the reflectance depth profile of the sample on an array detector in the lens back focal plane. The DC component of  
20 the spectrum will be mechanically blocked, thus overcoming the primary limitation upon dynamic range in previous array-detection OCT schemes proposed to date. For illumination sources with small relative bandwidth as are commonly used in OCT, the absolute variation in optical frequency across the dispersed spectrum will be small and is not expected to degrade the optical Fourier transform significantly. For larger  
25 relative bandwidth sources, a variation of the phase-control optical delay line used in Izatt's laboratory for video-rate OCT may be adapted for frequency-specific pre-filtering of the dispersed spectrum prior to Fourier transformation.

Alternatively, recent advances in application-specific integrated circuit (ASIC) and field programmable gate array (FPGA) technologies specifically designed for  
30 high-speed FFT calculations may provide cost-effective solutions for real-time spectral OCT imaging. At least one laboratory has worked with a developer of PC-

compatible FPGA solutions to design a card for real-time CDOCT imaging that is capable of performing  $10^6$  32-element complex FFTs per sec, or equivalently more than 50,000 512-element real FFTs per sec. Such a card may easily be adapted to perform spectral OCT up to and beyond video rate.

5        Apart from being able to obtain 2 or 3-D OCT images without moving parts, the system of FIG. 30 allows for the addition of functional elements, or modules that may perform other measurements, including, for instance optical measurements, simultaneously. An example is illustrated in FIG. 30, where a multi-wavelength fluorescence module has been incorporated. The module uses the same delivery and  
10       collection optics as the OCT device but separates its signal band by the use of a dichroic mirror DM1. This setup allows for simultaneous measurement of an OCT image together with the spectrally and spatially resolved fluorescence at each point along the surface of the OCT image. In a similar fashion other modules may be incorporated to allow for, the example, the visual monitoring of the surface being  
15       measured; measurement of full field surface fluorescence; and for delivery of therapeutic optical radiation. All of these can be implemented while monitoring the sub-surface structure with Fourier domain OCT. With the benefit of the present disclosure, those having skill in the art will appreciate that many other modules may also be utilized in combination with embodiments described herein, including the  
20       embodiment of FIG. 30.

      The excitation wavelengths for this system based on an analysis of a study that measured fluorescence emission spectra of normal and neoplastic ovary at 18 excitation wavelengths. The inventors may test the combined OCT/fluorescence system using RAFT cultures and *in vitro* ovary samples. The fluorescence of intrinsic  
25       chromophores may be examined initially. If necessary, the additional contrast provided by extrinsic fluorophores may be examined. The inventors may link fluorophores to antibodies to CA125 receptors, EGFR receptors and Her-2 receptors. TRICT may be used as a fluorophore because of its high quantum yield and red excitation which allows deep penetration.

30       New technologies and methods of analysis developed herein may be used to characterize samples ranging from single cells and cell suspensions, to complex multi-

layer cell cultures. In addition, surgically removed ovaries may be examined *in vitro*. The use of absorbing, scattering and fluorescent contrast agents linked to specific cell surface antigens expressed on neoplastic epithelial cells may be explored.

OC125, antibody to CA125, has been linked to fluorophore in at least one  
5 laboratory. This can either be added to cell culture or painted on the ovary and may be a marker for expression of CA125. Probes may be used to study the properties of normal ovarian cells, transformed cells and ovarian cancer cells grown in monolayer. OC125 linked to a fluorophore may be used to determine the amount of CA125  
10 expression in this population. Normal ovarian surface epithelium lacks CA125 expression along with SV40 T antigen immortalized epithelial cells. Transfected cells which are known to express CA125 may be used as controls for the CA125 linked antibody. An *in vivo* marker for CA125 may well indicate that microscopic pathology exists and the inventors may use this opportunity to investigate if this may be one  
15 mechanism for screening high risk patients. Anti-Her-2 (TA1 antibody) antibody and anti-EGFR antibody (225 antibody) may also be explored to develop other markers for underlying pathology. Annexin-V linked to fluorophore may be used to assess apoptosis.

#### **Example 7 – OCT System for Early Detection of Ovarian Neoplasias**

This example describes a rapid scan OCT system to image ovarian tissue *in*  
20 *vivo* at the time of laparotomy. A fiber optic-based probe to acquire OCT images of the exocervix *in vivo* has been designed and tested to image ovarian tissue *in vitro* (see FIGS. 15-23). The probe is approximately 2 cm in diameter, and can be advanced to the ovary through the abdominal incision made at laparotomy. The probe features a GRIN lens to focus the light into the sample and a multimorph piezoelectric  
25 translator to scan the fiber and lens assembly transversely. This results in a transverse coverage of 900  $\mu\text{m}$  (piezoelectric translator specification) with 10  $\mu\text{m}$  resolution. The ovarian OCT system features a depth (ranging) resolution of 10  $\mu\text{m}$  in tissue, and can acquire cross-sectional images with dimensions  $0.9 \times 1 \text{ mm}$  (transverse  $\times$  depth) in 3 sec with 75 dB dynamic range, or in 20 sec with >100 dB dynamic range.  
30 FIG. 41 shows an image of a normal ovary and an ovarian cyst acquired *in vitro* with this system.

### **Example 8 -- Spatially Resolved Spectral Interferometry for Determination of Sub-Surface Structure**

The following is an example of an instrument capable of obtaining 2-dimensional images of sub-surface structure in real time with no moving parts. The technique is based on spectral interferometry and uses an imaging spectrograph to obtain spatially resolved spectra. A test sample consisting of microscope cover slips and a Ronchi grating was measured, illustrating the system's depth resolution of 38  $\mu\text{m}$  and transverse resolution of at least 12.7  $\mu\text{m}$ . The technique is readily adaptable to endoscopic delivery as well as 3-dimensional, real time image acquisition.

Many fields require high resolution, sub-surface imaging. Applications include characterization of semiconductors and non-invasive tumor detection for medical screening. Optical coherence tomography (OCT) is a promising technique to address these tasks, providing micron-scale resolution in a variety of media. OCT systems presented for the collection of 2 and 3-dimensional data sets require high-speed scanning components for rapid image acquisition. For remote delivery and collection of the signal, a very desirable quality in medical applications, problems arise due to the need for miniaturized mechanical scanning components. While some groups have successfully addressed these problems, a system that could acquire 2 and 3-dimensional images with no moving parts would have important advantages. In this example, the inventors present a variation of OCT that allows the acquisition of 2 and 3-dimensional images of subsurface structure with no moving parts and has the potential to acquire images in real time. The technique is also readily adaptable to endoscopic implementation.

The traditional implementation of OCT is essentially a time-domain technique. In this traditional method, a broad bandwidth source is used to illuminate the sample, which is in one of the arms of a Michelson interferometer. The pathlength of the other arm (the reference arm) is varied and interference fringes are observed when the optical pathlength of the reference arm is within one coherence length of a reflective site within the sample. Note that the detector in this case measures the cross correlation of the signals from the reference and the sample arms. A method for providing a continuous optical delay in the reference arm without mechanical



scanning was presented recently. This is achieved by using a reflective grating in the Littrow configuration in the reference arm. The output plane of the interferometer then encodes depth along the dimension of the grating-induced path delay (making it a parallel, time-domain technique), and can encode a lateral dimension simultaneously.

5 In an alternative approach a stationary interferometer illuminated with a broad bandwidth source is also used and the spectrum of the interferometer output, the interferogram, is measured instead. The Fourier transform of the interferogram contains the depth information. This can be thought of as a frequency domain technique. The signal returning from the sample is a superposition of monochromatic  
10 waves that interfere with the similar components reflected from the sample arm. This results in fringes at the output plane of the spectrograph. Depth information is encoded as the spatial frequency of the fringes and is given by

$$\Delta\sigma = \frac{1}{2 \cdot \Delta z}$$

15

Where  $\sigma = 1/\lambda$  is the wavenumber and  $\Delta z$  is the difference in distance from the reference mirror to the site in the sample that generated those fringes. This results in

$$\Delta z = \frac{1}{2} \cdot \frac{\lambda^2}{\Delta\lambda}$$

20

Where  $1/\Delta\lambda$  is the frequency of the observed fringes at the spectrograph output plane and  $\lambda$  corresponds to the center wavelength of the source.  $1/\Delta\lambda$  is readily obtained by Fourier transformation of the output spectrum, even in the case of complex multi-component signals. More detailed explanations have been presented  
25 by Fercher and Hausler.

Spectral interferometry provides a technique to probe subsurface structure beneath a single point using a system with no moving parts. In this example, an extension of this technique is presented in which 2-dimensional images of the subsurface structure beneath a line are obtained in a system with no moving parts.  
30 This is accomplished by optically imaging a line on the sample surface in the sample

arm of the interferometer onto the entrance slit of an imaging spectrograph coupled to an array detector. This is illustrated in FIG. 55. At the output of the spectrograph, the wavelength information encodes the depth (z) resolved remittance of the sample while the spatial direction (x) encodes the imaged, transverse direction on the sample. Line  
5 by line Fourier transformation along the wavelength direction converts the information back to the spatial domain. This allows for the acquisition of 2-dimensional images with no moving parts.

A study was designed to demonstrate this technique. An EG and G superluminescent diode source was collimated to a diameter of 5 mm and used as the  
10 input to a Michelson interferometer. The source had an output power of 500  $\mu$ W, a center wavelength of 855 nm and a FWHM bandwidth of 25 nm. Light was focused to a 500  $\mu$ m spot on the sample with a 155 mm focal length lens. An identical lens focused the light onto a flat, variable reflectance mirror in the reference arm. The optical path length in the sample arm was 1 mm longer than in the reference arm.  
15 After image reconstruction (line-by-line Fourier transformation of the spectrograph output image) this shifted the desired signal, consisting of cross-correlation of reference arm and signal remitted from sample, away from confounding terms. Confounding terms arise from source autocorrelation as well as autocorrelation terms between signals remitted from within the sample. These confounding terms occur  
20 around zero depth in the reconstructed image. The collimated signal returning from the reference and sample arms was then input into a Chromex 500 IS imaging spectrograph coupled to a Sony XC-75 camera. A cylindrical lens of focal length 40 mm was used to focus the interferometer output at the spectrograph input slit, which was set to a width of 25  $\mu$ m. Images were digitized to 8 bits at 30 frames per sec  
25 using a Matrox video capture card and saved to disk where Fourier transformation was implemented in software. The setup provided a theoretical depth resolution of 38.1  $\mu$ m with a maximum depth of 13.5 mm in air. These were limited by the detected bandwidth (in this case limited by the detector size) and pixel element size respectively. The imaging spectrograph is capable of independently resolving at its  
30 output plane the spectra from two spots imaged on its input slit when they are separated by 40  $\mu$ m. The input slit height is 10 mm although the detector height is 4.8

mm. The resolution achieved along the sample surface was limited by the imaging resolution of the spectrograph ( $40\text{ }\mu\text{m}$ ) and the magnification ratio of the spot on the sample to the projected image on the spectrograph input slit. The calculated magnification ratio was 10 ( $5\text{ mm}/500\text{ }\mu\text{m}$ ), resulting in a resolution on the sample surface of  $4\text{ }\mu\text{m}$ . The total coverage along the sample surface was limited by the magnification ratio and detector size and was calculated to be  $480\text{ }\mu\text{m}$ . Depth resolution and coverage were determined by the spectrograph's dispersive properties, while the transverse coverage and resolution were determined by the spectrograph's imaging properties. These are independent of one another.

10 A sample consisting of microscope cover slips and a Ronchi grating was used to illustrate the capability of this system. The sample arrangement is shown in FIG. 56. Two stacks of two cover slips each were used to raise another cover slip over a Ronchi grating. The grating had a reflective bar pattern of 500 cycles per inch. It was oriented such that the direction of the bars was perpendicular to the transverse  
15 imaging direction ( $x$ ). This provided a layered sample consisting of two glass layers separated by an air gap. The bars of the grating provided a pattern in the transverse imaging direction on the surface of the bottom glass layer. A single frame of the spectrograph output was captured. A background image, consisting of the spectrograph output with no sample in the interferometer was subtracted. Line-by-line  
20 Fourier transformation along the wavelength direction was then carried out, resulting in a two-dimensional image of the sample, shown in FIG. 57. For display purposes the image was also linearly interpolated 4 times in both horizontal and vertical directions. The structure of the layered sample is clearly seen in FIG. 57. The horizontal axis corresponds to depth in the sample ( $z$ , in FIG. 55), while the vertical axis corresponds to the transverse direction ( $x$ , in FIG. 55). The grayscale value  
25 represents the relative intensity of the reflected signal. The horizontal axis scale is calculated in microns of optical path length relative to the reference mirror. The vertical axis is given in microns and intensity scale is arbitrary but linear. From left to right in the image all four layers are easily distinguished: the top air layer is seen first,  
30 followed by the first glass layer corresponding to the top microscope cover slip; the air gap between the top cover slip and the Ronchi grating is seen next, followed by the

grating itself. Significant background noise is observed. Most is due to the combination of low digitization depth and high frame rate of the camera. Some of the noise is patterned, suggesting that it is due to multiple reflections within the sample, or to the source spectrum satellite peaks. Interference from light backscattered from off-axis points may also contribute to the patterned background noise.

Nine cycles of the 500 cycles per inch (25.4  $\mu\text{m}$  bars) grating are clearly distinguishable on the surface of the grating. This sets the approximate transverse coverage of this system at 460  $\mu\text{m}$ , with a resolution of at least 12.7  $\mu\text{m}$  (compare to the theoretical transverse resolution of 4  $\mu\text{m}$  calculated above). The transverse coverage compares very favorably to the value of 480  $\mu\text{m}$  calculated above. In the depth dimension, a range of about 1.6 mm optical pathlength is shown. Very good agreement is found between the dimensions from FIG. 57 and measured dimensions with a dial caliper. Notably, the depth of the top cover slip is measured to be 244  $\mu\text{m}$  from FIG. 57. Assuming an index of refraction of 1.5, this corresponds to a physical distance of 163  $\mu\text{m}$ . The measured thickness of the cover slip was 165  $\mu\text{m}$ . The depth of the air gap between the top cover slip and the grating is measured as 413  $\mu\text{m}$  from the FIG. 57, 83  $\mu\text{m}$  more than expected assuming equal cover slip thicknesses of 165  $\mu\text{m}$ . This could be due to small air gaps in between the stacked cover slips.

The current system acquires 2-dimensional images with no moving parts at video rate. Available digital signal processing boards may enable real-time processing of the acquired video stream. Optical Fourier transformation of the signal at the output plane of the spectrograph is not possible because the spectral content varies across the imaged field. Improvements in the system's detector may be needed in order to image highly scattering samples. More sensitive CCDs are available with higher bit depths. They may improve the sensitivity and signal to noise ratio. Some reduction in the data acquisition rate may be expected.

The results presented successfully show that it is possible to obtain two-dimensional images of sub-surface structure with tens of microns resolution in a system with no moving parts. This allows for straightforward implementation of remote delivery systems using optical fibers (inset, FIG. 55), an attractive possibility for medical applications. The resolution can be improved by increasing the

wavelength coverage of the spectrograph and using broader-band sources. Real time, 3-dimensional acquisition is also possible. This may be implemented by imaging the sample onto a 2-dimensional fiber bundle array, where the fibers have been arranged in a line at the proximal end and are imaged on to the spectrograph entrance slit (FIG. 55, inset). The spectrum of each fiber would then provide depth information about the point in the 2-dimensional patch imaged onto that fiber. This results in non-scanning, 3-dimensional image acquisition.

### Example 9 -- OCT System

#### Fourier Domain OCT

In a traditional implementation of OCT, a broad bandwidth source is used to illuminate a sample, which is in one of the arms of a Michelson interferometer. The pathlength of the other arm (the reference arm) is scanned and interference fringes are observed when the optical pathlength of the reference arm is within one coherence length of a reflective site on the sample. Note that the detector in this case is measuring the cross-correlation of the signal from the reference and the sample arms.

In Fourier domain methods an interferometer illuminated with a broad bandwidth source is also used, although the reference and sample arms are stationary. The spectrum of the interferometer output, the interferogram, is analyzed instead. It is the Fourier transform of this interferogram which contains the depth information. A schematic representation of the experimental setup is shown in FIG. 58. The principle is based on spectral interferometry. The signal returning from the sample can be thought of as a superposition of monochromatic waves which interfere with the similar components reflected from the sample arm. It can be shown that the spectrally resolved output of the interferometer carries depth information in the manner analogous to the time domain methods described above. This results from the fact that the power spectral density of a light beam is equal to the Fourier transform of the autocorrelation of the electric field. In a variation of this technique a tunable light source and a single detector may also be used.

At the output of the interferometer, the wavenumber-dependent signal can be expressed as

$$I(k) = S(k) \left| a_R \cdot \exp(i2kr) + \int_0^{\infty} a(z) \cdot \exp(i2k[r + n(z) \cdot z]) \cdot dz \right|^2 \quad [2.5]$$

Where  $k=2\pi/\lambda$  [1/m] is the light wavenumber and  $S(k)$  denotes the spectral intensity distribution of the source. The first term in the magnitude brackets corresponds to the reference arm term.  $a_R$  is the amplitude of the reference arm signal and  $2r$  is the round-trip path length in the reference arm. The second term of the expression describes the signal returning from the sample arm.  $a(z)$  is the depth-resolved backscattering amplitude of the object along the illumination axis;  $2[r+z]$  is the round-trip pathlength in the sample arm; and  $n(z)$  is the depth-resolved index of refraction of the object along the illumination axis. Note that no wavelength ( $k$ ) dependence has been assumed for either  $a(z)$  or  $n(z)$ .

$a(z)$  can be obtained by Fourier transformation of  $I(k)$  after symmetric expansion of the integral with respect to 0 and expansion of the terms in the magnitude brackets. Then

$$I(k) = S(k) \left[ 1 + \int_{-\infty}^{\infty} \hat{a}(z) \cdot \cos(2knz) \cdot dz + \frac{1}{4} \int_{-\infty}^{\infty} \int_{-\infty}^{\infty} \hat{a}(z) \cdot \hat{a}(z') \cdot \exp(-i2kn \times [z - z']) \cdot dz \cdot dz' \right] \quad [2.6]$$

Where  $\hat{a}(z)$  denotes the expansion coefficients corresponding to  $a(z)$ . Note that the second term in the square brackets is the Fourier transform of  $\hat{a}(z)$ , and the third term in the square brackets is the autocorrelation (AC) of  $\hat{a}(z)$ . The autocorrelation term encodes the interference from all of the reflections inside the sample with themselves. Inverse-Fourier transformation ( $\mathfrak{F}^{-1}$ ) of  $I(k)$  results in

$$\mathfrak{F}^{-1}\{I(k)\} = \mathfrak{F}^{-1}\{S(k)\} \otimes \left( \delta(z) + \frac{1}{2} \hat{a}(z) + \frac{1}{8} AC[\hat{a}(z)] \right) \quad [2.7]$$

$\otimes$  denotes the convolution operator. After the transformation three terms are observed: the first is the inverse Fourier transform of the source around  $z=0$ ; the second is the convolution of the signal  $\hat{a}(z)$  with the transform of the source spectrum; and the third is the convolution of the source spectrum with the autocorrelation terms, also centered around  $z=0$ . The desired term  $\hat{a}(z)$  can be isolated from the other two terms by placing the reference plane at an offset  $z_0$  from the object surface. This has

the effect of shifting the Fourier-transformed terms away from zero where they would superimpose with the source transform and autocorrelation terms.

Fourier domain methods provide a means to obtain OCT images in systems without moving parts. Systems which provide single line scans have been reported in the literature. These however still necessitate some form of transverse scanning of the probe beam in order to assemble a complete image. Another limitation of these systems is the fact that the technique is computationally intensive, since Fourier transforms of each of the acquired spectra must be taken in order to retrieve the depth-resolved reflectance information.

#### 10 Fourier Domain OCT

In this example, there is presented a system that overcomes the limitations of mechanical scanning and high-bandwidth signal processing while displaying real-time, two-dimensional OCT images. The system may also have the capability to obtain images endoscopically. It is an elaboration of the single line system presented by Häusler and Lindner and is illustrated in FIG. 59. The single line limitation is overcome by using an imaging system on the sample arm and an imaging spectrograph in the detection path. In this way a spectrogram corresponding to a full 2-D OCT image may be collected at once.

Note that the transverse resolution (along the sample surface) in this case is determined by the imaging quality of the spectrograph while the dispersive quality (resolution and coverage) of the spectrograph and the bandwidth of the source determine the depth resolution. The computational requirements of the Fourier domain methods may be overcome by converting the spectrograph output intensity from incoherent to coherent and then performing the required Fourier transformations optically. All-optical incoherent to coherent transformation of a signal may be done by using an optically addressed spatial light modulator (OASLM). Table 1 in Bernasconi et. al. illustrates the variety and characteristics of currently available OASLMs.

Apart from being able to obtain 2-D OCT images without moving parts, the system of this example allows for the addition of functional elements, or modules, that can perform other optical measurements simultaneously. An example is illustrated in

FIG. 59, where a multi-wavelength fluorescence "module" has been incorporated. The module would use the same delivery and collection optics as the OCT device but would separate its signal band by the use of a dichroic mirror DM1. This particular setup would allow for the simultaneous measurement of an OCT image together with the spectrally and spatially resolved fluorescence at each point along the surface of the OCT image. In a similar fashion other "modules" may be incorporated to allow for the visual monitoring of the surface being measured; for the measurement of full field surface fluorescence; and for the delivery of therapeutic optical radiation. All of these may be implemented while monitoring the sub-surface structure with Fourier domain OCT.

#### System Specifications

A system may be built to prove the concept and assess the potential of Fourier Domain OCT for imaging of subsurface biological structures. A system diagram is shown in FIG. 60. Light from a broadband source (SLD) is directed to the sample through a polarizing beamsplitter (PBS) and quarter-wave (QW) plate. A partially reflecting mirror (Mr) is placed a short distance ( $\sim 1$  mm) before the sample (S) and acts as a reference mirror. Light returning from the sample and the reference mirror is expanded 10x and then directed into an imaging spectrograph (Chromex 500 IS, Chromex, Albuquerque, NM). The spectrograph provides at its image plane a map of the dispersed wavelength content of each of the spatial positions on its entrance slit. Since the entrance slit of the spectrograph is at a conjugate plane of the sample, the spectrograph image at plane SP corresponds to the interference of the signal from the reference mirror and the (space-resolved) signal returning from the sample. Note that for each resolvable spatial position the wavelength dependence on this plane is given by Equation 2.5. An image may be obtained here and then Fourier-transformed numerically (cfr. Equation 2.7) to yield the desired information.

Alternatively, the Fourier transformation property of lenses may be exploited to achieve the same result. This would require the introduction of an OASLM as an intermediate detector and a coherent "readout" source to generate the transformed image. Since the spectrograph output image needs to be transformed in the wavelength plane only, a cylindrical lens should be used. The desired image, a



mapping of reflectance versus depth for each of the sample points conjugate to the entrance slit, could then be available at the focal plane of the lens (FP) in real time. The speed limitation in this system is introduced by the OASLM.

In this example, all of the information may be available in real time at plane  
 5 FP. The limiting factor in the speed of image acquisition may then be the signal strength and the detector (OASLM) sensitivity. The transverse resolution of the system is determined by the imaging characteristics of the spectrograph. The Chromex 500 IS has a resolution of 40  $\mu\text{M}$  at the center of the 10 mm field. Given the 10x magnification of the input beam this would result in a resolution of 4  $\mu\text{M}$  on the  
 10 image plane. Depth information is encoded as a function of wavelength (Equation 2.5), and depth and wavelength are related by

$$dz = \frac{1}{4 \cdot n} \cdot \frac{\lambda^2}{d\lambda} \quad [4.1]$$

Where  $dz$  [nm] is the depth increment,  $d\lambda$  [nm] is the wavelength increment at the spectrograph image plane,  $\lambda$  [nm] is the center wavelength of the source and  $n$  is the  
 15 index of refraction of the medium. Note that for the spectrograph, the wavelength resolution and total coverage are described by

$$\delta\lambda = \text{Slit} \cdot \text{RLD} \quad [4.2]$$

$$\Delta\lambda = \text{Field} \cdot \text{RLD} \quad [4.3]$$

20 Where  $\delta\lambda$  [nm] is the spectrograph resolution and  $\Delta\lambda$  [nm] the total wavelength coverage. *Slit* [mm] is the entrance slit width and *Field* [mm] is the width of the spectrograph field at the output plane. *RLD* [nm/mm] is the reciprocal linear dispersion of the spectrograph, a measure of the spectrograph's dispersive power.

Substituting Equation 4.2 into Equation 4.1 one obtains  $z_{\text{max}}$ , an estimate of the  
 25 maximum depth coverage allowed by the spectrograph. Using representative values: *Slit* = 50  $\mu\text{m}$ , *RLD* = 1.5 nm/mm,  $\lambda$  = 855 nm, and a worst-case  $n$  = 1.5 yields a  $z_{\text{max}}$  = 1.62 mm. Similarly, substituting Equation 4.3 into Equation 4.1 one gets  $\delta z$ , an estimate of the depth resolution given by the spectrograph. Using the same parameters as above and *Field* = 20 mm (Chromex specification) yields  $\delta z$  = 4.06  $\mu\text{m}$ . Note that  
 30 the depth coverage can be improved by making the entrance slits smaller, though this

would come with a decrease in signal. Resolution could be improved by increasing the size of the useful field, although as shown below factors other than the spectrograph limit the ultimate depth resolution.

In the all-optical implementation, the spectrograph output image is converted to a reflective pattern by the OASLM and then illuminated by a coherent source. After this incoherent-to-coherent transformation, a lens transforms the intensity distribution. The lens imaging properties are therefore of interest. At the Fourier plane of a lens, the distance from the optical axis ( $x$  [mm]) of a signal peak is related to a corresponding spatial period ( $a$  [mm]) by

$$x = f \cdot \tan\left(\frac{\lambda_R \cdot m}{a}\right) \quad [4.4]$$

Here  $m$  is the diffraction order ( $=1$  in this case),  $\lambda_R$  [nm] the readout wavelength and  $f$  [mm] the focal length of the lens. Identifying the spatial period  $a$  with the resolution of the spectrograph  $\delta\lambda/RLD = Slit$ , one obtains  $x_{z_{max}}$ , the  $x$  position of the maximum resolvable depth. Conversely, identifying  $a$  with  $\Delta\lambda/RLD = Field$ ,  $x_{\delta\lambda}$  results as the system's depth resolution. Substituting Equations 4.2 and 4.3 into Equation 4.1, and itself into 4.4 results in

$$x_{z_{max}} = f \cdot \tan\left(4 \cdot n \cdot RLD \cdot \frac{\lambda_R}{\lambda^2} \cdot z_{max}\right) \quad [4.5]$$

$$x_{\delta\lambda} = f \cdot \tan\left(4 \cdot n \cdot RLD \cdot \frac{\lambda_R}{\lambda^2} \cdot \delta\lambda\right) \quad [4.6]$$

Note that  $\lambda$  refers to the wavelength of light impinging on the OASLM and  $\lambda_R$  to the wavelength of the readout light. The final aspect to be taken into account is the imaging resolution of the lens. By the Rayleigh criterion, two spots are resolvable if they are separated by

$$x_{Rayleigh} = 1.22 \cdot \frac{f\lambda_R}{D} \quad [4.7]$$

Where  $f$  [mm] is the focal length of the lens,  $\lambda_R$  [nm] is the readout wavelength and  $D$  [mm] is the lens aperture. Equating  $x_{Rayleigh}$  and  $x_{\delta\lambda}$  results in

$$\delta z = \frac{1}{4 \cdot n \cdot RLD} \cdot \frac{\lambda^2}{\lambda_R} \cdot \tan^{-1} \left( \frac{1.22E-6}{D} \cdot \lambda_R \right) \quad [4.8]$$

where the factor 1E-6 results from expressing  $x_{Rayleigh}$  in mm in Equation 4.7. Given that the argument of the tangent is small in Equation 4.6, Equation 4.8 can be approximated as

$$\delta z = \frac{1.22E-6}{4 \cdot n \cdot RLD} \cdot \frac{\lambda^2}{D} \quad [4.9]$$

For the system values,  $\lambda=855$  nm,  $RLD=1.5$  nm/mm and  $D=20$  mm, and using a worst-case  $n=1$ ,  $\delta z=7.43$   $\mu$ m. While this is larger than the estimate obtained from the spectrograph alone, this is smaller than the calculated depth resolution from the bandwidth-limited estimate (Equation 2.2) of 12.75  $\mu$ m. Thus the latter will be the limiting factor in the depth resolution of the system.

Using 12.75  $\mu$ m as a value for depth resolution, and a focal distance  $f=300$  mm results in (Equation 4.6)  $x_{\delta} = 19.87$   $\mu$ m. An array sensor placed at the focal plane of the lens would therefore have to oversample  $x_{\delta}$  according to the Nyquist criterion. The x dimension of the pixels should thus be  $< 9.93$   $\mu$ m. The imaging resolution constrains the resolution in the y dimension to 40  $\mu$ m and so the y dimension of the pixels should be  $< 20$   $\mu$ m. Both of these dimensions are readily achieved with commercially available array detectors such as CCDs.

## References

The following references, to the extent that they provide exemplary procedural or other details supplementary to those set forth herein, are specifically incorporated herein by reference.

5

Alfano, Liu, Sha, Zhu, Akins, Cleary, Prudente, Cellmer, "Human Breast Tissues Studied by IR Fourier Transform Raman Spectroscopy," *Las. Lif. Sci.*, 4:1-6, 1991.

10

Alfano, Tang, Pradham, Lam, S. J. Choy, Opher, "Fluorescence Spectra from Cancerous and Normal Human Breast and Lung Tissues," *IEEE Journ. Quant. Electron.*, QE-23:1806-1811, 1987.

American Cancer Society Online. Cancer Facts and Figures-1997, In: <http://www.cancer.org/bottomcancinfo.html>.

15

Anderson *et al.*, "Organisation and Results of the Cervical Cytology Screening Programme in British Columbia," *Br. Med. J.*, 1988, 296:975-978, 1955-1985.

Bail *et al.*, "Optical coherence tomography with the "spectral radar": fast optical analysis in volume scatterers by short-coherence interferometry," *Proc SPIE Int Soc Opt Eng*, 1996.

20

Baraga, Feld, Rava, "In Situ Optical Histochemistry of Human Artery Using Near Infrared Fourier Transform Raman Spectroscopy," *Proc. Nat. Acad. Sci. USA*, 89:3473-3477, 1992.

Barer, "Refractometry and Interferometry of Living Cells," *Journal of the Optical Society of America A*, pp. 545-556, 1957.

25

Berchuk, "Biomarkers in the Ovary," *Journal of Cellular Biochemistry*, S23:223-226, 1995.

P. Bernasconi, G. Montemezzani, M. Wintermantel, I. Biaggio, and P. Gunter, "High-resolution, high-speed photorefractive incoherent-to-coherent optical converter," *Optics Letters*, vol. 24, pp. 199-201, 1999.

30

Bigio and Mourant, "Ultraviolet and Visible Spectroscopies for Tissue Diagnostics: Fluorescence Spectroscopy and Elastic-scattering Spectroscopy," *Physics Med. Biol.*, 42(5):803-814, 1997.

- Bigio, Boyer, Johnson, Lacey, Mourant, "Detection of Gastrointestinal Cancer by Elastic Scattering and Absorption Spectroscopies with the Los Alamos Optical Biopsy System," presented at Advances in Laser and Light Spectroscopy to Diagnose Cancer and Other Diseases II, San Jose, CA, 1995.
- 5 Bigio, Mourant, Boyer, Johnson, Shimada, Conn, "Noninvasive Identification of Bladder Cancer with Subsurface Backscattered Light," presented at Advances in Laser and Light Spectroscopy to Diagnose Cancer and Other Diseases, Los Angeles, CA, 1994.
- 10 Boersma, Nooter, Oostrum, Stoter, "Quantification of Apoptotic Cells with Fluorescein Isothiocyanate Labeled Annexin-V in Chinese Hamster Ovary Cell Cultures Treated with Cisplatin," *Cytometry*, 24:123-130, 1996.
- Bohorfoush, "Tissue Spectroscopy for Gastrointestinal Diseases," *Endoscopy*, 28(4):372-380, 1996.
- Boppart, Brezinski, Bouma, Tearney, Fujimoto, *Dev. Biol.*, 177:54-63, 1996a.
- 15 Boppart, Brezinski, Tearney, Bouma, Fujimoto, *J. Neurosci. Methods*, 70:65-72, 1996b.
- Boppart, Tearney, Bouma, Southern, Brezinski, Fujimoto, "Noninvasive assessment of the developing *Xenopus* cardiovascular system using optical coherence tomography," *Proc. Natl. Acad. Sci. USA*, 94:4256-4261, 1997.
- 20 Bouma *et al.*, "Optical Coherence Tomographic Imaging of Human Tissue at 1.55  $\mu\text{m}$  and 1.81  $\mu\text{m}$  using Er- and Tm-Doped Fiber Sources," *J. Biomed. Optics*, 3(1):76-79, 1998.
- Brezinski, Tearney, Bouma, Izatt, Hee, Swanson, Southern, Fujimoto, "Optical coherence tomography for optical biopsy," *Circulation*, 93:1206-1213, 1996.
- 25 Burke, Antonioli, Ducatman, *In: Colposcopy, Text and Atlas*, Appleton and Large, Norwalk, CT, 1991.
- Cantor, Follen-Mitchell, Tortelero-Luna, Bratka, Bodurka, Richards-Kortum, "Cost-Effectiveness Analysis of Diagnosis and Management of Cervical SIL," *Obstetrics and Gynecology*, (IN PRESS), 1998.
- 30 Cheong, Prahl, Welch, "A review of the optical properties of biological tissues," *IEEE J. Quant. Elect.*, QE-26:2166-2185, 1990.

- Chinn, Swanson, Fujimoto, "Optical Coherence Tomography Using a Frequency-Tunable Optical Source," *Optics Letters*, 22(5):340-342, 1997.
- Clivaz *et al.*, "High-Resolution Reflectometry in Biological Tissues," *Opt. Lett.*, 17:4, 1992.
- 5 Clivaz, Marquis-Weible, Salathe, "Optical Low Coherence Reflectometry with 1.9  $\mu$ m Spatial Resolution," *Electron. Lett.*, 28:1553-1555, 1992.
- Coifman, Roklin, Wandzura, "The Fast Multipole Method of the Wave Equation," *IEEE Antennas and Propagation*, 35:7-12, 1993.
- Copenhaver, Kelly, Wood, In: *Bailey's Textbook of Histology*, 17 ed., The Williams  
10 and Wilkins Company, Baltimore, 1978.
- Cothren, Richards-Kortum, Sivak, Fitzmaurice, Rava, Boyce, Doxtader, Blackman, Ivanc, Hayes, Feld, Petras, "Gastrointestinal tissue diagnosis by laser-induced fluorescence spectroscopy at endoscopy," *Gastrointest. Endosc.*, 36:105-111, 1990.
- 15 Cothren, Sivak, Van Dam, Petras, Fitzmaurice, Crawford, Wu, Brennan, Rava, Manoharan, Feld, "Detection of Dysplasia at Colonoscopy Using Laser-Induced Fluorescence: A Blinded Study," *Gastrointest. Endosc.*, 1995.
- Danielson and Whittenberg, "Guided-wave Reflectometry with Micrometer Resolution," *Applied Optics*, 26(14):2836-2842, 1987.
- 20 Davidovits and Egger, *Appl. Opt.*, 10:1615, 1971.
- Deligdisch, Einstein, Guera, Gil, "Ovarian Dysplasia in Epithelial Inclusion Cysts," *Cancer*, 76:1027-1034, 1995.
- Dunn and Richards-Kortum, "Three-Dimensional Computation of Light Scattering from Cells," *IEEE Journal of Selected Topics in Quantum Electronics*, 2:898-  
25 905, 1996.
- Dunn *et al.*, "Sources of Contrast in Confocal Reflectance Imaging," *Applied Optics*, 35(19):3441-3446, 1996.
- Durkin, Jaikumar, Ramanujam, Richards-Kortum, "Relation Between Fluorescence Spectra to Dilute and Turbid Samples," *Appl. Opt.*, 33:414-423, 1994.
- 30 Evers and Heineman, In: *Gynecology. A Clinical Atlas*, 1st ed., The C.V. Mosby Company, Ontario, 1990.

- Fahey, Irwig, Macaskill, "Meta-analysis of Pap Test Accuracy," *Am. J. Epidemiol.*, 141(7):680-689, 1995.
- Feldchtein, F.I., Gelikonov, G.V., Gelikonov, V.M., Kuranov, R.V. and Sergeev, A.M. *Optics Express* 3, 257-270 (1998).
- 5 Fercher *et al.*, "Measurement of Optical Distances by Optical Spectrum modulation," *In: SPIE*, 1994.
- Fercher, "New techniques in OCT," *Conf. Proc. Laser Electr. Optic. Soc. Annu. Meet.*, pp 54-55, 1997.
- Fercher, Hitztenberger, Drexler, Kamp, Sattmann, *Am. J. Ophthalmol.*, 116:113, 1993.
- 10 Fercher, Hitztenberger, Juchem, "Measurement of intraocular Optical Distances Using Partially Coherent Laser Light," *Journal of Modern Optics*, 38(7):1327-1333, 1991.
- Fercher, Mengedocht, Werner, "Eye-Length Measurement by Interferometry with Partially Coherent Light," *Opt. Lett.*, 13:186-188, 1988.
- 15 Fogh, *Human Tumor Cells in vitro*. New York: Plenum Press, 1975.
- Foster, "Determination of the Refractive Index Dispersion of Liquid Nitrobenzene in the Visible and UV," *J. Phys. D: Appl. Phys.*, 25:525-529, 1992.
- Fujimoto, Brezinski, Tearney, Boppart, Bouma, Hee, Southern, Swanson, "Optical biopsy and imaging using optical coherence tomography," *Nat. Med.*, 1:970-972, 1995.
- 20 Fukano, T. and Yamaguchi, I. *Opt Lett* (1996).
- Gelikonov, Gelikonov, Feldchtein, Stepanov, Sergeev, Antoniou, Ionnovich, Reitze, Dawson, "Two-Color-In-One-Interferometer OCT System For Bioimaging," presented at Conference on Lasers and Electro-Optics, 1997.
- 25 Gilgen, *et al.*, "Submillimeter optical reflectometry," *IEEE J. Lightwave Techno.*, 8:1225-1233, 1989.
- Goins, Phillips, Klipper, Rudolph, "Role of Complement in Rats Injected with Liposome Encapsulated Hemoglobin," *Journal of Surgical Research*, 68:99-105, 1997.
- 30 Goodman, *In: Statistical Optics*, John Wiley and Sons, New York, 1985.

- Haberland, *et al.*, "Optical Coherence Tomography of Scattering Media Using Frequency Modulated Continuous Wave Techniques with Tunable Near-infrared Laser," *Proc. SPIE*, 2981:20-28, 1997.
- Harrison and Braunwald, *In: Harrison's Principles of Internal Medicine*, Vol. 1, MacGraw - Hill, New York, 1987.
- 5 Hausler and Lindner, "Coherence Radar" and "Spectral Radar" -- New Tools for Dermatological Diagnosis," *Journal of Biomedical Optics*, 3(1):21-31, 1998.
- Hee *et al.*, "Optical coherence tomography for ophthalmic imaging," *IEEE Eng. Med. Biol.*, 14(1):1-5, 1994.
- 10 Hee *et al.*, "Optical Coherence Tomography for Micron-Resolution Ophthalmic Imaging," *IEEE Eng. Med. Biol. Mag.*, 67-76, 1995.
- Hee, Izatt, Swanson, Huang, Schuman, Lin, Puliafito, Fujimoto, "Optical coherence tomography of the human retina," *Arch. Ophthalmol.*, 113:325-332, 1995b.
- Hee, Puliafito, Wong *et al.*, "Quantitative assessment of macular edema with optical coherence tomography," *Arch. Ophthalmol.*, 113:1019-1029, 1995c.
- 15 Hee, Puliafito, Wong, *et al.*, "Optical coherence tomography of macular holes," *Ophthalmology*, 102:748-756, 1995a.
- Hitzenberger, Drexler, Fercher, "Measurement of corneal thickness by laser doppler interferometry," *Invest. Ophthalmol. Vis. Sci.*, 33:98-103, 1992.
- 20 Hodgson, *Optical Absorption and Dispersion in Solids*. London: Chapman and Hall Ltd., 1970.
- Hoffman, "Three Dimensional Histoculture: Origin and Applications in Cancer Research," *Cancer Cells*, 3:86-92, 1991.
- Hoskins, "Prospective on Ovarian Cancer: Why Prevent?," *Journal of Cellular Biochemistry*, S23:189-199, 1995.
- 25 Huang, Swanson, Lin, Schuman, Stinson, Chang, Hee, Flotte, Gregory, Puliafito, Fujimoto, "Optical coherence tomography," *Science*, 254:1178-1181, 1991.
- Hung, *et al.*, "Autofluorescence of normal and malignant bronchial tissue," *Las. Surg. Med.*, 11:99-105, 1991.
- 30 Izatt *et al.*, "Micrometer-scale resolution imaging of the anterior eye *in vivo* with optical low coherence tomography," *Arch. Ophthalmol.*, 112:1584-1589, 1994.



- Izatt *et al.*, "Micron-Resolution Biomedical Imaging with Optical Coherence Tomography," *Opt. Photon. News*, 4:14, 1993.
- Izatt *et al.*, "Ophthalmic Diagnostics using Optical Coherence Tomography," *Proc. Soc. Photo-Opt. Instrum. Eng.*, 1877:136, 1993.
- 5 Izatt *et al.*, "Optical Coherence Microscopy in Scattering Media," *Opt. Lett.*, 19:590-592, 1994.
- Izatt *et al.*, "Optical Coherence Tomography and Microscopy in Gastrointestinal Tissues," *In: Advances in Optical Imaging and Photon Migration*, Orlando, FL: OSA, 1996.
- 10 Izatt, Hee, Swanson, Lin, Huang, Schuman, Puliafito, Fujimoto, "Micrometer-scale resolution imaging of the anterior eye *in vivo* with optical coherence tomography," *Arch Ophthalmol.*, 112:1584-1589, 1994.
- Izatt, J.A., Kulkarni, M.D., Wang, H.-W., Kobayashi, K. and Sivak, M.V. *IEEE J. Sel. Top. Quant. Electron.* 4, 1017-1028 (1996).
- 15 Kabawat, Bast, Bhan, Welch, Knap, Colvin, "Tissue Distribution of a Coelomic Epithelium Related Antigen Recognized by the Monoclonal Antibody OC-125," *International Journal of Gynecology Pathology*, 2:275-285, 1983.
- Kelloff *et al.*, "Intermediate Biomarkers of Precancers and their Application in Chemoprevention," *J. Cell. Biochem., Suppl(16G)*:15-21, 1992.
- 20 Knuettel *et al.*, "Tissue characterization with optical coherence tomography (OCT)," *Proc. SPIE Int. Soc. Opt. Eng.*, 2676:54-64, 1996.
- Lam, MacAulay, Hung, LeRiche, Profio, Palcic, "Detection of dysplasia and carcinoma *in situ* with a lung imaging fluorescence endoscope device," *J. Thorac. Cardiovasc. Surg.*, 105:1035-1040, 1993.
- 25 Lankenau *et al.*, "In vivo OCT at Different Wavelengths," *In: OSA, Advances in Optical Imaging and Photon Migration*, Orlando, FL, 1988.
- Lerman, *Journal of the American Medical Association*, 275:1185-1189, 1996.
- Mahadevan, Follen Mitchell, Silva, Thomsen, Richards-Kortum, "Study of the Fluorescence Properties of Normal and Neoplastic Human Cervical Tissue,"
- 30 *Lasers in Surgery and Medicine*, 13:647-655, 1993.

- McCreery, Frank, Redd, Gansler, "Raman Spectroscopy of Human Biopsy Specimens," presented at Advances in Fluorescence Sensing Technology II, San Jose, CA, 1995.
- 5 Miller, McEachern, Miller, "Growth Regulation of Mouse Mammary Tumor Cells in Collagen Gel Cultures by Diffusible Factors Produced by Normal Mammary Gland Epithelium and Stromal Fibroblasts," *Cancer Research*, 49:6091-6097, 1989.
- Mitchell, "The Accuracy of Colposcopy. Clinical Consultation in Obstetrics and Gynecology," 6(1):70-73, 1994.
- 10 Mittal, Zeleniuch-Jacquotte, Cooper, Demopoulos, "Contralateral Ovary in Unilateral Ovarian Carcinoma: A Search for Preneoplastic Lesions," *Int J. Gynecol. Pathol.*, 12:59-64, 1993.
- Mourant, Bigio, Boyer, Conn, Johnson, Shimada, "Spectroscopic Diagnosis of Bladder Cancer with Elastic Light Scattering," *Lasers in Surgery and Medicine*, 17:350-357, 1995.
- 15 Mourant, Boyer, Hielscher, Bigio, "Influence of the Scattering Phase Function on Light Transport Measurements in Turbid Media Performed with Small Source-Detector Separations," *Optics Letters*, 21:546-548, 1996.
- Mur, "Absorbing Boundary Conditions for Finite Difference Approximation of the Time Domain Electromagnetic Field Equations," *IEEE Transactions on Electromagnetic Compatibility*, EMC23:185-200, 1981.
- 20 Murphy and Lagarias, "The Phytofluors: A New Class of Fluorescent Protein Probes," *Current Biology*, 7:870-876, 1997.
- Nishioka, "Laser-induced Fluorescence Spectroscopy," *Gastrointestinal Endoscopy Clinics of North America*, 4(2):313-326, 1994.
- 25 Pan *et al.*, "Low-Coherence Optical Tomography in Turbid Tissue: Theoretical Analysis," *Appl. Opt.*, 34:6564-6574, 1995.
- Pawley, In: *Handbook of Biological Confocal Microscopy*, Plenum Press, New York, 1995.
- 30 Perelman, Backman, Wallace, Zonios, Manoharan, Nusrat, Shields, Seiler, Lima, Hamano, Itzkan, Van Dam, Crawford, Feld, "Observation of Periodic Fine

- Structure in Reflectance from Biological Tissue: A New Technique for Measuring Nuclear Size Distribution," *Physical Review Letters*, 80:627-630, 1998.
- 5 Plaxe, Deligdisch, Dottino, Cohen, "Ovarian Intraepithelial Neoplasia Demonstrated  
om Patients with Stage I Ovarian Carcinoma," *Gynecologic Oncology*, 38:367-  
372, 1990.
- Puliafito, Hee, Lin, Reichel, Schuman, Duker, Izatt, Swanson, Fujimoto, "Imaging of  
macular diseases with optical coherence tomography," *Ophthalmology*,  
102:217-229, 1995a.
- 10 Puliafito, Hee, Schuman, Fujimoto, "Optical coherence tomography of ocular  
diseases," SLACK, Thorofare, NJ, 1995b.
- Rajadhyaksha, Grossman, Esterowitz, Webb, Anderson, "In Vivo Confocal Scanning  
Laser Microscopy of Human Skin: Melanin Provides Strong Contrast,"  
*Journal of Investigative Dermatology*, 104:946-952, 1995.
- 15 Ramanujam *et al.*, "Fluorescence Spectroscopy: a Diagnostic Tool for Cervical  
Intraepithelial Neoplasia (CIN)," *Gynecol. Oncol.*, 52:31-38, 1994.
- Ramanujam, Follen Mitchell, Mahadevan, Thomsen, Malpica, Wright, Atkinson,  
Richards-Kortum, "Development of a Multivariate Statistical Algorithm to  
Analyze Human Cervical Tissue Fluorescence Spectra Acquired *in vivo*,"  
20 *Lasers in Surgery and Medicine*, 19:46-62, 1996.
- Ramanujam, Follen Mitchell, Mahadevan-Jansen, Thomsen, Staerkel, Malpica,  
Wright, Atkinson, Richards-Kortum, "Cervical Precancer Detection Using a  
Multivariate Statistical Algorithm Based on LIF Spectra at Multiple Excitation  
Wavelengths," *Photochemistry and Photobiology*, 64:720-735, 1996.
- 25 Reitze *et al.*, "Low Coherence Imaging of Cerebral Structures *in vivo*," In: *Coherence  
Domain Optical Methods in Biomedical Science and Clinical Applications*,  
San Jose, CA: SPIE, 1997.
- Resta, Russo, Colucci, Prat, "Morphologic Precursors of Ovarian Epithelial Tumors,"  
*Obstetrics and Gynecology*, 1993:181-186, 1993.
- 30 Richards-Kortum and Sevic-Muraca, "Quantitative Optical Spectroscopy for Tissue  
Diagnosis," *Annu. Rev. Phys. Chem.*, 47:555-606, 1996.

- Robbins and Kumar, *In: Pathologic Basis of Disease*, Philadelphia: W.B. Saunders Co., 1984.
- Robbins, Cotran, Kumar, *Pathologic Basis of Disease*, 3rd ed. Philadelphia, PA: W.B. Saunders Co., 1984.
- 5 Rollins and Izatt, "Video Rate Optical Coherence Tomography," *In: OSA, Advances in Optical Imaging and Photon Migration*, Orlando, FL, 1998.
- Roy *et al.*, "Diagnostic Fluorescence Spectroscopy of Oral Mucosa. in Lasers and Surgery: Advanced Characterization," *In: Therapeutics and Systems IV, SPIE*, Bellingham, 1995.
- 10 Schmitt *et al.*, "Optical Characterization of Dense Tissues Using Low-Coherence Interferometry," *Proc. Soc. Photo-Opt. Instrum. Eng.*, 1889:197, 1993.
- Schmitt, Knuttel, Bonner, "Measurement of Optical Properties of Biological Tissues by Low-Coherence Reflectometry," *Appl. Opt.*, 32:6032-6042, 1993.
- Schmitt, Knuttel, Eckhaus, "Optical-Coherence Tomography of a Dense Tissue:
- 15 Statistics of Attenuation and Backscattering," *Phys. Med. Biol.*, 39:1705, 1994.
- Schmitt, Knuttel, Yadlowsky, "Confocal Microscopy in Turbid Media," *J. Opt. Soc. Am. A.*, 11:2226-2235, 1994.
- Schmitt, Yadlowsky, Bonner, "Subsurface imaging of living skin with optical coherence microscopy," *Dermatology*, 191:93-98, 1995.
- 20 Schmitt, J.M., Yadlowsky, M.J. and Bonner, R.F. *Dermatology* 191, 93-98 (1995).
- Schomacker *et al.*, "Ultraviolet Laser-Induced Fluorescence of Colonic Tissue: Basic Biology and Diagnostic Potential," *Las. Surg. Med.*, 12:63-78, 1992.
- Schuman *et al.*, "Quantification of Nerve Fiber Thickness in Normal and Glaucomatous Eyes using Optical Coherence Tomography: A Pilot Study,"
- 25 *Arch. Ophthalmol.*, 113:586-596, 1995.
- Scully, "Pathology of Ovarian Cancer Precursors," *J. Cell Biochem*, 23:208-218, 1995.
- Sergeev, Gelikonov, Gelikonov, Feldchtein, Gladkova, Kamensky, "Biomedical Diagnostics Using Optical Coherence Tomography," presented at *Advances in*
- 30 *Optical Imaging and Photon Migration*, Orlando, FL, 1996.

- Sergeev, Gelikonov, Gelikonov, Feldchtein, Kuranov, Gladkova, "In vivo endoscopic OCT imaging of precancer and cancer states of human mucosa," *Optics Express*, 1:432, 1997.
- 5 Sevick-Muraca, Lopez, Reynolds, Troy, Hutchinson, "Fluorescence and Absorption Contrast Mechanisms for Biomedical Optical Imaging using Frequency Domain Techniques," *Photochemistry and Photobiology*, 66:55-64, 1997.
- Smithpeter, "Fiber optic confocal imaging for *in vivo* detection and diagnosis of pre-cancerous lesions," 1997.
- 10 Speroff, Glass, Kase, "Regulation of the Menstrual Cycle," in *Clinical Gynecologic Endocrinology and Infertility*. Maryland: Williams and Wilkins, 1994.
- Svanberg, Andersson-Engels, Berg, Johansson, Svanberg, Wang, "Tissue Characterization in Different Malignant Tumors Utilizing Laser-Induced Fluorescence," presented at Advances in Laser and Light Spectroscopy to Diagnose Cancer and Other Diseases II, San Jose, CA, 1995.
- 15 Swanson *et al.*, "High Speed Optical Coherence Domain Reflectometry," *Opt. Lett.*, 17(2):151-153, 1992.
- Swanson, Izatt, Hee, Huang, Lin, Schuman, Puliafito, Fujimoto, "In vivo retinal imaging by optical coherence tomography," *Optics Lett.*, 18:1864-1866, 1993.
- 20 Takada, Yokohama, Chida, Noda, "New measurement system for fault location in optical waveguide devices based on an interferometric technique," *Appl. Opt.*, 26:1603-1606, 1987.
- Tearney *et al.*, "Endoscopic Optical Coherence Tomography," In: *Optical Tomography and Spectroscopy of Tissue: Instrumentation, Model, and Human Studies II*, San Jose, CA: SPIE, 1997.
- 25 Tearney *et al.*, "Scanning single-mode fiber optic catheter-endoscope for optical coherence tomography," *Opt. Lett.*, 21(7):543-545, 1996.
- Tearney, Brezinski, Bouma, Boppart, Pitris, Southern, Fujimoto, "In vivo endoscopic optical biopsy with optical coherence Tomography," *Science*, 276:2037-2039, 1997.
- 30 Tearney, Webb, and Bouma, "Spectrally encoded confocal microscopy" *Optics Letters*, 23 (15): 1152-1154, August 1, 1998.

- Toth, Narayan, Boppart, Hee, Fujimoto, Birngruber, Cain, DiCarlo, Roach, "A comparison of retinal morphology viewed by optical coherence tomography and by light microscopy," *Arch Ophthalmol.*, 115:1425-1428, 1997.
- 5 Tsay and Pozar, "Application of the FDTD Technique to Periodic Problems in Scattering and Radiation," *IEEE Microwave Guided Wave Letters*, 3:250-252, 1993.
- Tumer, Ramanujam, Ghosh, Richards-Kortum, "Ensembles of Radial Basis Function Networks for Spectroscopic Detection of Cervical Pre-Cancer," *IEEE Transactions on Biomedical Engineering*, (IN PRESS), 1998.
- 10 Van de Hulst, *Light Scattering by Small Particles*. New York: John Wiley and Sons, Inc., 1957.
- Vaupel, Kallinowski, Okunieff, "Blood Flow, Oxygen and Nutrient Supply, and Metabolic Microenvironment of Human Tumors: A Review," *Blood Flow and Metabolism of Human Tumors*, pp. 6449-6465, 1989.
- 15 Vermes, Haanen, Steffens-Nakken, Reutelingsperfer, "A Novel Assay for Apoptosis Flow Cytometric Detection of Phosphatidyl Serine Expression on Early Apoptotic Cells Using Fluorescein Labelled Annexin V," *Journal of Immunologic Methods*, 184:39-51, 1995.
- Vienot, J.C., Goedgebuer, J.P. and Lacourt, A. *Applied Optics* 16, 454-461 (1977).
- 20 Vo-Dinh, Panjehpour, Overholt, Farris, Buckley, Sneed, "In Vivo Cancer Diagnosis of the Esophagus Using Differential Normalized Fluorescence (DNF) Indices," *Las. Surg. Med.*, 16:41-47, 1995.
- Webb, Hughes, Delori, "Confocal Laser Scanning Ophthalmoscope," *Applied Optics*, 26(8):1492-1499, 1987.
- 25 Webb, Hughes, Delori, *ibid.*, 26:1492, 1987.
- Weedon, Chew, Rappaport, "Computationally Efficient FDTD Simulation of Open Region Scattering Problems on the Connection Machine," *IEEE Antennas and Propagation Soc. Int. Symp.*, 1:376-379, 1994.
- Welch and van Gemert, *In: Optical-Thermal Response of Laser-Irradiated Tissue*,  
30 Plenum Press, New York, NY, 1995.

- Wilson and Sheppard, In: *Theory and Practice of Scanning Optical Microscopy*, Academic Press, London, 1984.
- Wingo, "Cancer Statistics," *CA Cancer J. Clin.*, 45:8-30, 1995.
- Wu, Feld, Rava, "Analytical Model for Extracting Intrinsic Fluorescence in Turbid Media," *Applied Optics*, 32:3585-3595, 1993.
- Wyllie, "Apoptosis and Carcinogenesis," *European Journal of Cell Biology*, 73:189-197, 1997.
- Yoshiya, Shimada, Tanaka, "Spectrophotometric Monitoring of Arterial Oxygen Saturation in the Fingertip," *Med. Biol. Eng. and Comp.*, 18:27-32, 1980.
- Young, Woodburn, Wright, Mody, Fan, Sessler, Dow, Miller, "Lutetium Texaphyrin: A NIR Water Soluble Photosensitizer," *Photochemistry and Photobiology*, 63:892-897, 1996.
- Youngquist, Carr, Davies, "Optical coherence-domain reflectometry: A new optical evaluation technique," *Opt. Lett.*, 12:158-160, 1987.
- Zeylikovich, I., Gilerson, A. and Alfano, R.R. *Optics Letters* 23, 1797-1799 (1998).

All of the methods and apparatus disclosed and claimed herein can be made and executed without undue experimentation in light of the present disclosure. While the compositions and methods of this invention have been described in terms of preferred embodiments, it will be apparent to those of skill in the art that variations may be applied to the methods and apparatus and in the steps or in the sequence of steps of the method described herein without departing from the concept, spirit and scope of the invention. More specifically, it will be apparent that certain agents which are both chemically and physiologically related may be substituted for the agents described herein while the same or similar results would be achieved. All such similar substitutes and modifications apparent to those skilled in the art are deemed to be within the spirit, scope and concept of the invention as defined by the appended claims.

**CLAIMS:**

1. An apparatus for subsurface imaging of a sample, comprising:
  - a radiation source;
  - 5 an interferometer in optical communication with said source;
  - a scanning probe in optical communication with said interferometer and said sample, comprising:
    - an optical fiber configured to receive radiation from said radiation source and to direct said radiation toward said sample; and
    - 10 a piezoelectric scanner coupled to said probe and configured to scan said radiation relative to said sample; and
    - a detector in optical communication with said scanning probe.
- 15 2. The apparatus of claim 1, wherein said scanning probe is a scanning side-looking probe comprising an optical element in optical communication with said fiber, said optical element configured to direct radiation from said fiber toward said sample in a direction that is substantially non-parallel with said fiber.
- 20 3. The apparatus of claim 1, wherein said piezoelectric scanner comprises a piezoelectric bender.
4. The apparatus of claim 1, wherein said scanning probe further comprises a GRIN lens coupled to said optical fiber.
- 25 5. The apparatus of claim 1, wherein said scanning probe further comprises a sterilizable cover configured to cover at least a portion of said scanning probe.
6. The apparatus of claim 1, wherein said scanning probe further comprises an optical window coupled to said scanning probe adjacent said optical fiber.



7. The apparatus of claim 1, wherein said scanning probe further comprises an inner and outer tube enclosing at least a portion of said scanning probe.

8. An apparatus for subsurface imaging of a sample, comprising:

- 5 a radiation source;
- an interferometer in optical communication with said source;
- a scanning probe in optical communication with said interferometer and sample, comprising:
  - an optical fiber configured to receive radiation from said radiation
  - 10 source and to direct said radiation toward said sample; and
  - a mirror scanner coupled to said probe and configured to scan said radiation relative to said sample; and
  - a detector in optical communication with said scanning probe.

15 9. The apparatus of claim 8, wherein said mirror scanner comprises a mirror coupled to an electromagnetically powered micromotor.

10. An apparatus for subsurface imaging of a sample, comprising:

- a radiation source;
- 20 an interferometer in optical communication with said source;
- a scanning probe in optical communication with said interferometer and sample, comprising:
  - an optical fiber configured to receive radiation from said radiation
  - source and to direct said radiation toward said sample; and
  - 25 a galvanometric scanner coupled to said probe and configured to scan said radiation relative to said sample; and
  - a detector in optical communication with said scanning probe.

11. The apparatus of claim 10, wherein said galvanometric scanner comprises one or  
30 more permanent magnets in operative relation with said optical fiber.

12. An apparatus for subsurface imaging of a sample, comprising:

a radiation source;

an interferometer in optical communication with said radiation source;

a probe in optical communication with said interferometer and said sample,

5 comprising:

an optical fiber configured to receive radiation from said radiation  
source and to direct said radiation toward said sample; and

a spectroscopy module in optical communication with said sample and  
configured to measure optical spectroscopy of said sample

10 simultaneously with optical coherence imaging of said sample;

and

a detector in optical communication with said probe.

13. The apparatus of claim 12, wherein said probe is a scanning probe comprising a  
15 piezoelectric scanner configured to scan said radiation from said radiation source  
relative to said sample.

14. The apparatus of claim 12, wherein said probe is a scanning probe comprising a  
mirror scanner configured to scan said radiation from said radiation source relative to  
20 said sample.

15. The apparatus of claim 12, wherein said probe is a scanning probe comprising a  
galvanometric scanner configured to scan said radiation from said radiation source  
relative to said sample.

25 16. The apparatus of claim 12, wherein said spectroscopy module further comprises a  
dichroic mirror configured to direct said radiation from said radiation source into said  
optical fiber.

17. The apparatus of claim 12, wherein said spectroscopy module further comprises an optical fiber configured to direct radiation toward said sample.

18. The apparatus of claim 12, wherein said spectroscopy module is a multi-  
5 wavelength spectroscopy module further comprising a spectrograph in optical communication with said probe.

19. The apparatus of claim 12, wherein said optical spectroscopy comprises fluorescence, reflectance, or Raman spectroscopy.

10

20. An apparatus for subsurface imaging of a sample, comprising:

a radiation source;

an interferometer in optical communication with said radiation source;

a probe in optical communication with said interferometer and said sample,

15

comprising:

an optical fiber configured to receive radiation from said radiation  
source and to direct said radiation toward said sample; and

a surface imaging module in optical communication with said sample  
and configured to optically image said sample simultaneously

20

with optical coherence imaging of said sample; and

a detector in optical communication with said probe.

21. The apparatus of claim 20, wherein said probe is a scanning probe comprising a  
piezoelectric scanner configured to scan said radiation from said radiation source  
25 relative to said sample.

22. The apparatus of claim 20, wherein said probe is a scanning probe comprising a  
mirror scanner configured to scan said radiation from said radiation source relative to  
said sample.

30

23. The apparatus of claim 20, wherein said probe is a scanning probe comprising a galvanometric scanner configured to scan said radiation from said radiation source relative to said sample.

- 5 24. An apparatus for subsurface imaging of a sample, comprising:  
a radiation source;  
an interferometer in optical communication with said radiation source;  
a probe in optical communication with said interferometer and said sample,  
comprising:  
10 an optical fiber configured to receive radiation from said radiation  
source and to direct said radiation toward said sample; and  
a therapeutic module in optical communication with said sample and  
configured to apply therapeutic radiation to said sample  
simultaneously with optical coherence imaging of said sample;  
15 and  
a detector in optical communication with said probe.

25. The apparatus of claim 24, wherein said probe is a scanning probe comprising a piezoelectric scanner configured to scan said radiation from said radiation source  
20 relative to said sample.

26. The apparatus of claim 24, wherein said probe is a scanning probe comprising a mirror scanner configured to scan said radiation from said radiation source relative to  
said sample.

25 27. The apparatus of claim 24, wherein said probe is a scanning probe comprising a galvanometric scanner configured to scan said radiation from said radiation source  
relative to said sample.

28. An apparatus for multi-dimensional subsurface imaging of a sample without scanning, said apparatus comprising:

a radiation source in optical communication with said sample;

an interferometer in optical communication with said radiation source;

5 a detector in optical communication with said interferometer and said sample;  
and

an imaging spectrograph intermediate said interferometer and said detector.

29. The apparatus of claim 28, further comprising an optically addressed spatial light  
10 modulator in optical communication with said imaging spectrograph, a coherent  
source in optical communication with said optically addressed spatial light modulator,  
and a cylindrical lens in optical communication with said optically addressed spatial  
light modulator.

15 30. The apparatus of claim 28, further comprising an optical fiber bundle in optical  
communication with said interferometer and said sample, said optical fiber bundle  
configured to receive radiation from said radiation source and to direct said radiation  
though individual fibers of said optical fiber bundle toward said sample.

20 31. The apparatus of claim 30, wherein said optical fiber bundle comprises a one  
dimensional array of optical fibers.

32. The apparatus of claim 30, wherein said optical fiber bundle comprises a two  
dimensional array of optical fibers.

25 33. The apparatus of claim 30, further comprising a probe in optical communication  
with said radiation source and said sample, said probe housing at least a portion of  
said optical fiber bundle.

30 34. The apparatus of claim 33, wherein said probe is a side-looking probe comprising  
an optical element in optical communication with said fiber bundle, said optical

element configured to direct radiation from said fiber bundle toward said sample in a direction that is substantially non-parallel with said fiber bundle.

35. The apparatus of claim 33, wherein said probe is a radially-looking probe  
5 comprising one or more angle polished fibers.

36. The apparatus of claim 28, wherein said apparatus further comprises a spectroscopy module in optical communication with said sample and configured to analyze said sample simultaneously with optical coherence imaging of said sample.

10

37. The apparatus of claim 28, wherein said apparatus further comprises a surface imaging module in optical communication with said sample and configured to optically image said sample simultaneously with optical coherence imaging of said sample.

15

38. The apparatus of claim 28, wherein said apparatus further comprises a therapeutic module in optical communication with said sample and configured to apply therapeutic radiation to said sample simultaneously with optical coherence imaging of said sample.

20

39. An apparatus for multidimensional subsurface imaging of a sample without scanning, said apparatus comprising:

a confocal microscopy system comprising:

a radiation source;

25

an imaging spectrograph in optical communication with said sample;

and

a detector in optical communication with said sample; and

an optical fiber bundle configured to receive radiation from said radiation

source and to direct said radiation through individual fibers of said fiber

30

bundle toward said sample.

40. The apparatus of claim 39, further comprising an optically addressed spatial light modulator in optical communication with said imaging spectrograph, a coherent source in optical communication with said optically addressed spatial light modulator, and a cylindrical lens in optical communication with said optically addressed spatial light modulator.
41. The apparatus of claim 39, wherein said optical fiber bundle comprises a one dimensional array of optical fibers.
42. The apparatus of claim 39, wherein said optical fiber bundle comprises a two dimensional array of optical fibers.
43. The apparatus of claim 39, further comprising a probe in optical communication with said radiation source and said sample, said probe housing at least a portion of said optical fiber bundle.
44. The apparatus of claim 43, wherein said probe is a side-looking probe comprising an optical element in optical communication with said fiber bundle, said optical element configured to direct radiation from said fiber bundle toward said sample in a direction that is substantially non-parallel with said fiber bundle.
45. The apparatus of claim 43, wherein said probe is a radially-looking probe comprising one or more angle polished fibers.
46. The apparatus of claim 39, wherein said apparatus further comprises a spectroscopy module in optical communication with said sample and configured to analyze said sample simultaneously with confocal imaging of said sample.

47. The apparatus of claim 39, wherein said apparatus further comprises a surface imaging module in optical communication with said sample and configured to optically image said sample simultaneously with confocal imaging of said sample.

5 48. The apparatus of claim 39, wherein said apparatus further comprises a therapeutic module in optical communication with said sample and configured to apply therapeutic radiation to said sample simultaneously with confocal imaging of said sample.

10 49. A method for subsurface imaging of a sample, comprising:  
providing a radiation source, an interferometer in optical communication with said radiation source, a detector in optical communication with said interferometer, and an imaging spectrograph intermediate said interferometer and said detector;  
15 directing radiation from said radiation source to said sample;  
directing radiation from said sample to said interferometer, to said imaging spectrograph, and to said detector; and  
generating a multi-dimensional optical coherence tomography image of said sample.

20

50. The method of claim 49, further comprising:  
providing an optically addressed spatial light modulator in optical communication with said imaging spectrograph, a coherent source in optical communication with said optically addressed spatial light  
25 modulator, and a cylindrical lens in optical communication with said optically addressed spatial light modulator;  
converting output intensity of said imaging spectrography from incoherent to coherent with said optically addressed spatial light modulator; and  
performing a Fourier transformation with said cylindrical lens.

30



51. The method of claim 49, further comprising providing an optical fiber bundle in optical communication with said interferometer and said sample, said optical fiber bundle configured to receive radiation from said radiation source and to direct said radiation through individual fibers of said fiber bundle toward said sample.

5

52. The method of claim 49, further comprising:

providing a spectroscopy module in optical communication with said sample;

and

measuring optical spectroscopy of said sample simultaneously with optical

10

coherence imaging of said sample.

53. The method of claim 49, further comprising:

providing a surface imaging module in optical communication with said

sample; and

15

optically imaging said sample simultaneously with optical coherence imaging of said sample.

54. The method of claim 49, further comprising:

providing a therapeutic module in optical communication with said sample;

20

and

applying therapeutic radiation to said sample simultaneously with optical coherence imaging of said sample.

55. A method for subsurface imaging of a sample, comprising:

25

providing a confocal microscopy system including a radiation source, an imaging spectrograph in optical communication with said sample, and a detector in optical communication with said sample;

directing radiation from said radiation source to said sample;

directing radiation from said sample to said imaging spectrograph and to said

30

detector; and

generating a multi-dimensional confocal microscopy image of said sample.

56. The method of claim 55, further comprising:

5       providing an optically addressed spatial light modulator in optical  
communication with said imaging spectrograph, a coherent source in  
optical communication with said optically addressed spatial light  
modulator, and a cylindrical lens in optical communication with said  
optically addressed spatial light modulator;  
converting output intensity of said imaging spectrography from incoherent to  
coherent with said optically addressed spatial light modulator; and  
10       performing a Fourier transformation with said cylindrical lens.

57. The method of claim 55, further comprising providing an optical fiber bundle in  
optical communication with said sample and configured to receive radiation from said  
radiation source and to direct said radiation through individual fibers of said fiber  
15       bundle toward said sample.

58. The method of claim 55, further comprising:

20       providing a spectroscopy module in optical communication with said sample;  
and  
measuring optical spectroscopy of said sample simultaneously with confocal  
imaging of said sample.

59. The method of claim 55, further comprising:

25       providing a surface imaging module in optical communication with said  
sample; and  
optically imaging said sample simultaneously with confocal imaging of said  
sample.

60. The method of claim 55, further comprising:

30       providing a therapeutic module in optical communication with said sample;  
and

applying therapeutic radiation to said sample simultaneously with confocal imaging of said sample.

PRIOR ART

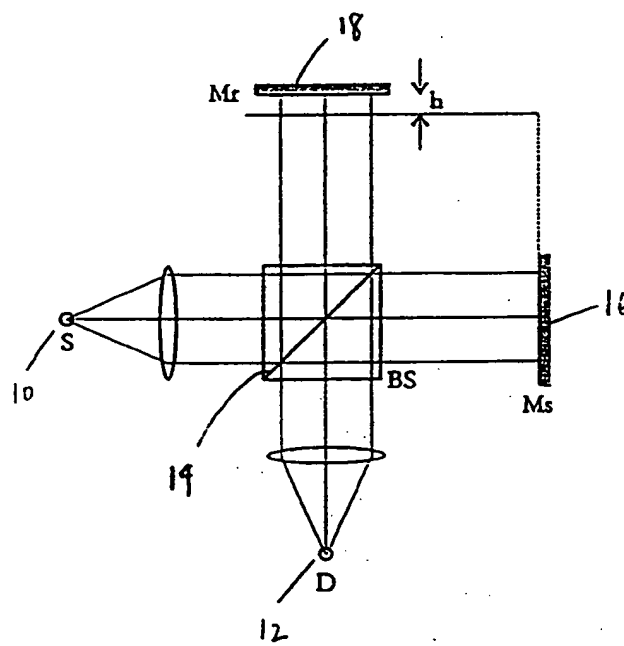
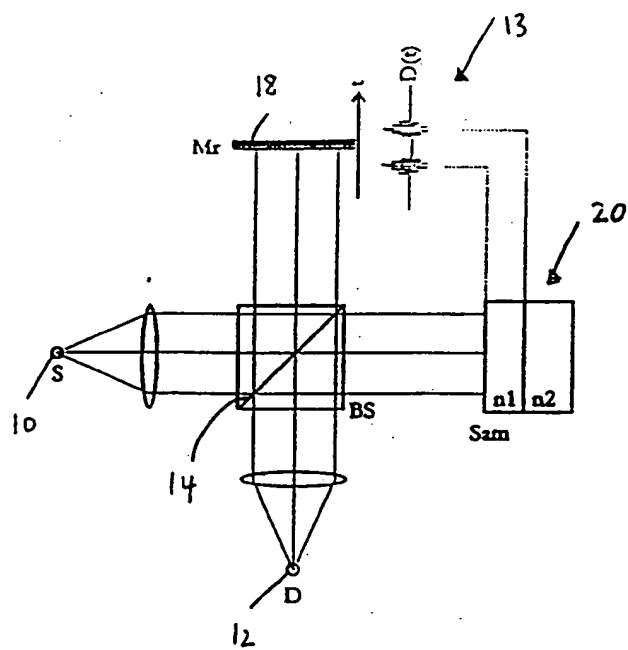


FIG. 1



PRIOR ART

FIG. 2

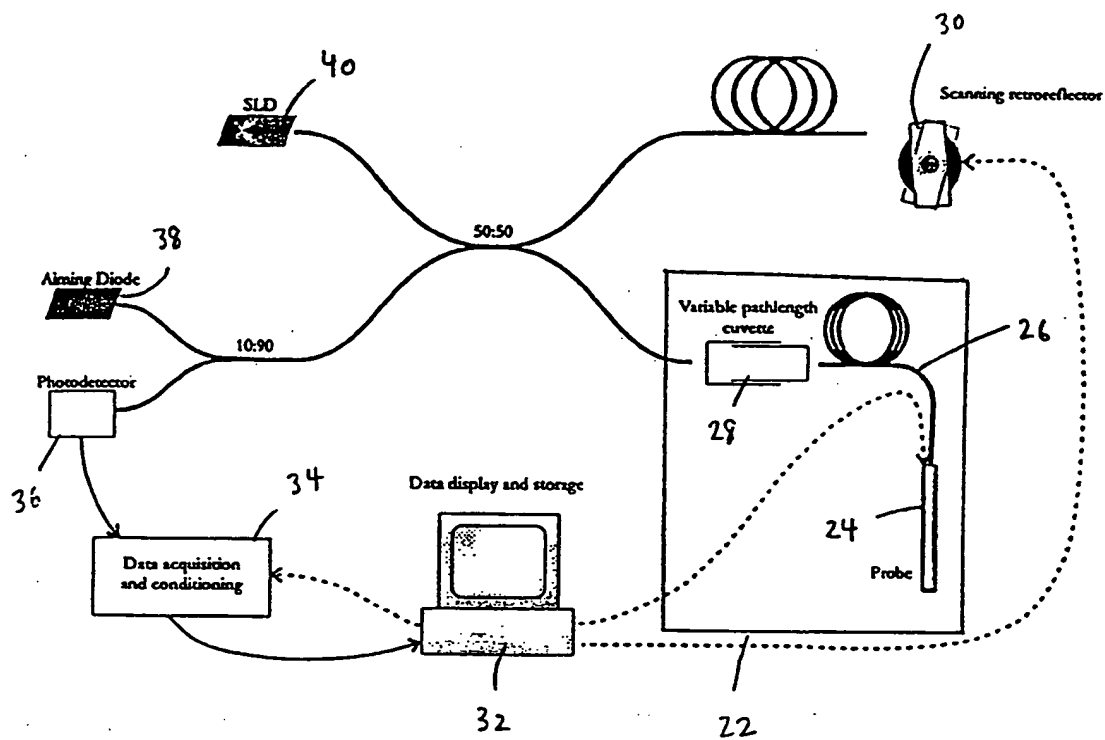


FIG. 3

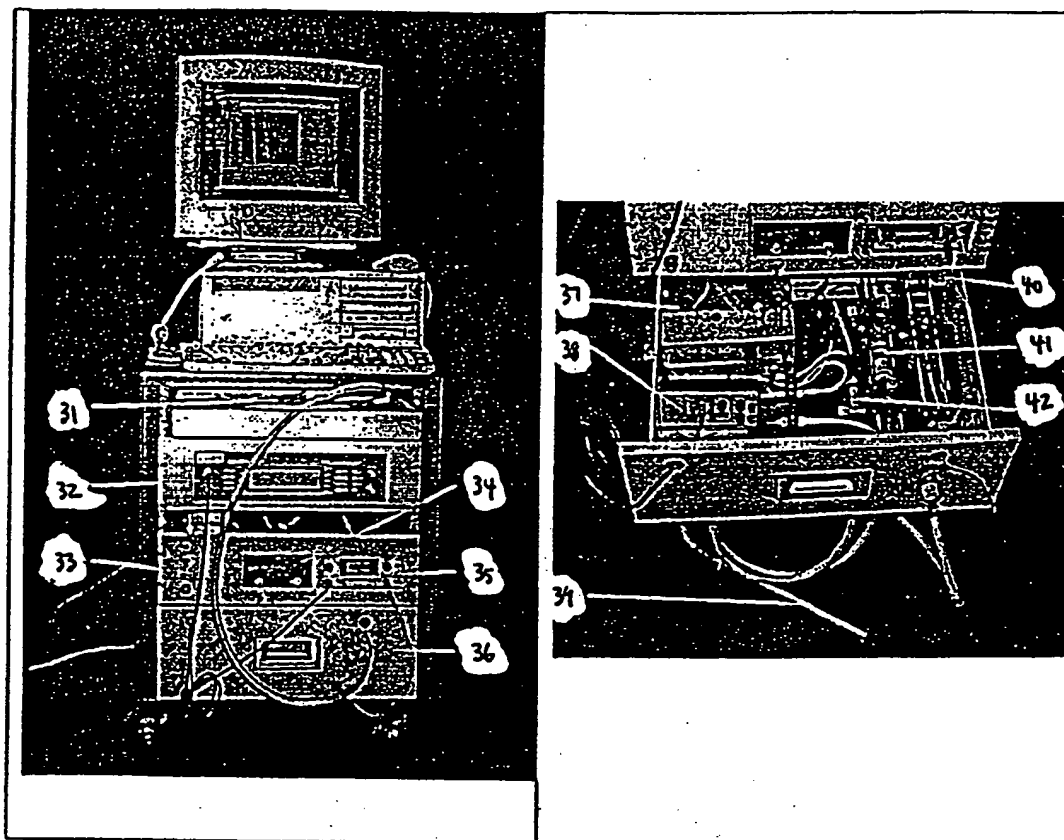


FIG. 4

FIG. 5

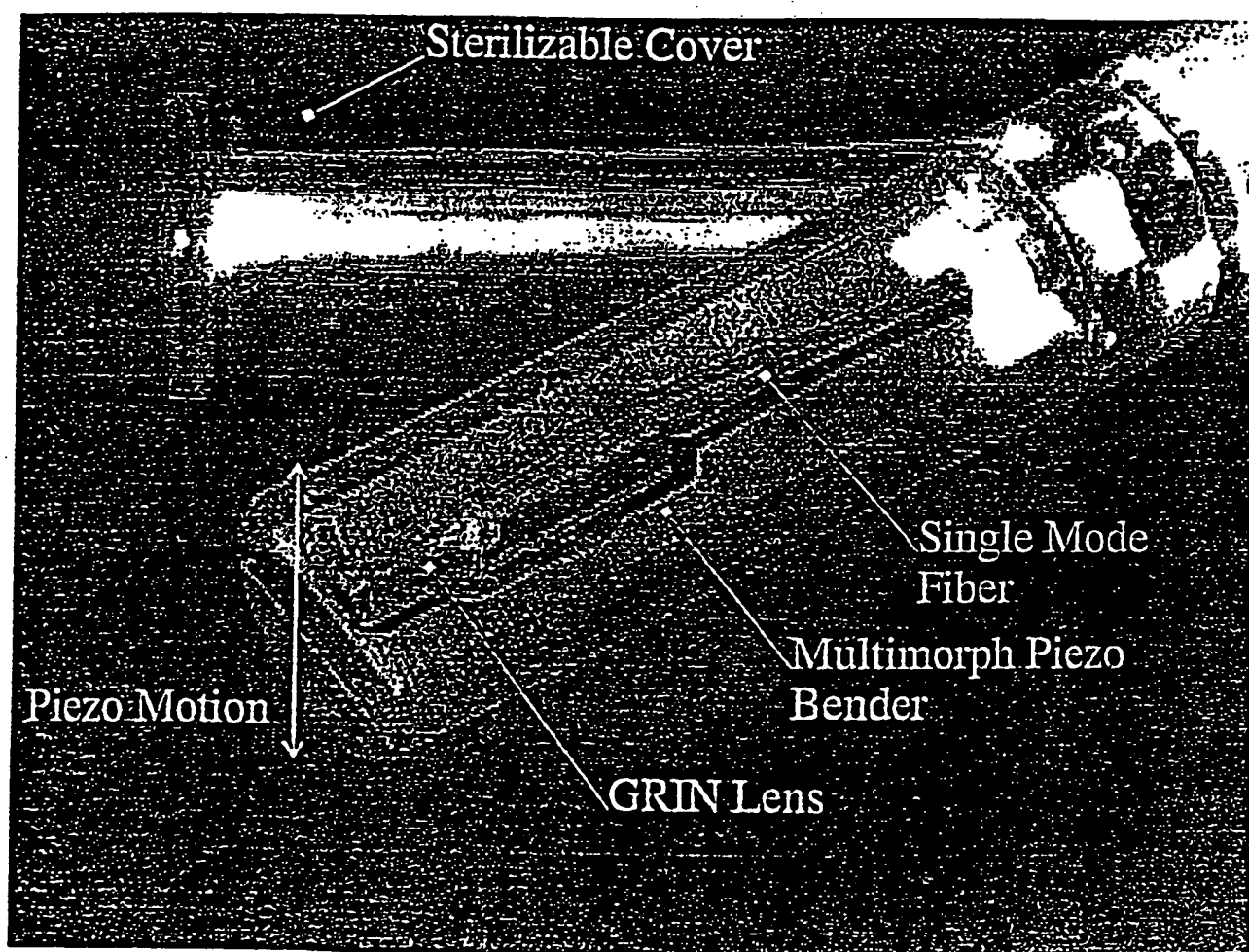
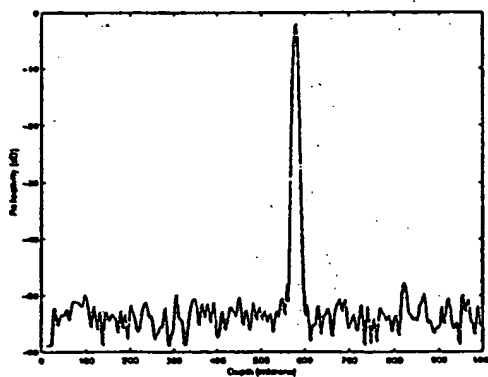


FIG. 6



6/40

**FIG. 7**



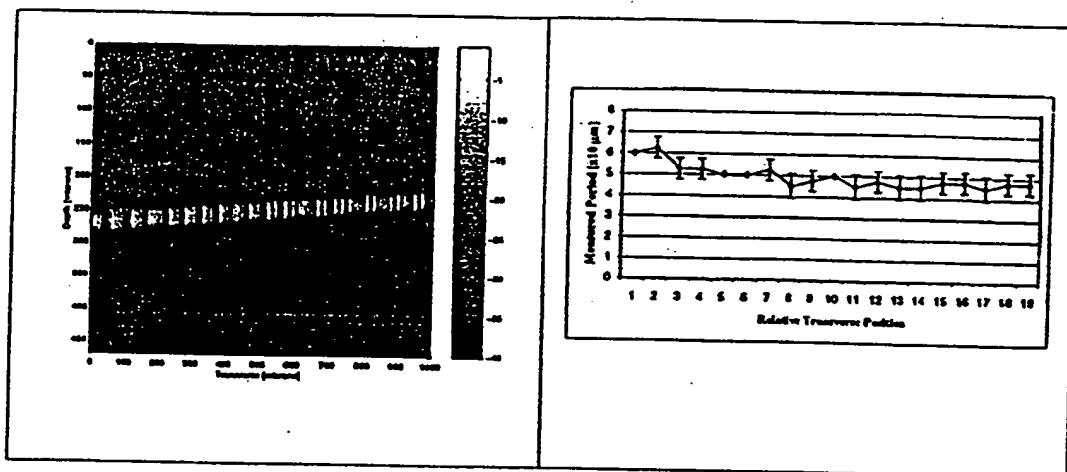


FIG. 8

FIG. 9

8/40

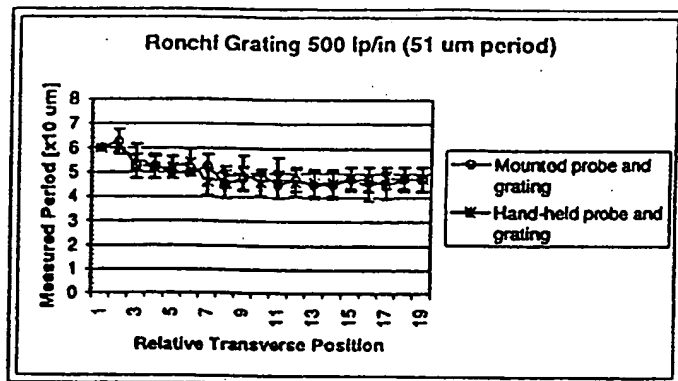


FIG. 10

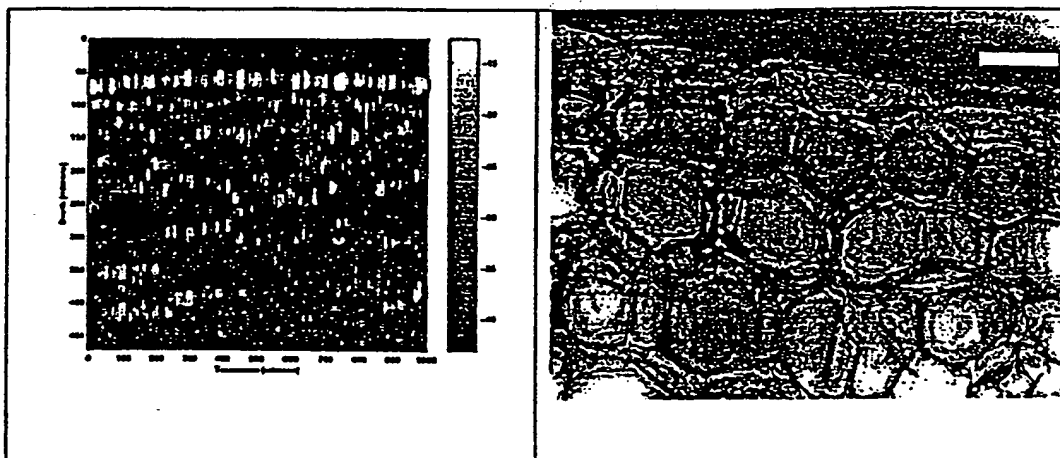


FIG. 11

FIG. 12

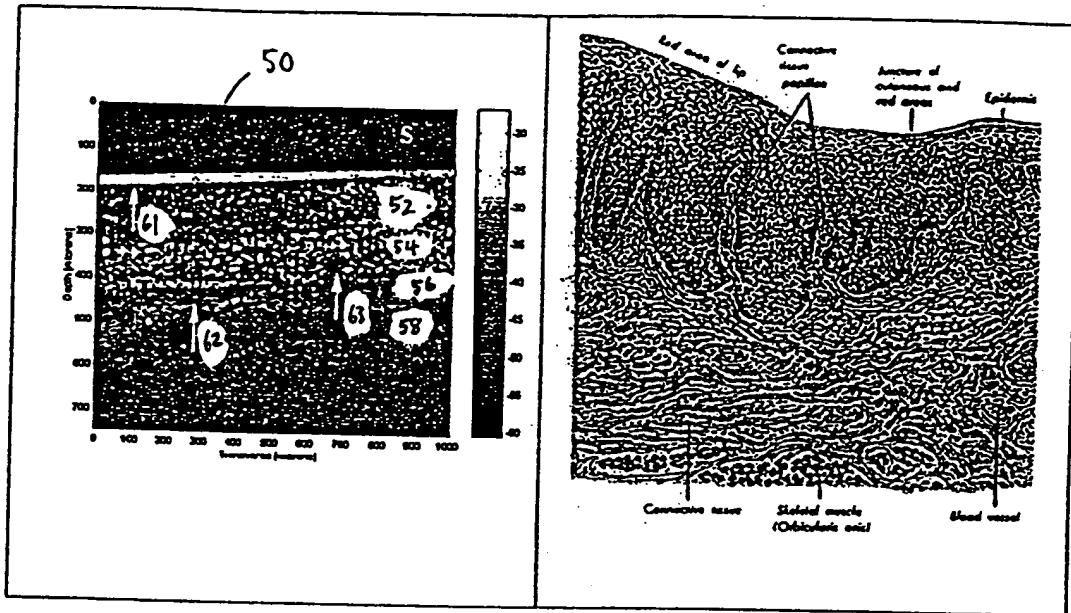


FIG. 13

FIG. 14

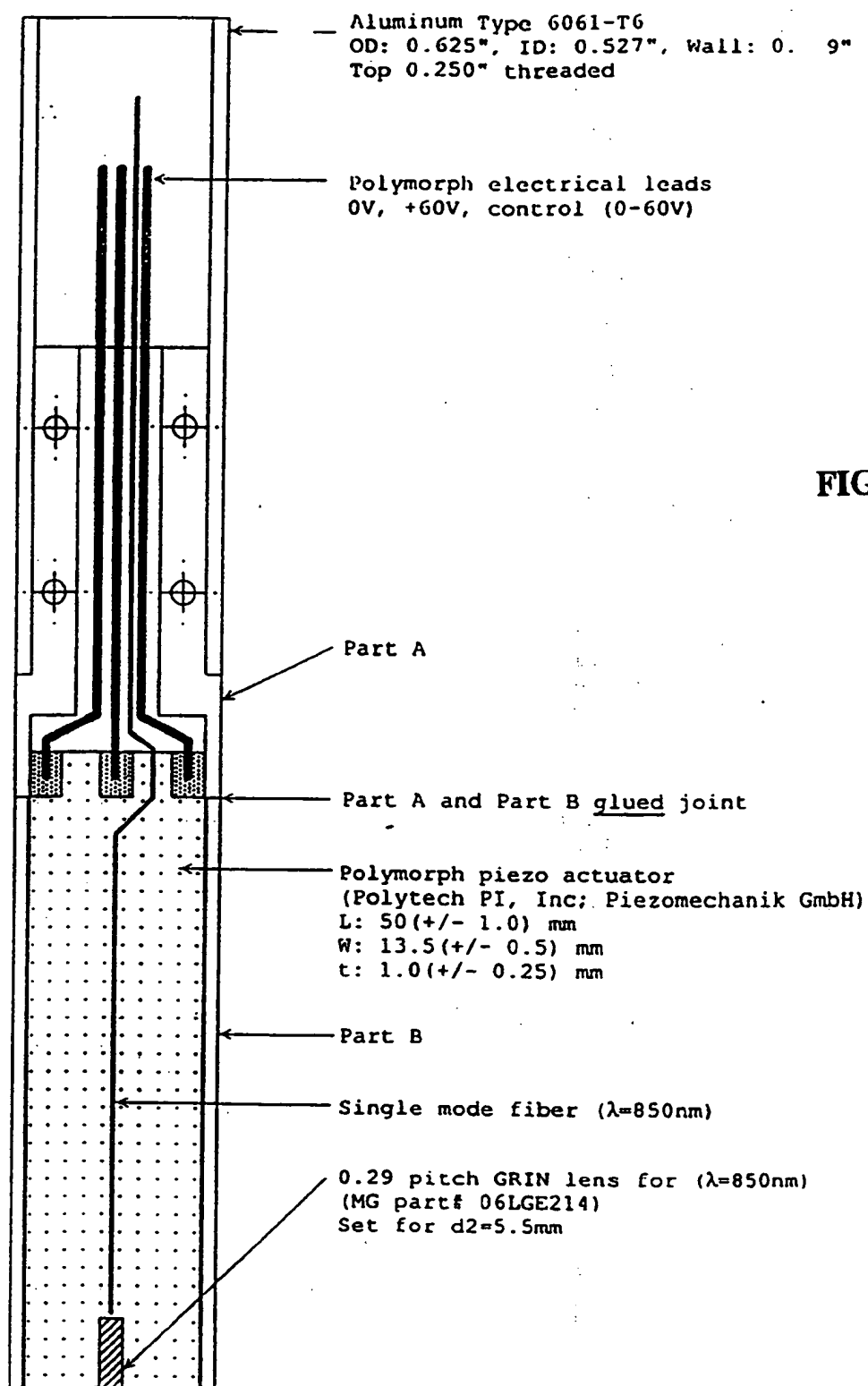


FIG. 15

12/40

FIG. 16

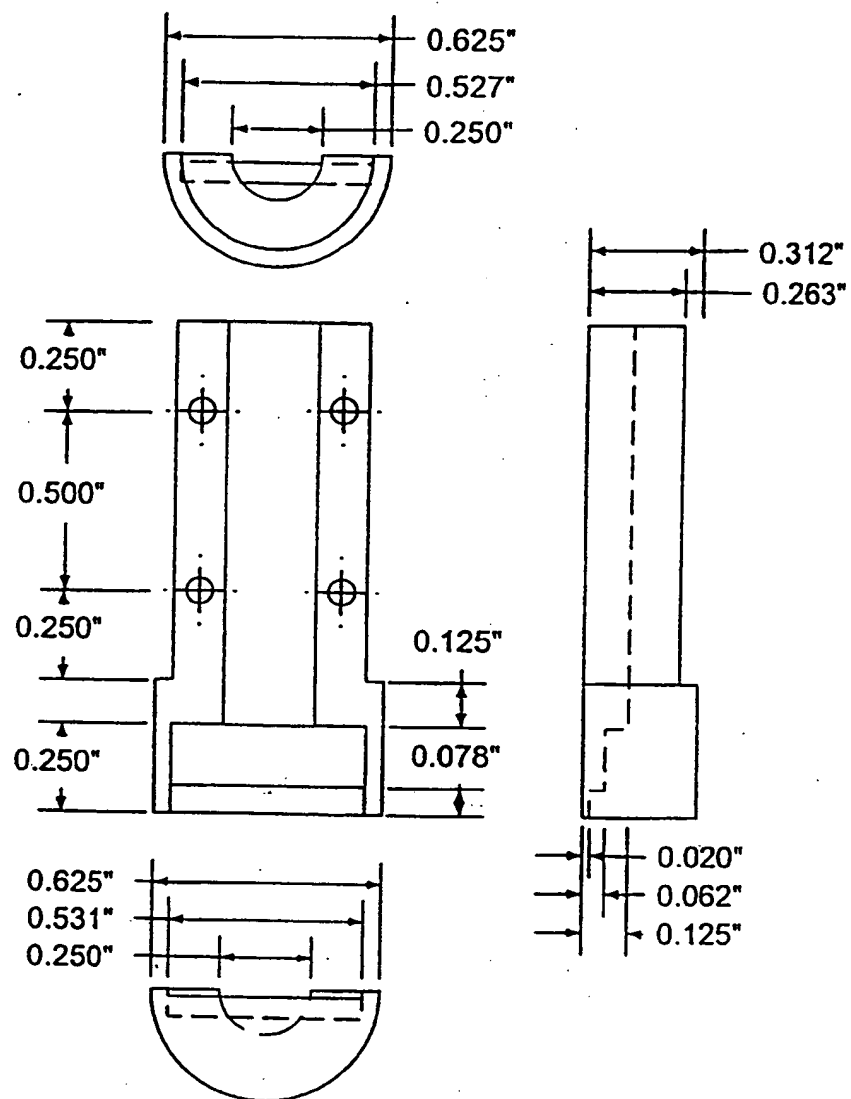


FIG. 17

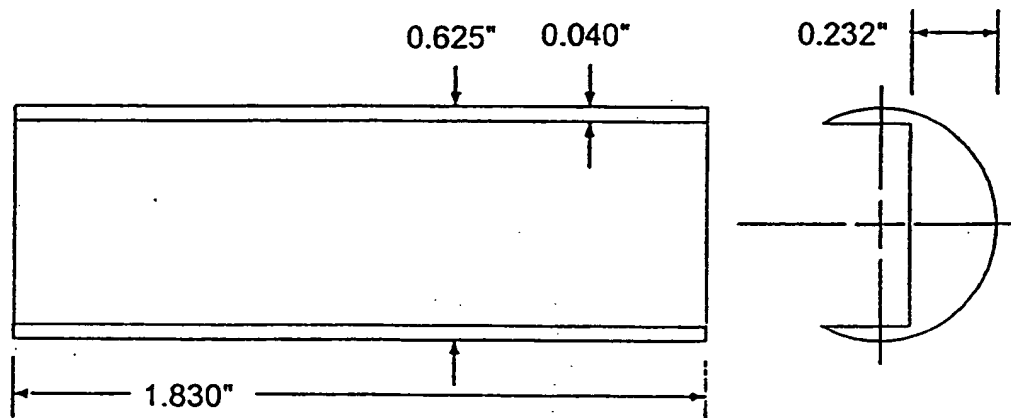




FIG. 18

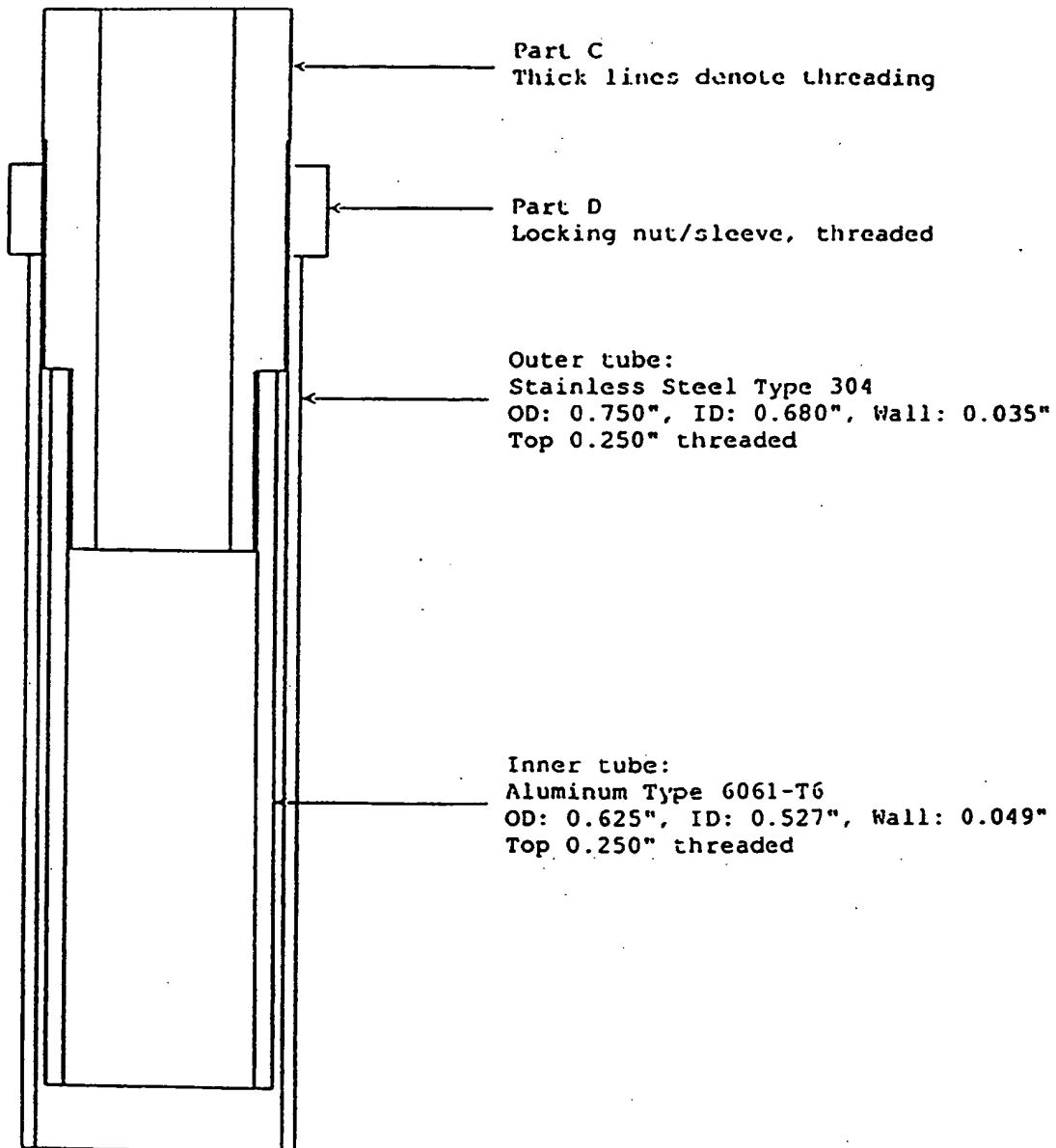


FIG. 19

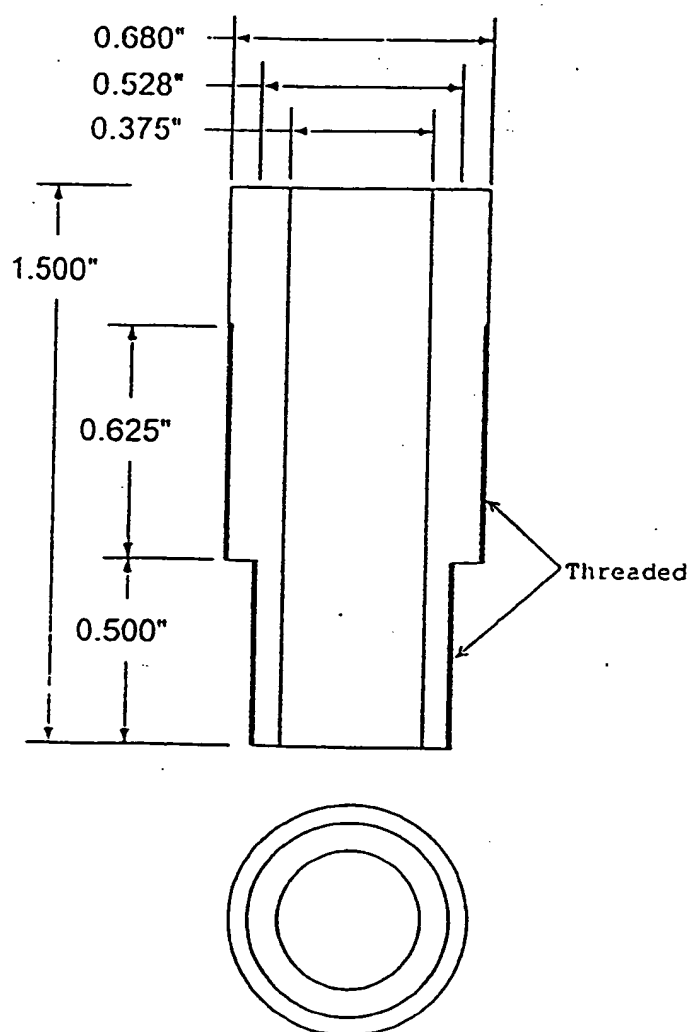
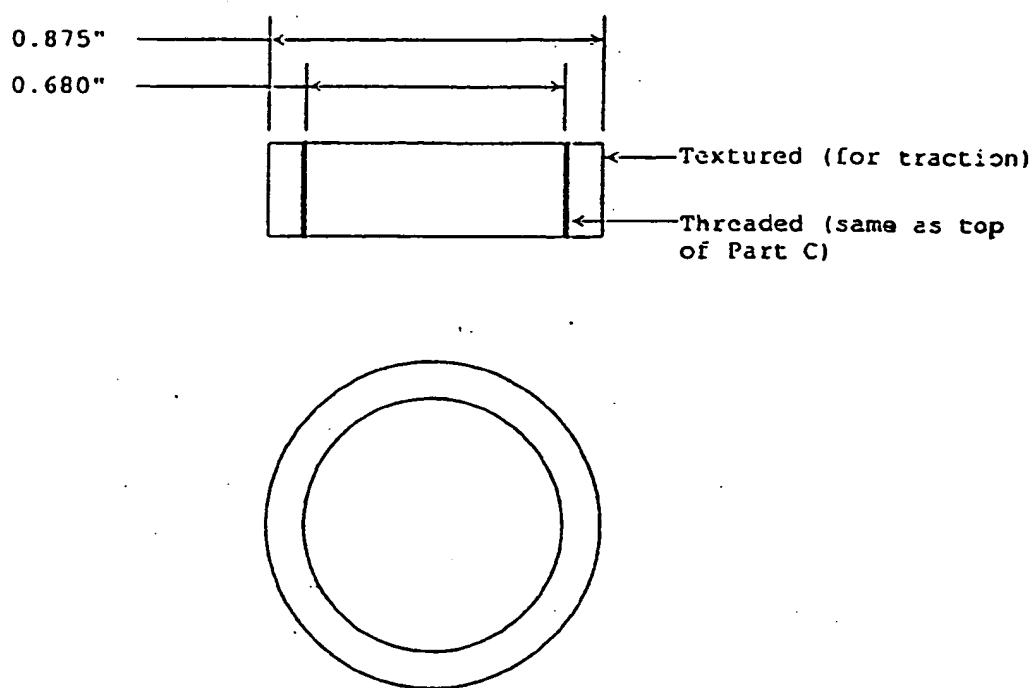
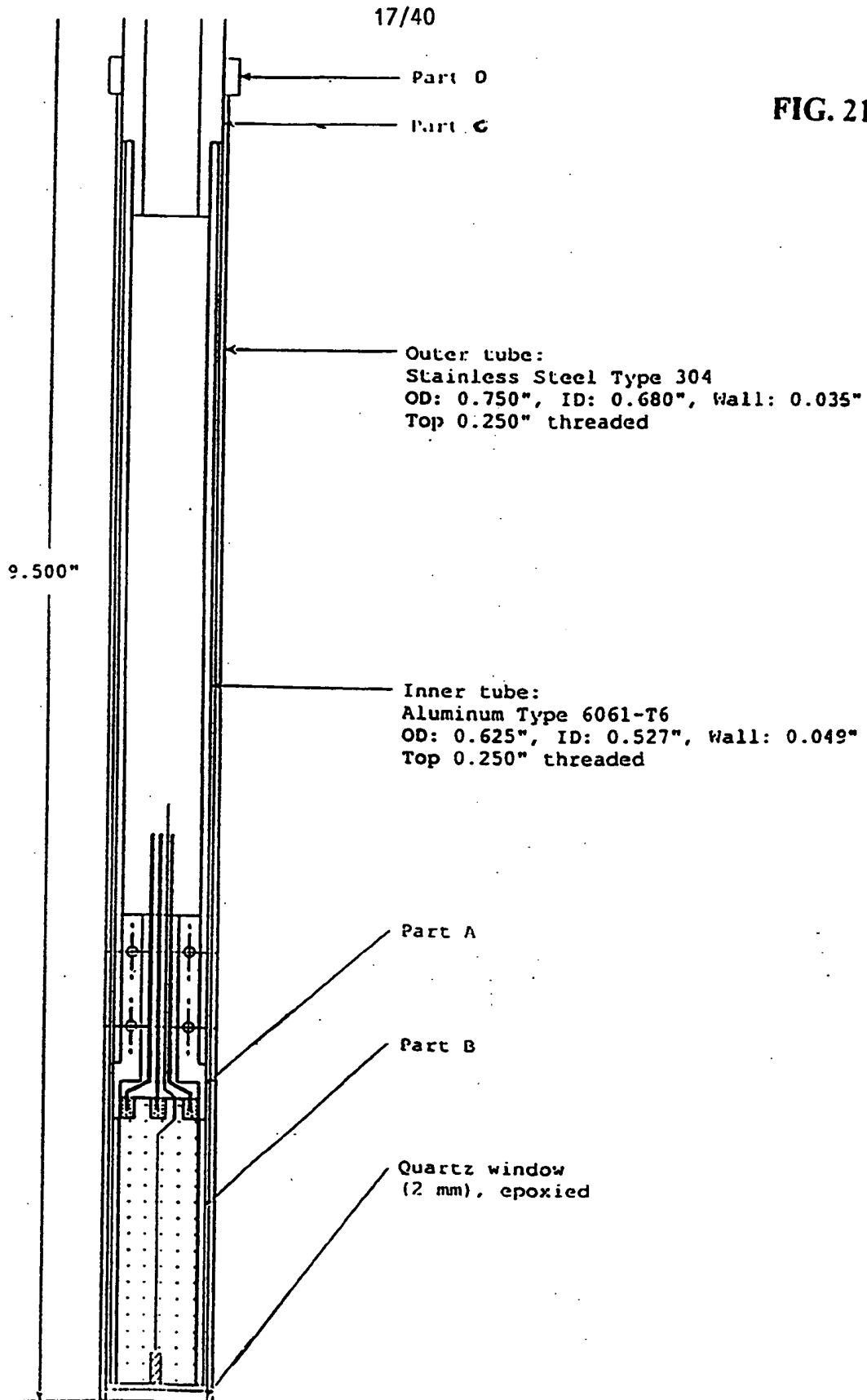


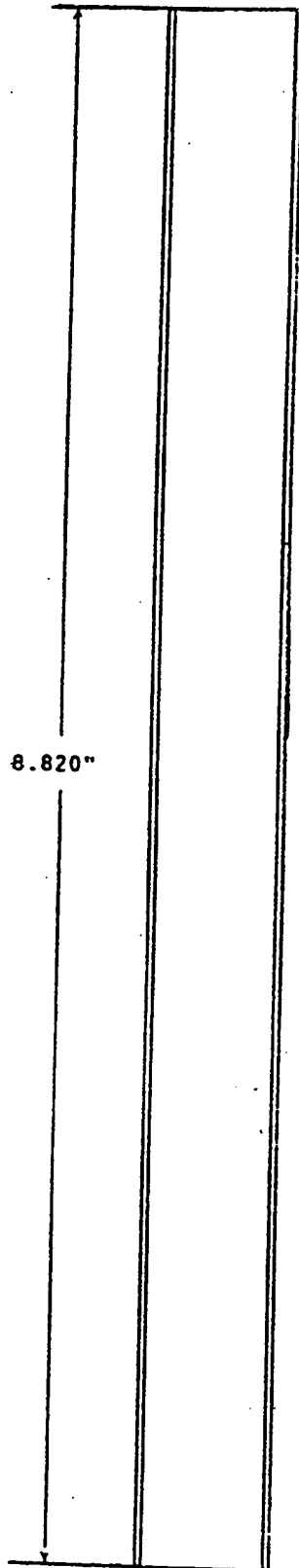
FIG. 20





18/40

**FIG. 22**



Outer tube:  
Stainless Steel Type 304  
OD: 0.750", ID: 0.680", Wall: 0.035"

Top 0.250" (inside) threaded

Small Parts Catalog Part #: A-GPTX-35/12

19/40

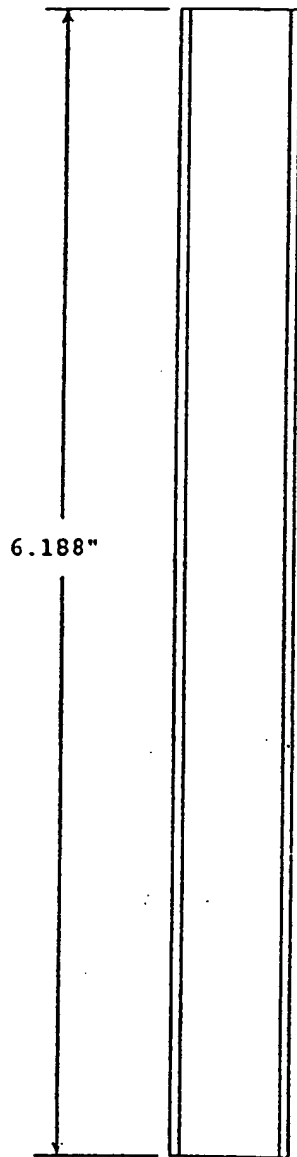


**FIG. 23**

Inner tube:  
Aluminum Type 6061-T6  
OD: 0.625", ID: 0.527", Wall: 0.049"

Top 0.250" (inside) threaded

Small Parts Catalog Part #: A-LAT-49/10

20/40

FIG. 24

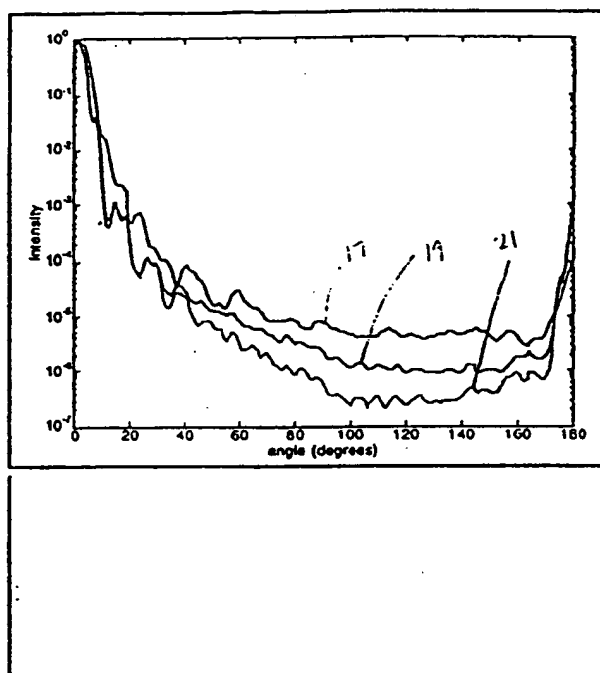
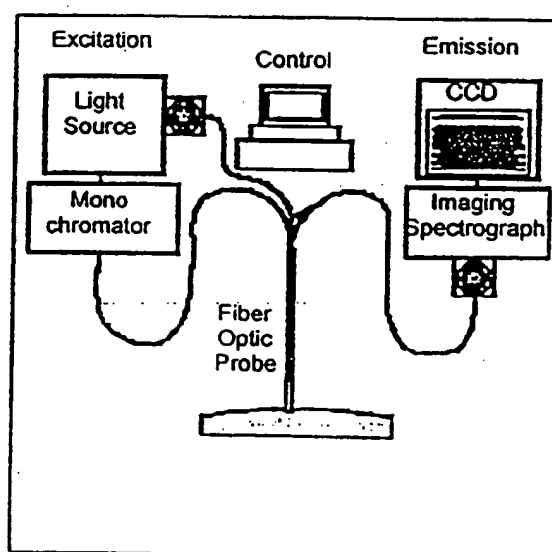


FIG. 25



21/40

FIG. 26

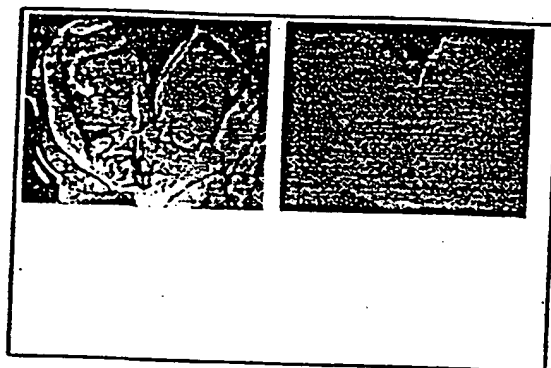


FIG. 27

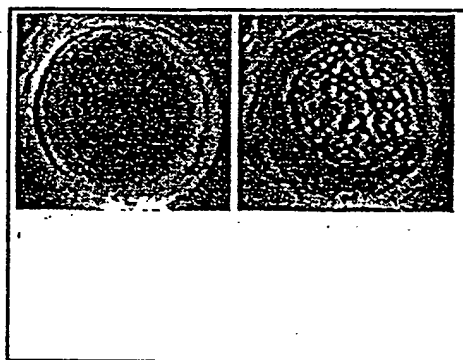
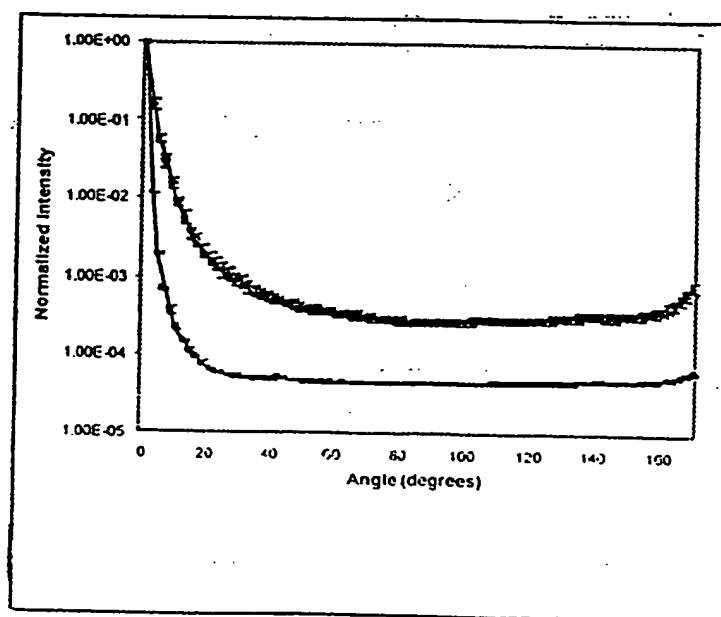


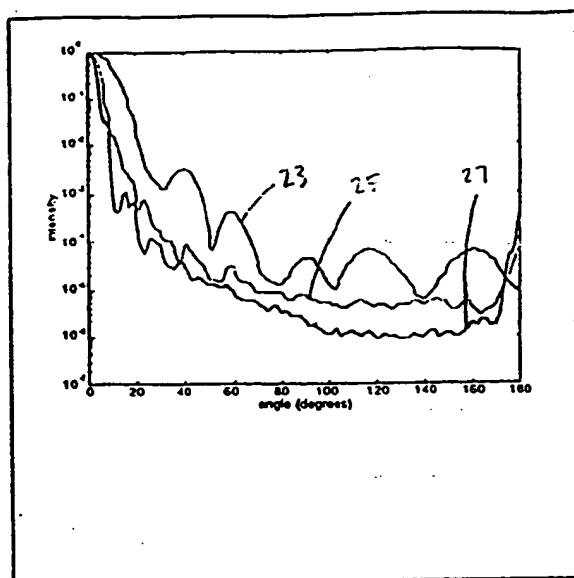
FIG. 28





22/40

FIG. 29



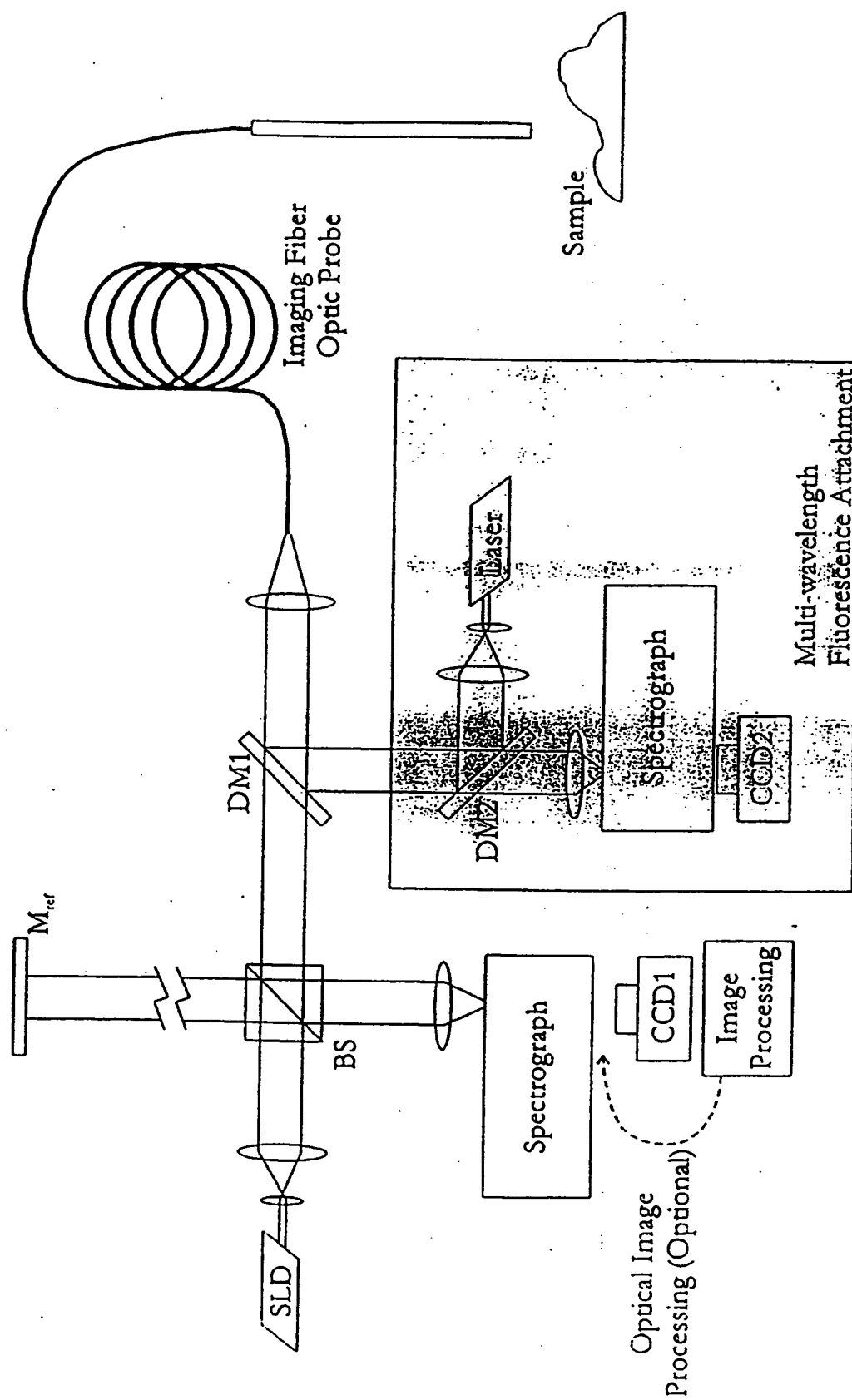


**FIG. 30**

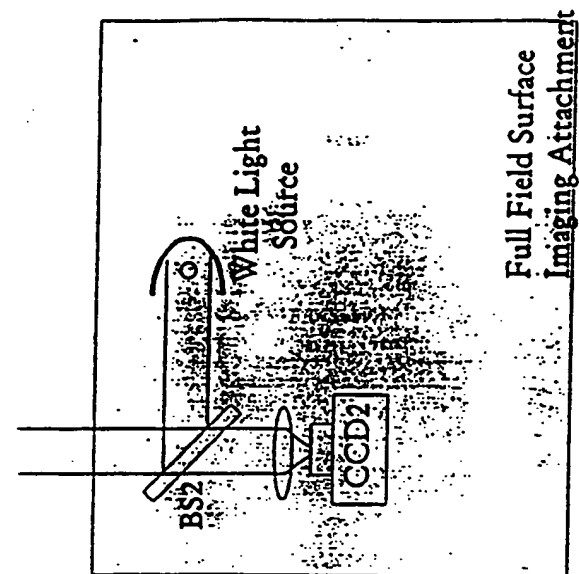


FIG. 32

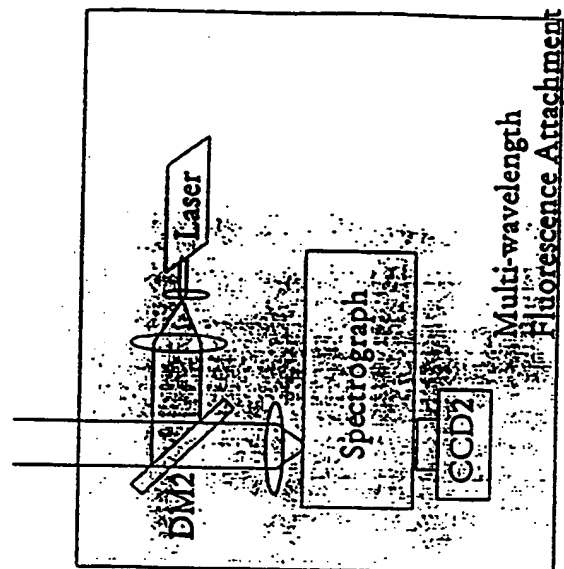


FIG. 34

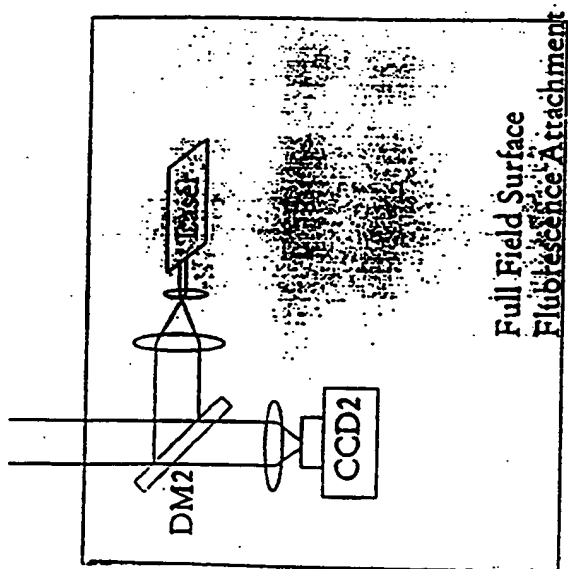


FIG. 31

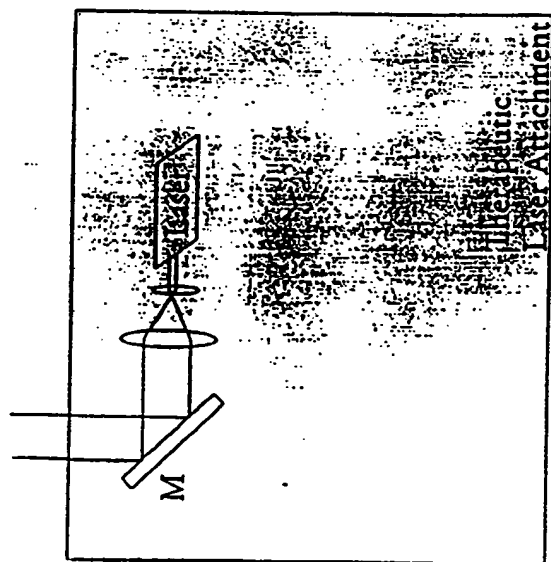


FIG. 33

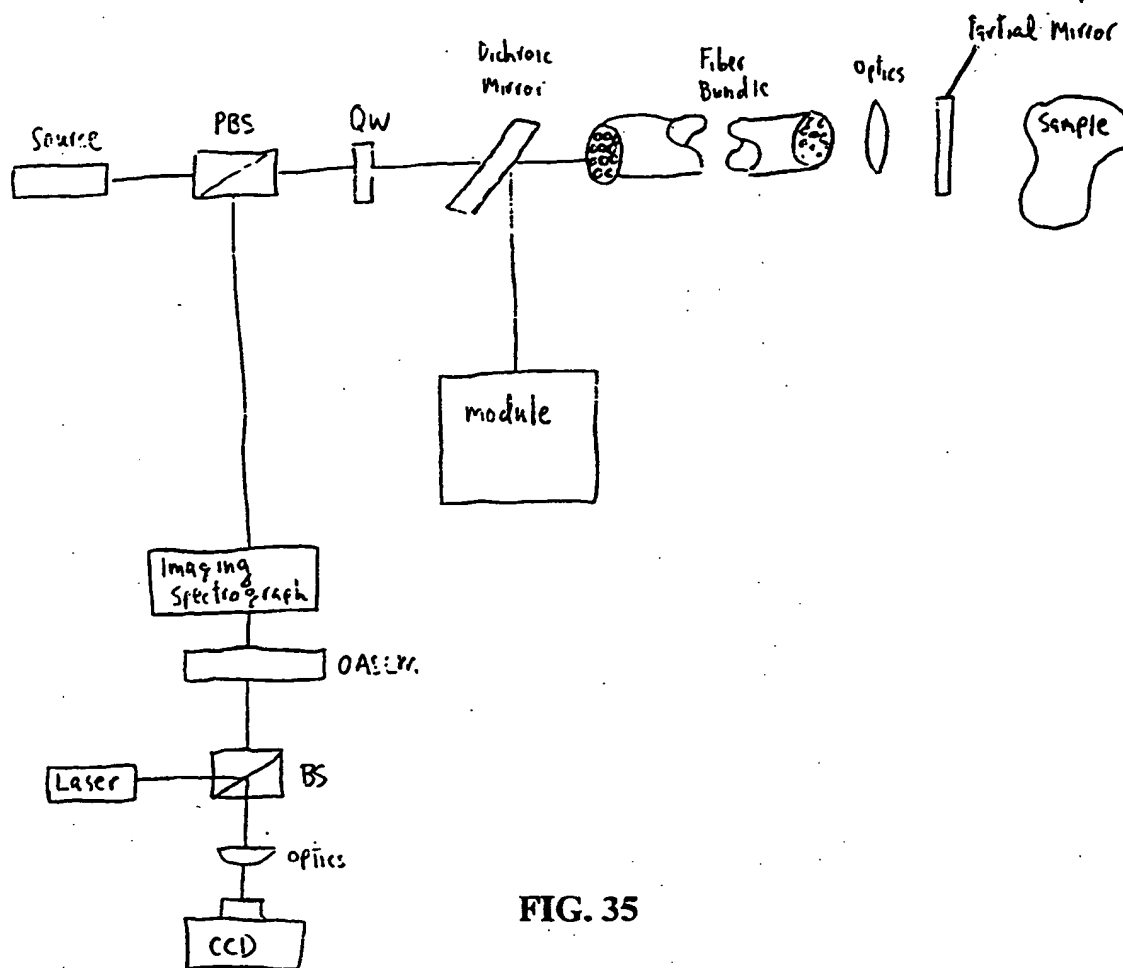


FIG. 35

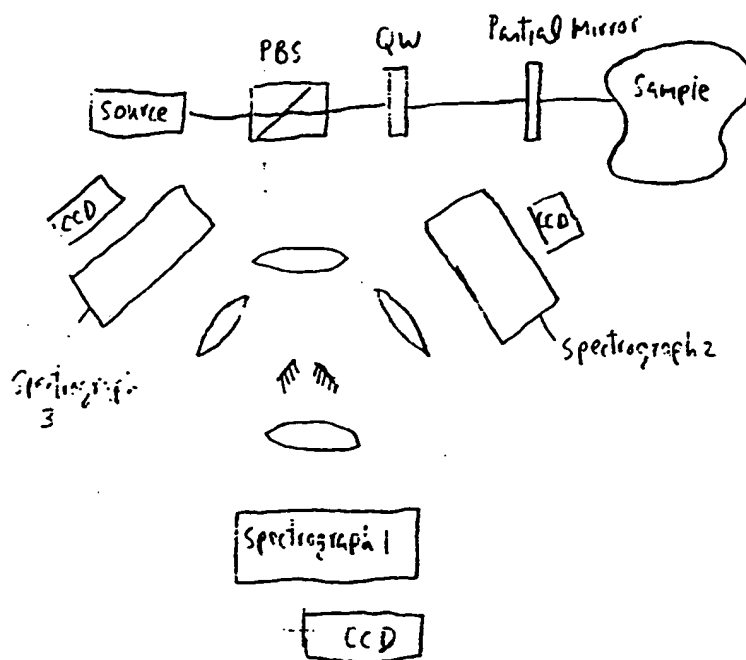


FIG. 36

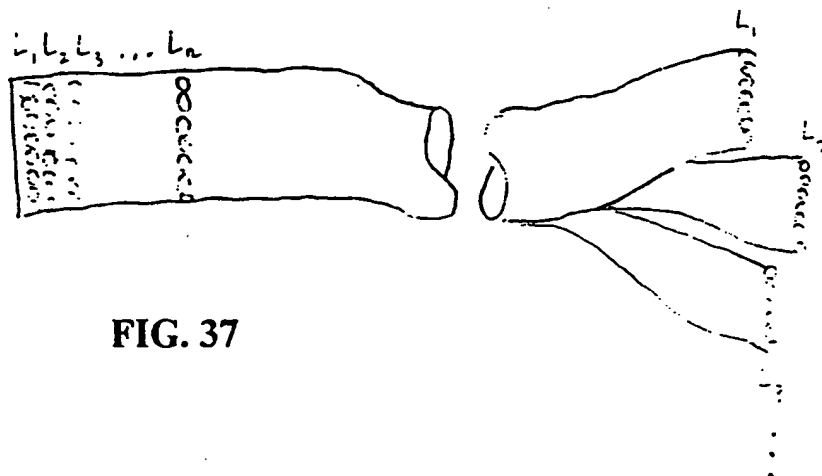


FIG. 37

27/40

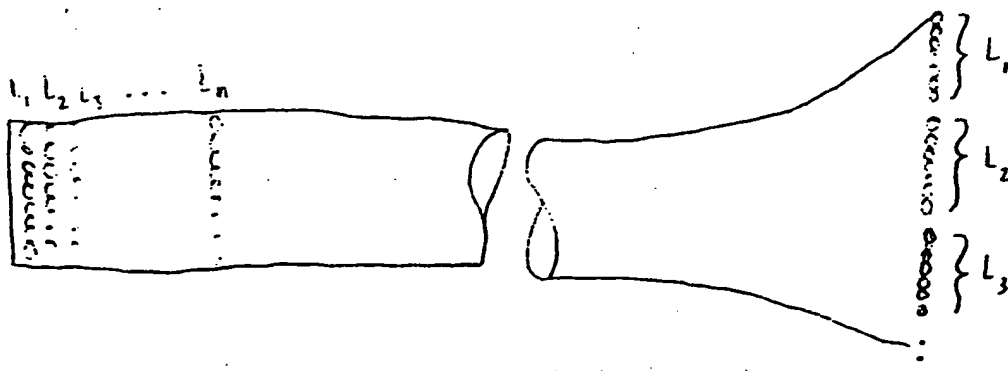


FIG. 38

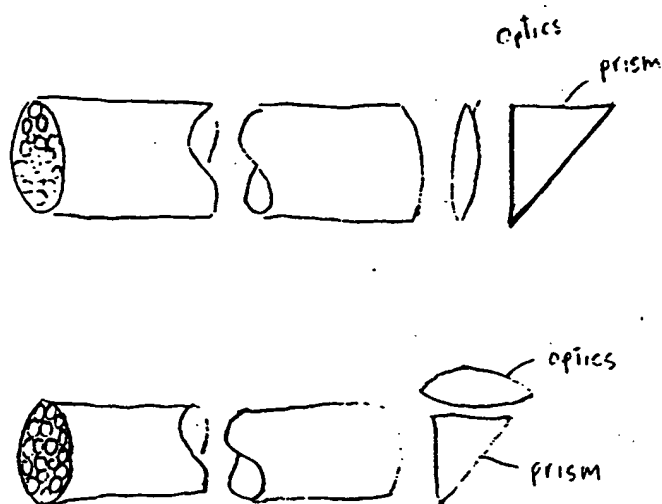


FIG. 39

28/40

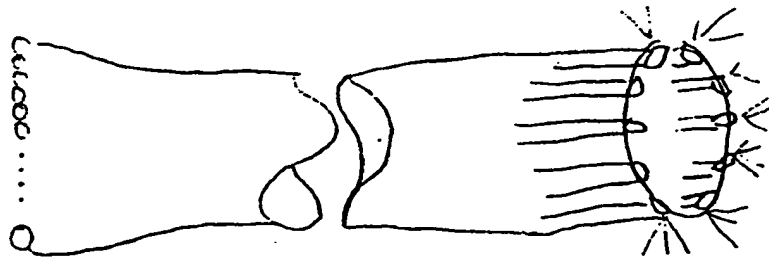


FIG. 40A

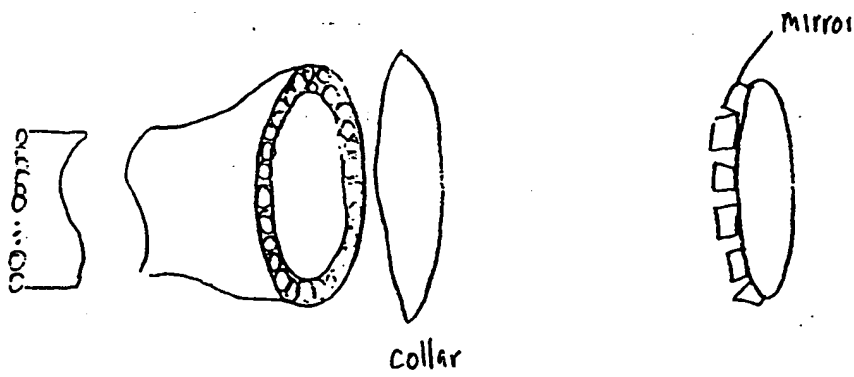


FIG. 40B

29/40

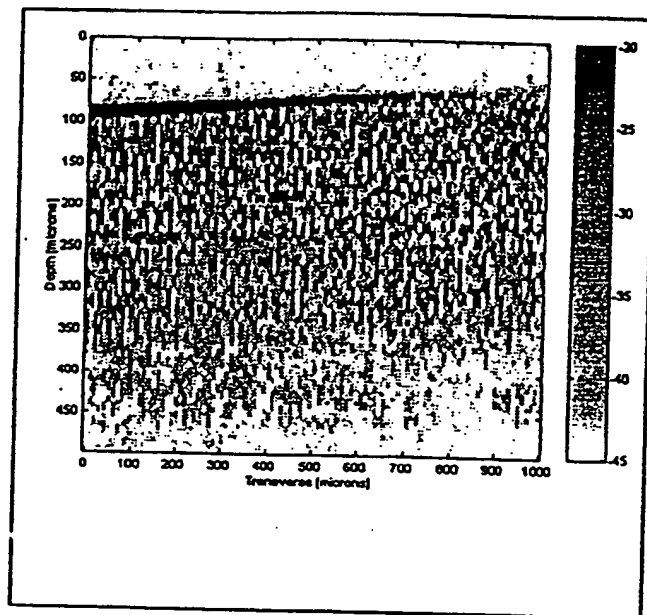


FIG. 41



30/40

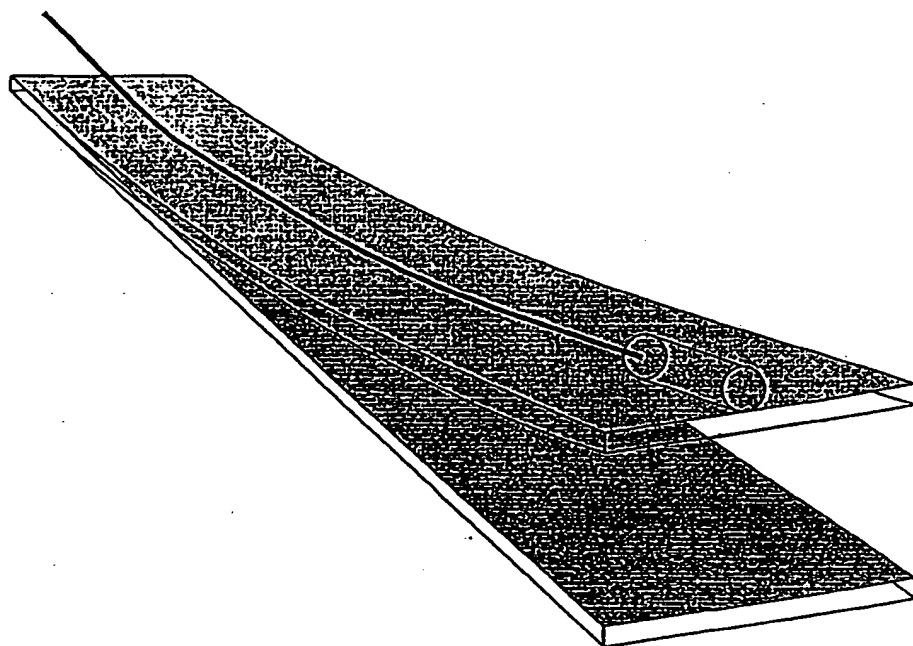
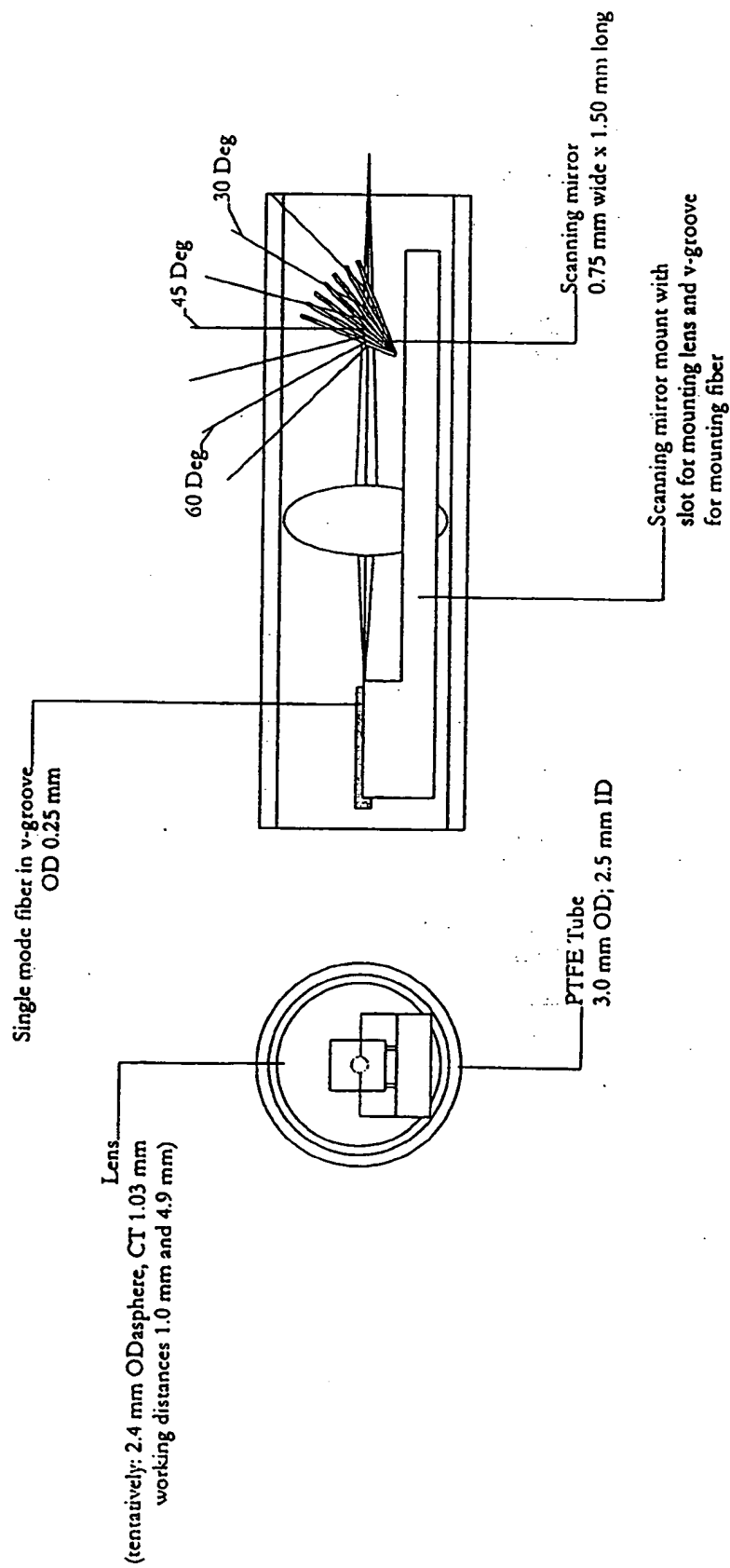


FIG. 42

FIG. 43



32/40

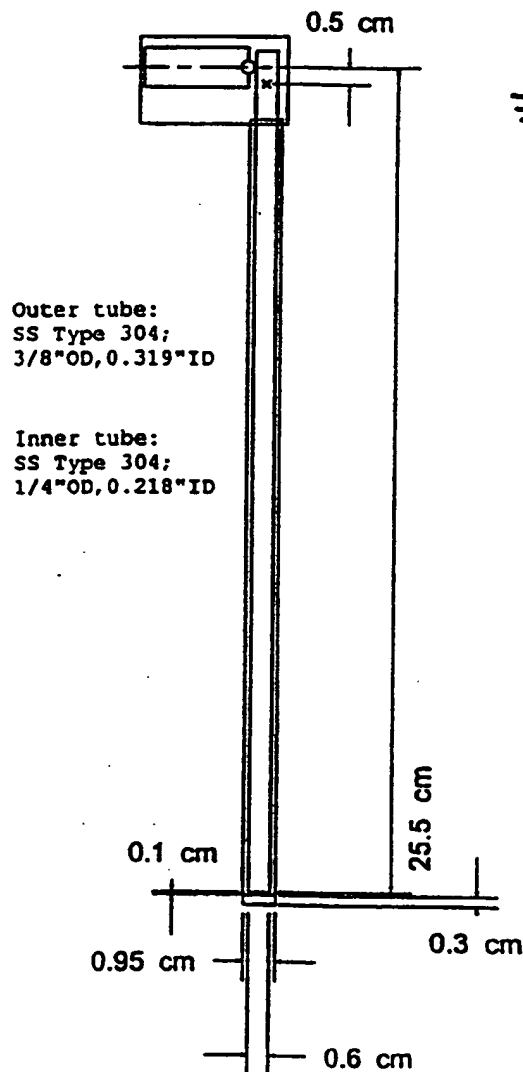


FIG. 44

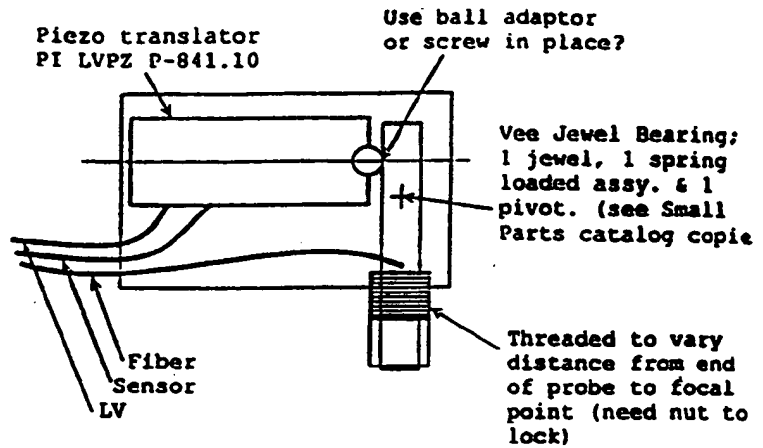


FIG. 45

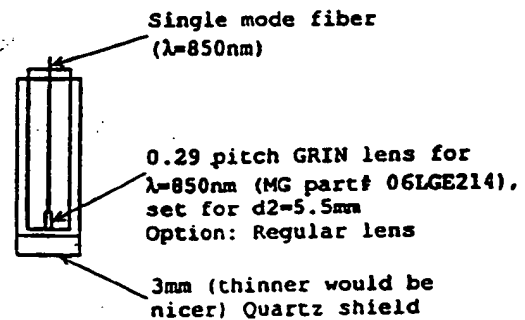


FIG. 46

33/40

FIG. 47

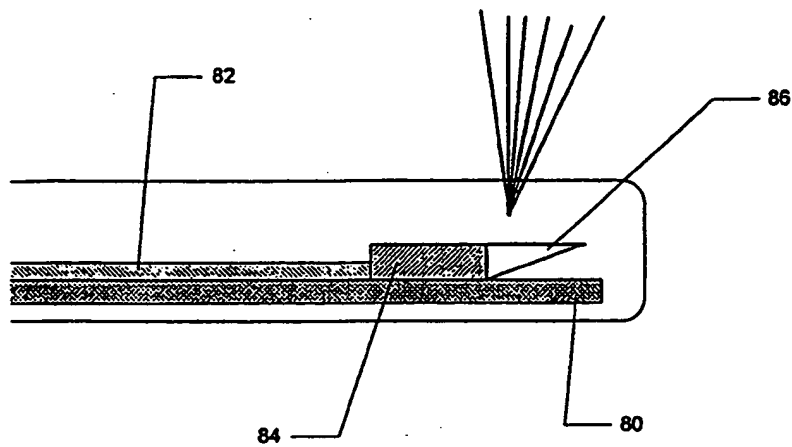
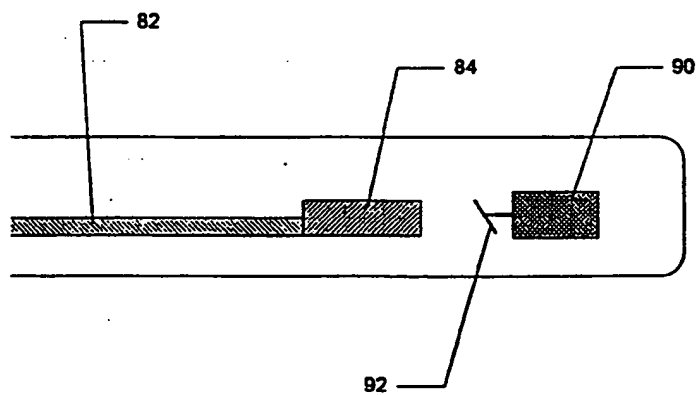


FIG. 48



34/40

FIG. 49

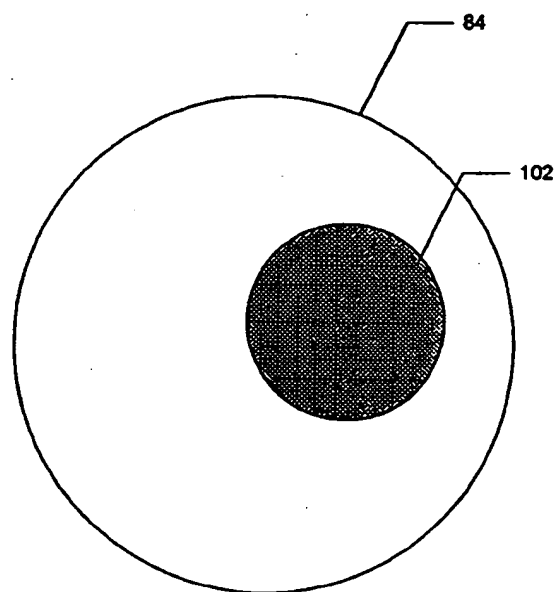
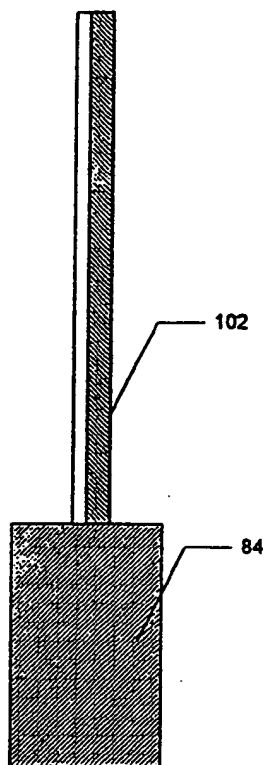


FIG. 50

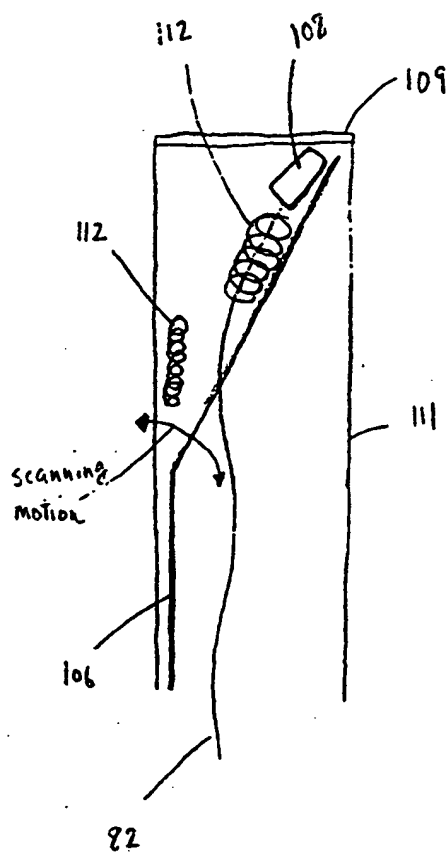


FIG. 51

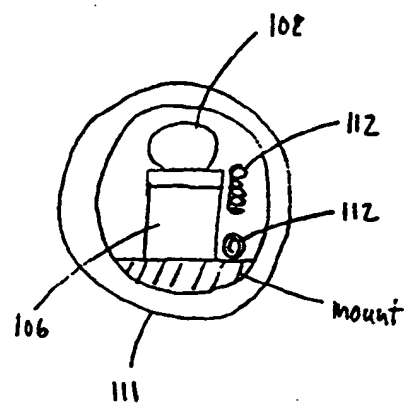


FIG. 52

FIG. 53

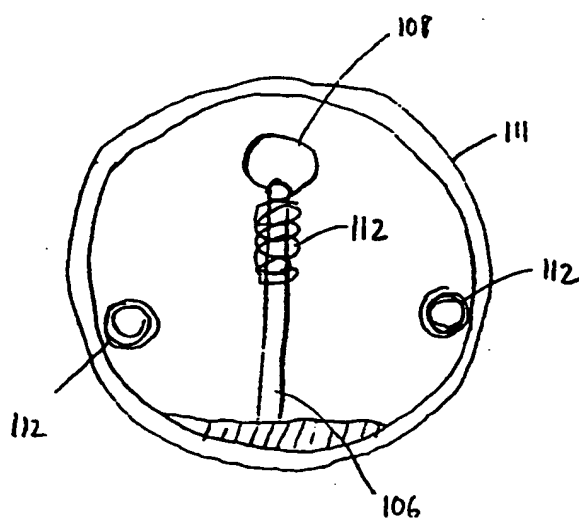
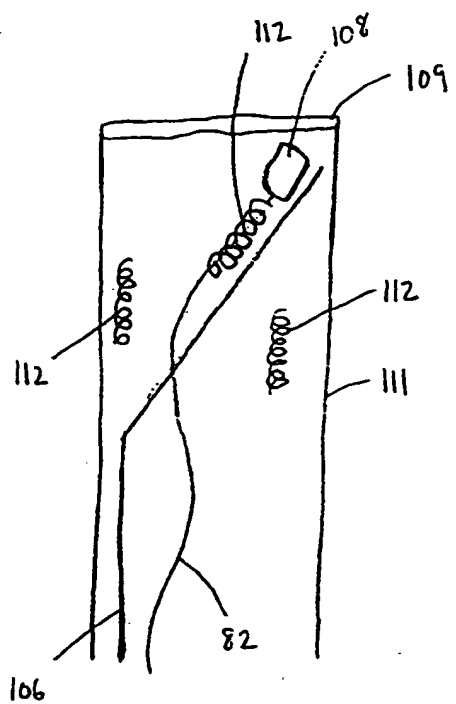


FIG. 54

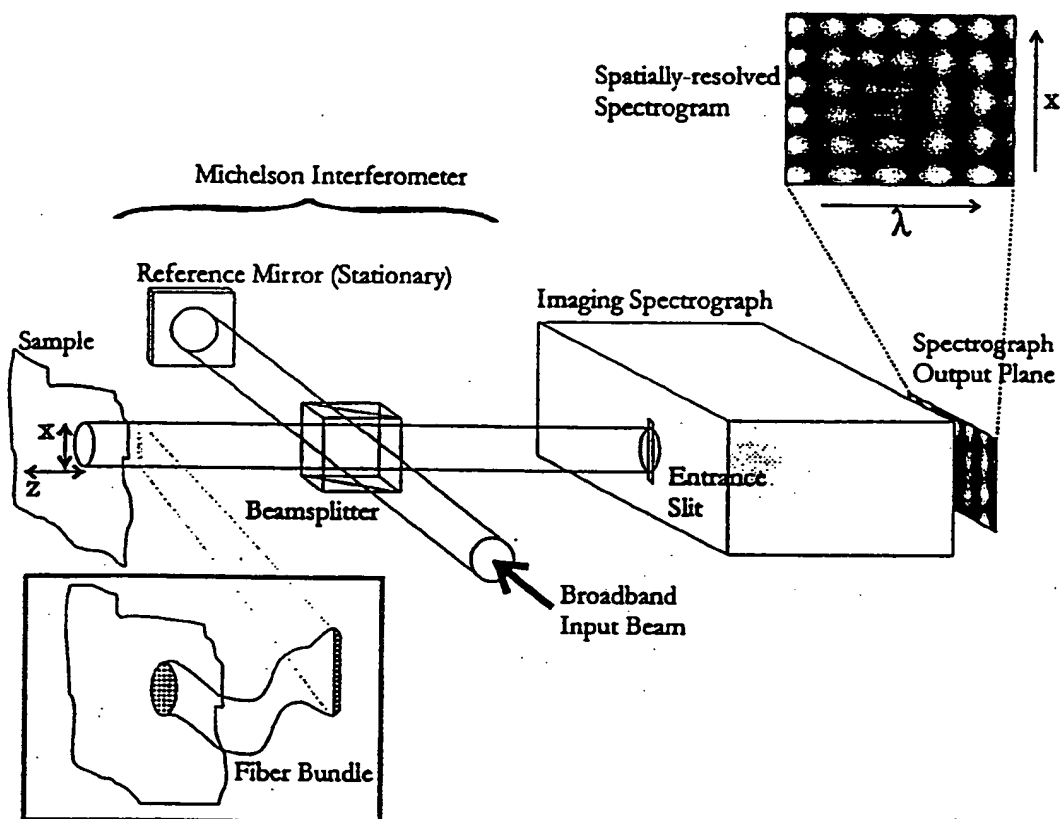


FIG. 55



38/40

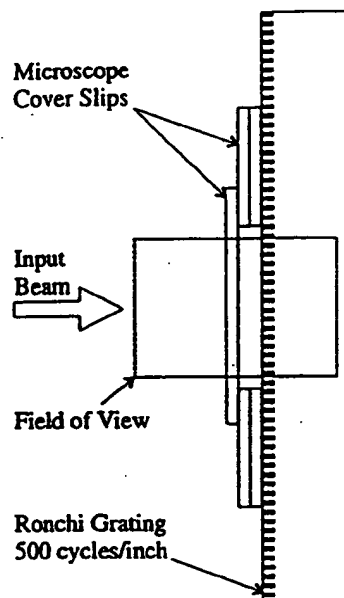


FIG. 56

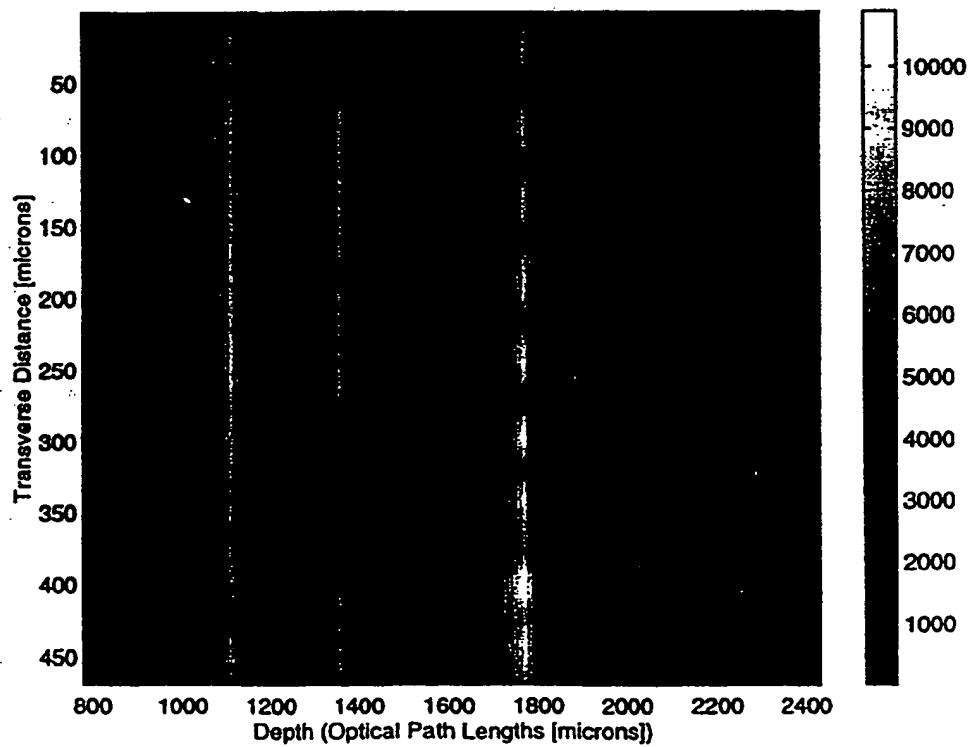


FIG. 57

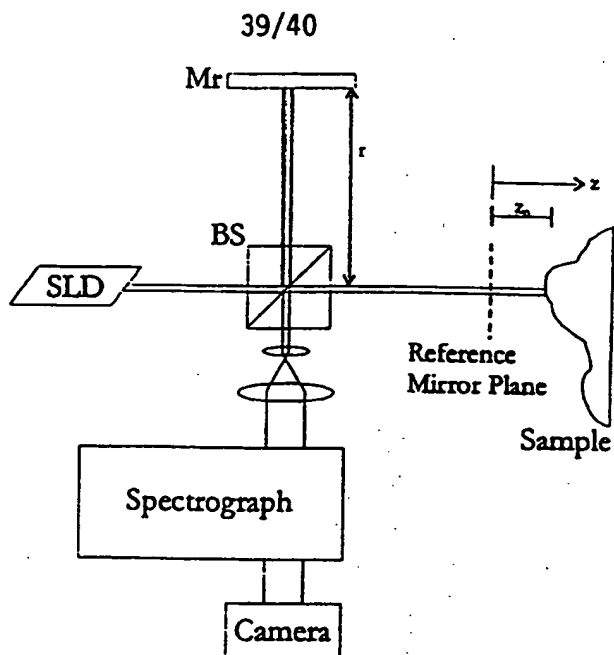
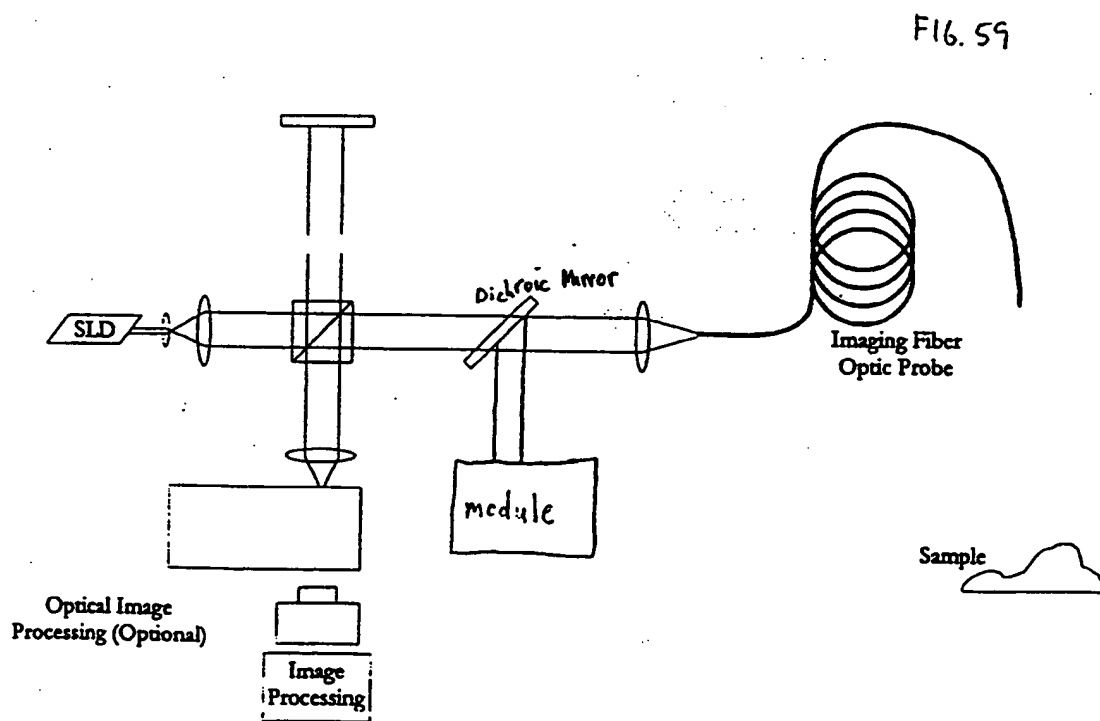


FIG. 58



40/40

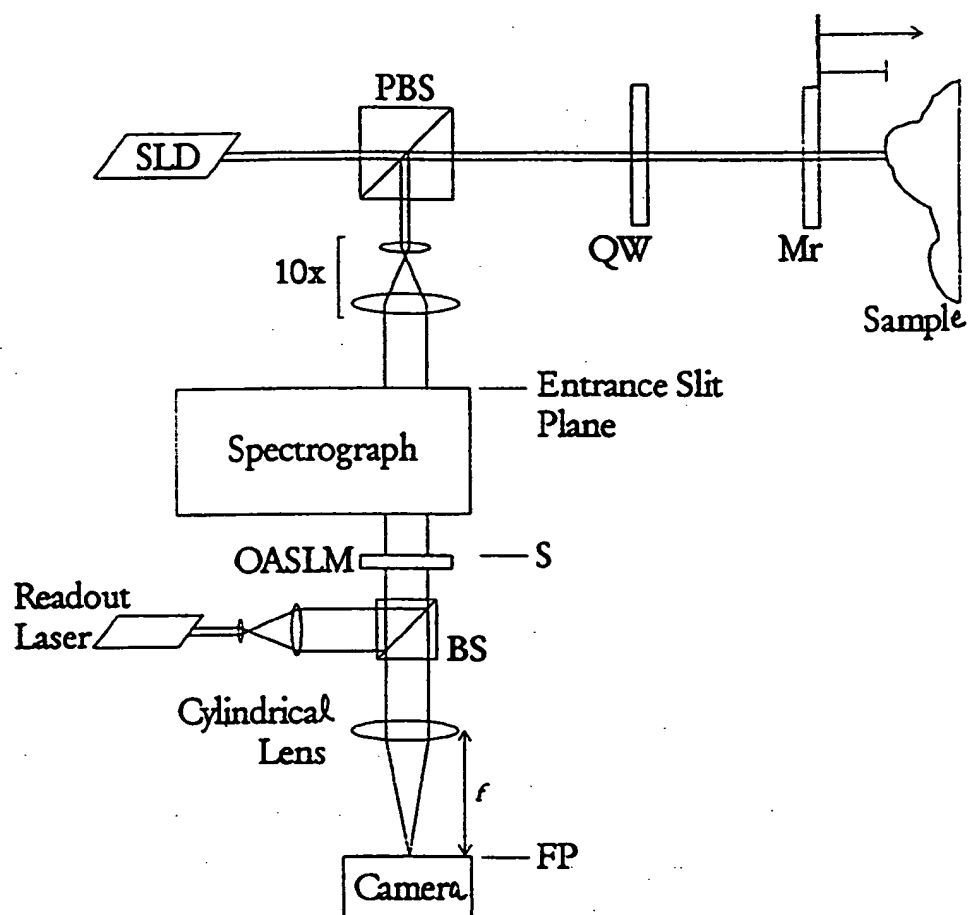


FIG. 60

## INTERNATIONAL SEARCH REPORT

International application No.  
PCT/US99/09626

## A. CLASSIFICATION OF SUBJECT MATTER

IPC(6) :G01B 09/02

US CL :356/345

According to International Patent Classification (IPC) or to both national classification and IPC

## B. FIELDS SEARCHED

Minimum documentation searched (classification system followed by classification symbols)

U.S. : 356/345, 359, 360

Documentation searched other than minimum documentation to the extent that such documents are included in the fields searched  
none

Electronic data base consulted during the international search (name of data base and, where practicable, search terms used)

US PTO APS: endoscope, coherence, in situ, probe

## C. DOCUMENTS CONSIDERED TO BE RELEVANT

Category*	Citation of document, with indication, where appropriate, of the relevant passages	Relevant to claim No.
A	US 5,321,501 A (SWANSON et al) 14 June 1994 (14.06.1994), see entire document	1-60

☐ Further documents are listed in the continuation of Box C. ☐ See patent family annex.

* Special categories of cited documents:	
*A* document defining the general state of the art which is not considered to be of particular relevance	*T* later document published after the international filing date or priority date and not in conflict with the application but cited to understand the principle or theory underlying the invention
*B* earlier document published on or after the international filing date	*X* document of particular relevance; the claimed invention cannot be considered novel or cannot be considered to involve an inventive step when the document is taken alone
*L* document which may throw doubts on priority claim(s) or which is cited to establish the publication date of another citation or other special reason (as specified)	*Y* document of particular relevance; the claimed invention cannot be considered to involve an inventive step when the document is combined with one or more other such documents, such combination being obvious to a person skilled in the art
*O* document referring to an oral disclosure, use, exhibition or other means	*A* document member of the same patent family
*P* document published prior to the international filing date but later than the priority date claimed	

Date of the actual completion of the international search  
17 JUNE 1999Date of mailing of the international search report  
28 JUN 1999Name and mailing address of the ISA/US  
Commissioner of Patents and Trademarks  
Box PCT  
Washington, D.C. 20231

Authorized officer

ROBERT KIM *[Signature]*

**This Page is Inserted by IFW Indexing and Scanning  
Operations and is not part of the Official Record**

**BEST AVAILABLE IMAGES**

Defective images within this document are accurate representations of the original documents submitted by the applicant.

Defects in the images include but are not limited to the items checked:

- ☐ BLACK BORDERS
- ☐ IMAGE CUT OFF AT TOP, BOTTOM OR SIDES
- ☒ FADED TEXT OR DRAWING
- ☒ BLURRED OR ILLEGIBLE TEXT OR DRAWING
- ☐ SKEWED/SLANTED IMAGES
- ☐ COLOR OR BLACK AND WHITE PHOTOGRAPHS
- ☐ GRAY SCALE DOCUMENTS
- ☒ LINES OR MARKS ON ORIGINAL DOCUMENT
- ☒ REFERENCE(S) OR EXHIBIT(S) SUBMITTED ARE POOR QUALITY
- ☐ OTHER: \_\_\_\_\_

**IMAGES ARE BEST AVAILABLE COPY.**

**As rescanning these documents will not correct the image problems checked, please do not report these problems to the IFW Image Problem Mailbox.**